Durham E-Theses

Numerical studies of superfluids and superconductors

Winiecki, Thomas

How to cite:

Winiecki, Thomas (2001) *Numerical studies of superfluids and superconductors*, Durham theses, Durham University. Available at Durham E-Theses Online: http://etheses.dur.ac.uk/3876/

Use policy

The full-text may be used and/or reproduced, and given to third parties in any format or medium, without prior permission or charge, for personal research or study, educational, or not-for-profit purposes provided that:

- a full bibliographic reference is made to the original source
- a link is made to the metadata record in Durham E-Theses
- the full-text is not changed in any way

The full-text must not be sold in any format or medium without the formal permission of the copyright holders.

Please consult the full Durham E-Theses policy for further details.

Academic Support Office, Durham University, University Office, Old Elvet, Durham DH1 3HP
e-mail: e-theses.admin@dur.ac.uk Tel: +44 0191 334 6107
http://etheses.dur.ac.uk

Numerical Studies of Superfluids and Superconductors

Thomas Winiecki

A thesis submitted in partial fulfilment
of the requirements for the degree of
Doctor of Philosophy

The copyright of this thesis rests with the author. No quotation from it should be published in any form, including Electronic and the Internet, without the author's prior written consent. All information derived from this thesis must be acknowledged appropriately.

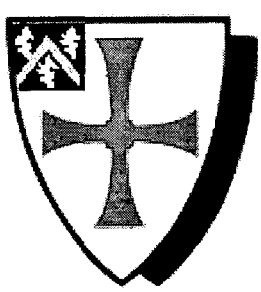

The University of Durham
Department of Physics
2001

- 8 MAR 2002

Numerical Studies of Superfluids and Superconductors

Thomas Winiecki

Abstract

In this thesis we demonstrate the power of the Gross-Pitaevskii and the time-dependent Ginzburg-Landau equations by numerically solving them for various fundamental problems related to superfluidity and superconductivity. We start by studying the motion of a massive object through a quantum fluid modelled by the Gross-Pitaevskii equation. Below a critical velocity, the object does not exchange momentum or energy with the fluid. This is a manifestation of its superfluid nature. We discuss the effect of applying a constant force to the object and show that for small forces a vortex ring is created to which the object becomes attached. For a larger force the object detaches from the vortex ring and we observe periodic shedding of rings. All energy transfered to the system is contained within the vortex rings and the drag force on the object is due to the recoil of the vortex emission. If we exceed the speed of sound, there is an additional contribution to the drag from sound emission. To make a link to superconductivity, we then discuss vortex states in a rotating system. In the ground state, regular arrays of vortices are observed which, for systems containing many vortices, mimic solid-body rotation. In the second part of the thesis, we initially review solutions to the Ginzburg-Landau equations in an applied magnetic field. For superconducting disks we observe vortex arrays similar to those in rotating superfluids. Finally, we study an electrical current flow along a superconducting wire subject to an external magnetic field. We observe the motion of flux lines, and hence dissipation, due to the Lorentz force. We measure the $V - I$ curve which is analogous to the drag force in a superfluid. With the introduction of impurities, flux lines become pinned which gives rise to an increased critical current.

Declaration

I confirm that no part of the material offered has previously been submitted by me for a degree in this or in any other University. If material has been generated through joint work, my independent contribution has been clearly indicated. In all other cases material from the work of others has been acknowledged and quotations and paraphrases suitability indicated.

Thomas Winiecki
Durham, 29th August 2001

The copyright of this thesis rests with the author. No quotation from it should be published without their written consent and information derived from it should be acknowledged.

Acknowledgements

I have greatly enjoyed the past three years here at Durham and I would like to express thanks to all the people who have contributed in some way to this thesis.

I am particularly indebted to Charles, my supervisor, for his support, enthusiasm and inspiration which was always there when I needed it and to Jim who helped me during my first year. Further, many thanks to Ifan and Mark for countless enlightening discussions (and chats) and for proof-reading. Cheers to Brian, Carolyn, Eleni, Hilary and Richard for the about 1500 coffee breaks we must have had, to Michael and Vicky for their most excellent skill in making award-winning posters, and of course to Lydia for regularly putting patches on all computers and keeping the whole system running happily.

Outside work, I have been extremely lucky to have met so many very special people who have made Durham a very special place. I wish to thank all my friends of the 'E-team': Ali (simply the king), Amir, Angel (world-class cook and world-class friend), Claudia, Jane, Jonas, Maria A, Rafael, Rainer (Halt die Ohren steif!), Richard, Susana and Thomas F for all the great times we have had, for the trips to Scotland, Spain, France, London, Belgium, Mexico, Germany, ..., for all the dinners, for playing 'H' or just for being so incredibly 'E'. Many thanks to Hugo, Nic, Philipp and Shogo for being the craziest but 'luveliest' house mates I have ever had and to Alain, Alex M and Hannah for trying to teach me English (or English to me?) and for regularly appointing me as a burger-turner. I also owe thanks to all the people of my final year who all understand how to feed me very well: Doug, Fernando, Gerado, Jun (tasteful jokes), Kha-Young, Marco, Maria-Angelica (my Spanish teacher), Maria S, Masa, Olga (second best nurse on this planet), Pet (more beer, mate!), Veronique (amazing cakes) and Yanmei (sorry about the alphabetical order).

A special thank you to my friends at home, Conny, Frank, Mathias, Sebastian, Tobias and Thomas A, who have always given me a warm welcome.

On the financial side, I have appreciated the substantial aid from the Studienstiftung des deutschen Volkes (German National Merit Foundation) and the EPSRC.

Finally, and far from least, I would like to show gratitude to my parents and to Maria-Jose for their never-ending love and support.

Contents

List of Figures

Chapter 1

Introduction

For many years superfluid ^{4}He was considered to be the only experimental example of the occurrence of Bose-Einstein condensation (BEC). In recent years, however, the phenomenon of BEC has been identified in various systems [1], for instance amongst excitations in semiconductors; as a pairing of quarks and anti-quarks in elementary particles; in neutron stars and; most recently, in dilute alkali gases. BEC is also related to the BCS transition in ^{3}He and superconductors. Another compelling example concerns the cascade of phase transitions in the early universe. According to the Kibble mechanism [2, 3], defects such as domain walls, cosmic strings and monopoles may have been formed spontaneously during the rapid cooling through the condensation point. The following table, taken from [1], gives an idea of the diversity of systems in which Bose-Einstein condensation takes place and shows the large temperature range at which the transition occurs.

Particle	System	T_c(K)
^{1}H, ^{7}Li, ^{23}Na, ^{87}Rb	atomic vapours	10^{-6}
^{3}He pair	superfluid	10^{-3}
exciton (e^-, h^+)	semiconductor	10^{-2}
^{4}He atom	superfluid	2.17
Cooper pair	superconductor	10
neutron pair	neutron stars	10^8
$q\bar{q}$	vacuum	10^{34}

A common theme for these systems is the occurence of a long-range quantum phase coherence. In 1924 Satyendra Nath Bose [4] and Albert Einstein [5] studied a uni-

form non-interacting gas of bosons at low temperatures and found a phase transition at a characteristic temperature below which a macroscopic number of particles occupy the same quantum state. In contrast to fermions (which obey Pauli's exclusion principle) bosons tend to cluster in the lowest energy state and form a coherent macroscopic wavefunction, or order parameter, which is accompanied with the observed long-range correlations. Far below the transition temperature, the fraction of non-condensate particles is often small and the system can be described solely by this order parameter.

The aim of this thesis is to study two quite distinct systems that can be described by a macroscopic order parameter: superfluids and superconductors. For both systems the dynamics may be modelled using non-linear equations of motion, the Gross-Pitaevskii (GP) equation for superfluids and the time-dependent Ginzburg-Landau (TDGL) equation for superconductors. Strictly speaking, these equations are formulated for idealised systems and only give an accurate description under particular conditions. However, they provide sophisticated fluid-dynamical models and can be expected to offer considerable qualitative insight into the physics of quantum fluids.

One of the main issues in this thesis is the mechanism of breakdown of superfluid and superconducting behaviour. In both cases, the onset of dissipation involves the creation, the growth or the motion of quantised vortices [6]. For example, in superfluid helium, vortex rings can be produced experimentally by injecting ions into the fluid [7]. However, the exact mechanism of vortex nucleation is not well-known because existing semi-classical theories of vortex nucleation cannot treat the intermediate states where the vortex loops are small [8]. The advantage of the GP model is that fluid healing and the quantisation of circulation are included explicitly, making it possible to identify a complete path of vortex nucleation.

In superconductors, dissipation is accompanied with the motion of vortices [9]. In commercially used superconductors, pinning sites prevent the vortices from sliding up to a critical current density. The depinning transition involves a complex non-equilibrium dynamics of an elastic lattice through a disordered medium. We will approach the problem by direct numerical solution of the TDGL equations and com-

pare the result to experiments and theoretical studies based on molecular dynamics simulations [10, 11].

In the following sections we shall give a very brief review of the history of experimental and theoretical research on superfluids and superconductors.

1.1 Superfluids

Under normal pressure ^{4}He becomes liquid at 4.211 K and does not freeze even at zero temperature. Below the λ point, $T_c = 2.186$ K, it develops some peculiar properties. Its viscosity and heat capacity become smaller and go to zero for $T \to 0$. On the contrary, the thermal conductivity becomes very large. In this state, often referred to as He-II, the fluid creeps up the walls of the container that holds it and sound waves propagate through it without significant damping. Remarkably, none of these effects can be seen in liquid ^{3}He above a few mK.

In 1939, a few months after the discovery of He-II, Fritz London drew a connection between the experiments and Einstein's earlier work on non-interacting bosons and explained the observations assuming that a macroscopic number of atoms were in the same coherent quantum state. For a non-interacting gas with the mass and density of ^{4}He, the BEC transition would occur at 3.3 K, close enough to the λ point to defend his idea. Soon after, Laszlo Tisza suggested that the He-II phase was made up of two inter-penetrating fluids, a *normal* component that behaves like an ordinary fluid and a *superfluid* component that is characterised by a lack of viscosity. Close to the transition temperature, the superfluid fraction would be small whereas the normal fluid component disappeared as $T \to 0$. On the basis of this model, Tisza was able to predict a new collective excitation of the fluid, the *second sound*, in which the two components oscillate out of phase [12].

The two-fluid model was further developed by Lev Landau who studied the quasi-particle excitation spectrum [13]. Besides phonons, whose dispersion relation is $\epsilon(p) = cp$, he postulated the existence of *rotons* with a dispersion relation of the form $\epsilon(p) = \Delta + p^2/2m$, where m is the mass of a helium atom. At low temperature,

$k_B T \ll \Delta$, phonons dominate and rotons have a negligible contribution to the specific heat. From the excitation spectrum it can immediately be seen that an excitation in the fluid can only be created by a moving object, when its velocity is larger than some non-zero critical velocity, U_c. This is known as the Landau criterion for superfluidity.

Although the two-fluid model was successful in explaining most of the hydro-dynamical properties, a microscopic theory for He-II that would, for instance, be able to explain the excitation spectrum, is difficult to formulate. To this day there is still no satisfactory complete theory for superfluid helium. This is due to the strong inter-particle interactions that result in a depletion of the condensate. Even close to absolute zero, only around 10% of the atoms are in the ground state and fluctuations dominate. In contrast, the fundamental many-body theory of BEC is well understood for a dilute, weakly-interacting gas of bosons where interactions can be treated within the mean-field approximation as a perturbation to the ideal (non-interacting) gas case.

1.1.1 Dilute Bose gases

The first realisation of Bose-Einstein condensation in magnetically trapped alkali vapours in 1995 [14, 15, 16] opened a new chapter of experimental and theoretical research on systems that undergo a Bose-Einstein phase transition. Since then, a spectacular record of experimental and theoretical research has enhanced the knowledge of these systems. At the time of writing, the BEC transition has been demonstrated with the alkali gases ^{87}Rb, ^{23}Na, ^{7}Li, and recently with ^{85}Rb [17] as well as with spin-polarised atomic hydrogen [18] and metastable helium [19, 20]. In the experiments, the atoms are confined in magnetic traps and cooled down to temperatures of the order of μK using elaborate techniques [21].

There is a variety of techniques available to probe the condensate. For example, the atomic cloud can be set into rotation by laser beams and one observes regular arrays of quantised vortices, an unambiguous signature of the quantum nature of

the condensate [22, 23]. In another landmark experiment, a laser beam was swept back and forth through a cylindrical condensate [24]. The measured heating rate revealed the existence of a critical velocity in agreement with the theory [25].

A condensate of ^{7}Li bosons was also utilised to cool down a gas of fermions, ^{6}Li such that the distinct behaviour of bosons and fermions at ultra-low temperatures became evident [26]. It is expected that at even lower temperatures pairs of two ^{6}Li couple to form boson-like *Cooper pairs* that can then condense [27]. The process is known as the BCS transition and occurs, for example, in superfluid ^{3}He and superconductors (see below).

A long-standing goal has been the construction of an *atom laser* that will provide a bright, narrow and continuous beam of coherent atoms. Up to now pulsed [28, 29] and continuous output couplers that can be operated for several hundred milliseconds [30] have been demonstrated.

The attractiveness of atomic vapour condensates is that the dynamics can be accurately described by the Gross-Pitaevskii (GP) equation [31], a form of non-linear Schrödinger equation [32]. Consequently, this system provides a near ideal testing ground for advancing our knowledge of superfluid flow.

1.1.2 The Gross-Pitaevskii equation

A major tool for the theoretical study of weakly-interacting Bose condensates is the Gross-Pitaevskii (GP) equation [32]. Because this equation is used in the following chapters to model superfluids, we shall sketch its derivation.

In the formalism of second quantisation, a many-body problem is described using field operators. One defines creation and annihilation operators, $\hat{\psi}^\dagger$ and $\hat{\psi}$, on the many-particle Hilbert space as linear combinations of single-particle wavefunctions. The operators are chosen in such a way that the commutation relations,

$$\left[\hat{\psi}(\boldsymbol{r}), \hat{\psi}^\dagger(\boldsymbol{r}')\right] = \delta(\boldsymbol{r} - \boldsymbol{r}') \quad \text{and} \quad \left[\hat{\psi}(\boldsymbol{r}), \hat{\psi}(\boldsymbol{r}')\right] = 0 \,, \tag{1.1}$$

are satisfied. The brackets [,] denote the commutator in which the correct quantum statistics for bosons is incorporated. Neglecting spin, the many-particle Hamiltonian of the system can be represented as

$$\begin{aligned} \hat{\mathcal{H}} &= \int \mathrm{d}^3\boldsymbol{r}\ \hat{\psi}^\dagger \left(-\frac{\hbar^2}{2m}\nabla^2 + V(\boldsymbol{r})\right)\hat{\psi}(\boldsymbol{r}) \\ &+ \frac{1}{2}\int \mathrm{d}^3\boldsymbol{r}\ \mathrm{d}^3\boldsymbol{r}'\ \hat{\psi}^\dagger(\boldsymbol{r})\hat{\psi}^\dagger(\boldsymbol{r}')\mathcal{U}(\boldsymbol{r},\boldsymbol{r}')\hat{\psi}(\boldsymbol{r})\hat{\psi}(\boldsymbol{r}')\ , \end{aligned} \tag{1.2}$$

where $V(\boldsymbol{r})$ is an external potential and the inter-particle interactions are represented by $\mathcal{U}(\boldsymbol{r},\boldsymbol{r}')$. The one-particle reduced density matrix can be expressed as a correlation function,

$$\rho_1(\boldsymbol{r},\boldsymbol{r}') = \left\langle \hat{\psi}^\dagger(\boldsymbol{r})\hat{\psi}(\boldsymbol{r}') \right\rangle\ . \tag{1.3}$$

It is possible to find a complete orthonormal basis of single particle wavefunctions $\chi_i(\boldsymbol{r})$ for which the density matrix is diagonal,

$$\rho_1(\boldsymbol{r},\boldsymbol{r}') = \sum_i n_i \chi_i^*(\boldsymbol{r})\chi_i(\boldsymbol{r}')\ , \tag{1.4}$$

where n_i and the basis functions $\chi_i(\boldsymbol{r})$ depend on time in the general case. A system shows Bose-Einstein condensation if any of the eigenvalues n_i is of order of the total number of particles [33]. In this case, it is convenient to write the field operator as a sum of the condensate wavefunction and an operator representing the non-condensed bosons: $\hat{\psi}(\boldsymbol{r}) = \psi(\boldsymbol{r}) + \tilde{\psi}(\boldsymbol{r})$, where $\psi(\boldsymbol{r}) \equiv \chi_i(\boldsymbol{r})$. A pure condensate exhibits perfect spatial phase coherence, a property that is fundamental to BEC.

The GP model neglects the non-condensed atoms and the alkali vapours are solely described by one macroscopic wavefunction. As a further approximation, the inter-particle interactions are treated as collisions of hard-body spheres with infinitesimally small radii,

$$\mathcal{U}(\boldsymbol{r},\boldsymbol{r}') = g\delta(\boldsymbol{r}-\boldsymbol{r}')\ , \tag{1.5}$$

where g is a measure of the effective strength of the interaction. Positive values of g indicate a repulsion between the particles whereas g is negative if the effective interactions are attractive. Substituting into Eq. (1.2) yields

$$\mathcal{H} = \int \mathrm{d}^3\boldsymbol{r} \left(-\frac{\hbar^2}{2m}\psi^*(\boldsymbol{r})\nabla^2\psi(\boldsymbol{r}) + V(\boldsymbol{r})|\psi(\boldsymbol{r})|^2 + \frac{g}{2}|\psi(\boldsymbol{r})|^4 \right) . \tag{1.6}$$

With Heisenberg's relation for the time evolution for a field operator, $\mathrm{i}\partial_t\hat{\psi} = [\hat{\psi}, \hat{\mathcal{H}}]$, one obtains a Schrödinger type equation with an additional non-linear term,

$$\mathrm{i}\hbar\frac{\partial}{\partial t}\psi(\boldsymbol{r},t) = \left(-\frac{\hbar^2}{2m}\nabla^2 + V(\boldsymbol{r}) + g|\psi(\boldsymbol{r},t)|^2 \right)\psi(\boldsymbol{r},t) . \tag{1.7}$$

This equation is known as the Gross-Pitaevskii (GP) equation [31] or as the non-linear Schrödinger equation (NLSE).

The use of Heisenberg's relation presupposes the conservation of energy and number of particles of the system. Gajda and Rzazewski [34] formulated a definition of the Bose-Einstein phase transition for such a *Microcanonical ensemble* of a finite number of bosons. On the contrary, the Bose-Einstein phase transition is usually derived for a grand-canonical ensemble of spin-less particles, i. e. assuming the presence of a temperature and a particle bath [35]. Because the GP model does not include any reservoir of heat or particles, it is inappropriate for modelling the phase transition itself, for example the growth of the condensate out of a 'thermal cloud' of non-condensed particles. The GP equation only describes the dynamics of an already existing condensate in a closed system [33].

In summary, the GP equation provides an accurate description of the time evolution of the condensate if almost all of the particles are in the condensate (no fluctuations); the range of the interactions is small compared to the length scale at which the wavefunction varies; and if the energy and number of particles are conserved. Fortunately, most experiments on trapped alkali vapours condensates lie in this regime [32]. Only recently, an experiment on bosons with attractive interactions demonstrated the limitations of the model. The dynamics of the observed

'bosenova', the collapse of the condensate, cannot be explained by the GP equation [36].

The approximations that lead to the GP equation are not valid for superfluid helium. In this system strong interactions lead to a depletion of the condensate and a different dispersion curve to the dilute Bose gas [6, 7]. A modified GP model which includes the non-local nature of the interactions has been proposed to reproduce the correct dispersion curve [37, 38]. The GP equation can also be extended to describe a finite temperature system, or similarly, the depletion of the condensate due to interactions [39, 40].

1.2 Superconductors

If one immerses mercury that is naturally solid at such low temperatures into liquid helium, its resistance suddenly becomes unmeasurably small. This was first observed by Kamerlingh Onnes in 1911 in Leiden, in the same laboratory in which helium had been liquefied for the first time three years before. Since then, superconductivity has been found in more than a thousand metals, alloys, compounds and even in semiconductors. It was only a few months ago that the phenomenon was discovered in MgB_2 [41]. The high transition temperature of 39 K was a surprise to the superconductivity community and has brought new excitement to the area of basic and applied research on superconducting materials.

Besides the zero resistivity, which is analogous to the flow without viscosity in a superfluid, superconductors show a second remarkable phenomenon known as the Meissner-Ochselfeld effect. If a sample above the transition temperature is placed in a magnetic field, the field lines run through it without any significant deflection (only non-ferromagnetic materials with $\mu \approx 1$ become superconducting). As soon as it is cooled below the critical temperature, the field lines are completely excluded from the bulk. The effect becomes understandable if one assumes persistent currents circulating in a surface layer of the superconductor that prevent external field lines from penetrating into the material. The creation of the currents requires work to be

done which is proportional to the square of the external magnetic field. However, the free energy of the superconducting phase is lower by an amount given by the so-called energy gap, Δ, so that the sample remains superconducting unless the external field exceeds a critical value. This energy gap is zero at the transition temperature and increases with decreasing temperature. Its existence was first explained by Bardeen, Cooper and Schrieffer (BCS) in 1956.

1.2.1 BCS theory

The Bardeen-Cooper-Schrieffer theory interprets the energy gap as the work needed to break a Cooper pair. According to the theory, there is an attractive interaction between pairs of electrons at low temperatures. This interaction can be understood in the following way. One electron perturbs the lattice of the superconductor by attracting the neighbouring ions. In this way it creates its own shallow potential well. The other electron can benefit from this well. However, this simple picture does not explain why only two electrons are involved and why the coupling works over distances as large as 10^4 Å [42].

The electrons in a Cooper pair have opposite spins and equal and opposite linear momenta. Thus, each Cooper pair may be considered as a single particle with zero spin. Such particles obey Bose-Einstein statistics and any number of Cooper pairs can occupy the same quantum state.

The Cooper pairs can also tunnel trough a thin insulating layer. If a dc voltage, V, is applied across such a junction, one observes an alternating current with a frequency given by $2eV/h$ [9]. In 1962 Josephson explained this effect by assigning a phase to the superconductors on both ends of the junction. A voltage shifts the energy levels so that the Cooper pairs on the two sides get out of tune and an ac current flows with a frequency given by the beat frequency between the two sides.

1.2.2 Ginzburg-Landau theory

The superconducting state may also be described by a macroscopic complex pseudo-wavefunction. In the Ginzburg-Landau theory [43] the complex order parameter $\psi(\boldsymbol{r})$ was introduced. Initially, the theory was purely phenomenological. However, in 1959 Gor'kov [44] showed that it was derivable as a rigorous limiting case of the BCS theory. The validity was shown to be restricted to temperatures sufficiently close to the transition temperature, T_c, and to spatial variations of ψ that were not too rapid.

In the Ginzburg-Landau model the local density of superconducting electrons is represented by $|\psi|^2$. According to Gor'kov, $|\psi|^2$ is also proportional to the energy gap. The theory postulates that the free energy of the system coupled with a static magnetic field can be expanded in a series of the form

$$\begin{aligned}\mathcal{F}(\psi, \nabla\psi, \boldsymbol{A}, \nabla\times\boldsymbol{A}) &= a|\psi|^2 + \frac{1}{2}b|\psi|^4 + \frac{\hbar^2}{2m_s}\left|\left(\nabla - \mathrm{i}\frac{e_s}{\hbar}\boldsymbol{A}\right)\psi\right|^2 \\ &\quad + \frac{1}{2\mu_0}|\nabla\times\boldsymbol{A} - \mu_0\boldsymbol{H}|^2,\end{aligned} \tag{1.8}$$

where a and b are phenomenological parameters that depend on external parameters such as temperature, $\boldsymbol{A}$ denotes the vector potential, $\boldsymbol{H}$ an external magnetic field, and e_s and m_s are the effective charge and the effective mass of the Cooper pairs. Below the transition temperature a becomes negative, whereas $b > 0$ for all T.

The field configurations $\psi(\boldsymbol{r})$ and $\boldsymbol{A}(\boldsymbol{r})$ in an equilibrium state are determined by the condition $\delta\mathcal{F}/\delta\psi^* = 0$ and $\delta\mathcal{F}/\delta\boldsymbol{A} = 0$. Explicit expressions of these conditions are

$$\frac{\hbar^2}{2m_s}\left(\nabla - \mathrm{i}\frac{e_s}{\hbar}\boldsymbol{A}\right)^2\psi + |a|\psi - b|\psi|^2\psi = 0 \tag{1.9}$$

$$\frac{1}{\mu_0}\nabla\times(\nabla\times\boldsymbol{A} - \mu_0\boldsymbol{H}) = \frac{\hbar e_s}{2m_s\mathrm{i}}(\psi^*\nabla\psi - \psi\nabla\psi^*) - \frac{e_s^2}{m_s}|\psi|^2\boldsymbol{A}\,. \tag{1.10}$$

Equation (1.10) is Maxwell's equation for the magnetic field and the right hand side is interpreted as the current of superelectrons, $\boldsymbol{j}_s$. In homogeneous regions the

order parameter takes the value of $|\psi|^2 = |a|/b$, which falls to zero at the transition temperature. Equation (1.9) also describes the ground state for a superfluid if one sets $\boldsymbol{A} = 0$. Indeed, the Ginzburg-Landau theory is a very general model for the description of second-order phase transitions. It is used to explain many other critical phenomena such as ferro magnetism or the phase transitions in van der Waals gases and it is also a starting point in string theory [45].

Equations (1.9) and (1.10) have been utilised by many groups to study equilibrium states in a superconductor. However, often one finds several meta-stable states that satisfy these *time-independent* GL equations and it is not clear which of these states will occur in an experiment. An expression for the time evolution of the order parameter is needed that makes it possible to study the transition between meta-stable states driven by changes of external parameters such as magnetic field, voltage or temperature.

The simplest assumption is that the order parameter relaxes towards a *local* minimum of the free energy with a rate proportional to the slope of the free energy [46],

$$\frac{\hbar^2}{2m_s D}\frac{\partial\psi}{\partial t} = -\frac{\partial\mathcal{F}}{\partial\psi^*} , \tag{1.11}$$

where D is a phenomenological diffusion constant that characterises the decay time of an excitation. The relaxation mechanism is due to an interaction with the lattice via exchange of quasi-particles. A more rigorous derivation shows that the time derivative must be replaced in the following way [46]:

$$\partial/\partial t \rightarrow \partial/\partial t + \mathrm{i}e_s/\hbar\Phi , \tag{1.12}$$

where Φ is the electric potential. To the left hand side of equation (1.10), a *normal* current $\boldsymbol{j}_n$ is added to account for non-condensed electrons which obey Ohm's law,

$$\boldsymbol{j}_n = \sigma\boldsymbol{E} = \sigma(-\nabla\Phi - \partial_t\boldsymbol{A}) . \tag{1.13}$$

In summary, the full time-dependent Ginzburg-Landau equations are given by

$$\frac{\hbar^2}{2m_s D}\left(\partial_t + \mathrm{i}\frac{e_s}{\hbar}\Phi\right)\psi = \frac{\hbar^2}{2m_s}\left(\nabla - \mathrm{i}\frac{e_s}{\hbar}\boldsymbol{A}\right)^2\psi + |a|\psi - b|\psi|^2\psi \tag{1.14}$$

$$\frac{1}{\mu_0}\nabla\times(\nabla\times\boldsymbol{A} - \mu_0\boldsymbol{H}) = \boldsymbol{j}_s + \boldsymbol{j}_n\,, \tag{1.15}$$

where

$$\boldsymbol{j}_s = \frac{\hbar e_s}{2m_s \mathrm{i}}(\psi^*\nabla\psi - \psi\nabla\psi^*) - \frac{e_s^2}{m_s}|\psi|^2\boldsymbol{A} \tag{1.16}$$

$$\boldsymbol{j}_n = \sigma(-\nabla\Phi - \partial_t\boldsymbol{A})\,. \tag{1.17}$$

The main difference between equation (1.14) for the order parameter and the NLSE, Eq. (1.7), for the superfluid wavefunction is the missing 'i' in front of the time derivative in the GL model. This profoundly changes the character of the equation from a wave to a diffusion equation.

1.2.3 Extensions to the GL equations

The BCS and GL theories were celebrated as a 'remarkably complete and satisfactory picture' [47] of superconducting phenomena until 1986, when Georg Bednorz and Alexander Müller found a complete new class of superconductors [48], the high-temperature superconductors (HTSC). Although the BCS theory appears to be the correct starting place for understanding these new superconductors, they have many features that are not clearly understood. The main difference between HTSC and ordinary superconductors stems from the layered structure of the materials that causes an anisotropy of the order parameter (d-wave instead of s-wave). To some degree this can be modelled with the TDGL equations by assuming a sinusoidal profile of the coherence length [49].

Many experiments with superconductors are sensitive to thermal fluctuations of the order parameter. According to statistical mechanics the probability of finding the system with a given ψ is proportional to $\exp(-\mathcal{F}(\psi)/k_BT)$. Thus the order parameter ψ_0 that minimises $\mathcal{F}$ is not the only possible solution but simply the most

probable one. The Ginzburg-Landau theory ignores the fact that ψ varies around ψ_0. Close to T_c, where the order parameter is small, fluctuations are substantial and the Landau theory loses its validity. However, for most superconductors, the fluctuations become very small for temperatures just below the critical temperature whereas the fluctuations in superfluid helium dominate at all temperatures. This is believed to be due to the small coherence length of He-II [6]. The finite temperature effects can be simulated by adding small random forces to the TDGL equations [50, 51].

A problem with the TDGL equations stated above is that the Hall effect is not modelled correctly [52]. In Chapter 8 we will discuss the motion of flux lines due to a Lorentz force. According to the TDGL equations, the flux lines drift perpendicular to the current and no Hall voltage can be measured. In experiments, however, a small Hall effect is observed which means that the velocity of the flux lines has a component in direction of the background current. Apparently, the dynamics of the order parameter is not only due to a relaxation towards a minimum of the free energy. Flux can also be carried by the background flow, as in a liquid. To take this into consideration the diffusion constant, D, in the TDGL must be replaced by a *complex* number so that $\arg(D)$ equals the Hall angle [53].

1.3 Structure of this thesis

In this thesis we shall explore some fundamental problems related to superfluidity and superconductivity by solving the appropriate equations of motion for the order parameter. The applied numerical methods are explained in detail in the Appendices.

In Chapter 2, we review the hydro-dynamical properties of the GP model and gather some information on well-known fundamental solutions to the NLSE. Chapters 3 to 5 are concerned with the motion of an object through a quantum fluid. We first study stationary flow solutions around a moving object. In Chapter 4 we utilise the GP equation coupled to an equation of motion for the object to study the response of the

fluid to external forces. The results are compared to experiments on ions dragged through superfluid helium. In Chapter 5, we study the motion of a heavy obstacle for which the back-action of the fluid can be neglected. In Chapter 6 some results are presented on rotating Bose gases in a flat-bottom potential.

In the last two Chapters the properties of the GL equations for superconductivity are examined and the origin of dissipation in a type-II superconductor is investigated. The Conclusion will summarise the results and it will become evident that the numerical solution of equations of motion for the macroscopic order parameter can provide new insight into the physics of condensed quantum systems.

Several parts of this thesis have been published in the following papers:

- *Pressure drag in linear and nonlinear quantum fluids*,
  T. Winiecki, J. F. McCann, and C. S. Adams, Phys. Rev. Lett. **82**, 5186 (1999)
- *Vortex structures in dilute quantum fluids*,
  T. Winiecki and C. S. Adams, Europhys. Lett. **48**, 475 (1999)
- *Vortex shedding and drag in dilute Bose-Einstein condensates*,
  T. Winiecki, B. Jackson, J. F. McCann, and C. S. Adams, J. Phys. B **33**, 4069 (2000)
- *Motion of an object through a quantum fluid*,
  T. Winiecki and C. S. Adams, Europhys. Lett. **52**, 257 (2000)
- *A fast semi-implicit finite difference method for the TDGL equations*,
  T. Winiecki and C. S. Adams, J. Comput. Phys. (submitted).
- *Vortex dynamics, pinning, and critical currents in a Ginzburg-Landau type-II superconductor*,
  T. Winiecki and C. S. Adams, Phys. Rev. Lett. (submitted).

Chapter 2

The Gross-Pitaevskii model

This chapter summarises some interesting properties of the solutions to the Gross-Pitaevskii equation. The dilute Bose-Einstein condensate is identical to a classical Euler fluid except for the quantisation of circulation and the influence of the kinetic energy term appearing in the GP equation. The latter produces fluid healing and shear stresses which enable vortex formation without viscosity. We relate the NLSE to equations known from fluid mechanics. Some fundamental solutions to the GP equation are discussed at the end of this chapter.

2.1 Quantum fluid mechanics

At low temperatures and low densities atoms interact by elastic s-wave scattering, and collisions can be parameterised by a single variable, the scattering length, a. For atoms of mass m, the wavefunction of the condensate, $\psi(\boldsymbol{r},t)$, is given by the solution of the time-dependent Schrödinger equation:

$$\mathrm{i}\hbar\partial_t\psi(\boldsymbol{r},t) = \left[-\frac{\hbar^2}{2m}\nabla^2 + V(\boldsymbol{r},t) + g|\psi(\boldsymbol{r},t)|^2\right]\psi(\boldsymbol{r},t)\ , \tag{2.1}$$

where the wavefunction is normalised to the number of atoms, N, the coefficient of the non-linear term, g, describes the interactions within the fluid, and $V(\boldsymbol{r},t)$ represents external potentials.

2.1.1 Fluid equations

In this section we gather some of the key concepts and equations that relate the NLSE and equations known from fluid mechanics. Classical (isentropic) fluid mechanics is based on two coupled differential equations: one describing the transport of mass, the other the transport of momentum [54]. The relevant quantum variables can be constructed from the wavefunction, $\psi = n^{1/2}\mathrm{e}^{\mathrm{i}S}$: the mass density ρ and momentum current density $\boldsymbol{J}$ are defined according to the Madelung transformation [55],

$$\rho = mn \equiv m\psi^*\psi \quad \text{and} \quad J_k \equiv (\hbar/2\mathrm{i})(\psi^*\partial_k\psi - \psi\partial_k\psi^*) \ , \tag{2.2}$$

where the index k denotes the vector component and n the number density of the particles. The fluid velocity is defined by $v_k \equiv J_k/\rho$, or equivalently in terms of the phase, S, of the wavefunction, $v_k \equiv (\hbar/m)\partial_k S$. Clearly, the velocity field is a potential flow, however it is also compressible and furthermore can support circulation (vorticity) as will be seen.

The conservation of mass (probability), i. e. the continuity equation, follows from the definition of ρ and equation (2.1)

$$\partial_t\rho + \partial_k J_k = 0 \ . \tag{2.3}$$

We use Einstein's summation convention throughout. The conservation of momentum equation may be found by considering the rate of change of the momentum current density

$$\partial_t J_k + \partial_j T_{jk} + \rho\partial_k(V/m) = 0 \ , \tag{2.4}$$

where the momentum flux density tensor takes the form

$$T_{jk} = \frac{\hbar^2}{4m}(\partial_j\psi^*\partial_k\psi - \psi^*\partial_j\partial_k\psi + \text{c.c.}) + \frac{g}{2}\delta_{jk}|\psi|^4 \ . \tag{2.5}$$

This can be rewritten as

$$T_{jk} = \rho v_j v_k - \sigma_{jk} \ , \tag{2.6}$$

where the stress tensor σ_{jk} is given by

$$\sigma_{jk} = -\tfrac{1}{2}\delta_{jk} g(\rho/m)^2 + (\hbar/2m)^2 \rho \partial_j \partial_k \ln \rho \ . \tag{2.7}$$

2.1.2 Pressure, sound and force

The form of equations (2.3), (2.4), and (2.6) is identical to those for classical fluid flow [54], the difference emerges from the nature of the stress, equation (2.7). A classical ideal fluid is characterised by $\sigma_{jk} = 0$, for all j, k. In a viscous fluid, the shear stress ($\sigma_{jk}, j \neq k$) is produced by velocity gradients between neighbouring streams such that $\sigma_{jk} = \eta(\partial_j v_k + \partial_k v_j)$, where η is the coefficient of viscosity. This creates a frictional force which gives rise to energy loss. In a pure dilute Bose-Einstein condensate there is no frictional viscosity, but a shear stress arises from density gradients, the second term in equation (2.7). This property gives rise to the possibility of vortex formation and drag without viscosity.

The pressure (normal stress, $-\sigma_{jk}, j = k$) within the quantum fluid has a non-linear and non-local dependence on the density,

$$p = \tfrac{1}{2} g(\rho/m)^2 - (\hbar/2m)^2 \rho \nabla^2 \ln \rho \ . \tag{2.8}$$

The second term, called the quantum pressure, is weak in homogeneous regions of the fluid, that is far from obstacles or boundaries, vortex lines or shocks. The essential difference between interacting and noninteracting (ideal) fluids is the existence of interaction pressure which supports sound propagation. The speed of sound in a fluid is given by $c = \sqrt{\partial p / \partial \rho}$ [54, 56]. For small amplitude waves of the form $\rho(x) = \rho_0 + \varepsilon \sin kx$, we obtain the Bogoliubov expression for the speed of sound

$$c(k) = \frac{\omega(k)}{k} = \sqrt{\frac{g}{m^2}\rho_0 + \left(\frac{\hbar}{2m}\right)^2 k^2} \ . \tag{2.9}$$

The dispersion relation $\omega(k)$ is linear for small k and approaches the free-particle dispersion law for short wavelengths. The Landau criterion for superfluidity is based on a non-zero slope of the excitation spectrum in the limit $k \to 0$ [6]. Therefore, we expect superfluid behaviour for any $g > 0$ with a Landau critical velocity of $v_L = \sqrt{g\rho_0}/m$.

The force on a sub-volume of the condensate can be calculated by integrating Eq. (2.4). One finds for the k-th component of the force,

$$F_k = \partial_t \int_\Omega \mathrm{d}^3 r J_k = -\int_{\partial\Omega} \mathrm{d}^2 r \; n_j T_{jk} - \int_\Omega \mathrm{d}^3 r \; \rho \partial_k (V/m) \; , \tag{2.10}$$

where $\partial\Omega$ is the surface of the volume Ω, n_j is the j-component of the normal vector to $\partial\Omega$, and $\mathrm{d}^2 r$ is a surface element. The first term on the right-hand side arises from pressures acting on the boundary of the considered volume whereas the second term is due to forces exerted by external potentials.

2.1.3 Quantisation of circulation

The quantum Euler equation follows from combining the equations describing the conservation of mass and momentum, (2.3) and (2.4), along with the identity

$$\rho^{-1} \partial_j [\rho \partial_j \partial_k \ln \rho] = 2 \partial_k [\rho^{-\frac{1}{2}} \partial_j \partial_j \rho^{\frac{1}{2}}] \; , \tag{2.11}$$

allowing the momentum equation to be written as

$$\partial_t v_k + v_j \partial_j v_k + \partial_k [g\rho/m^2 - (\hbar^2/2m)\rho^{-\frac{1}{2}} \partial_j \partial_j \rho^{\frac{1}{2}} + V/m] = 0 \; . \tag{2.12}$$

The conservation of energy (Bernoulli equation) then follows as an integral of Euler's equation, or more directly from the real part of equation (2.1):

$$\hbar \partial_t S + \tfrac{1}{2} m v^2 + g\rho/m - (\hbar^2/2m)\rho^{-\frac{1}{2}} \nabla^2 \rho^{\frac{1}{2}} + V = 0 \; . \tag{2.13}$$

For steady flow, in which $\boldsymbol{v}$ and ρ are independent of time, the phase S changes linearly in time, $S = -\mu t$, where μ is the chemical potential. The Bernoulli equation

then takes the form

$$\tfrac{1}{2}mv^2 + g\rho/m - (\hbar^2/2m)\rho^{-\frac{1}{2}}\nabla^2\rho^{\frac{1}{2}} + V = \text{const.} \tag{2.14}$$

Perhaps the most significant quantum effect on the mechanics of the fluid is the quantisation of angular momentum. The circulation is given by

$$\Gamma = \oint \mathrm{d}\boldsymbol{r} \cdot \boldsymbol{v} = (\hbar/m)2\pi s \ , \qquad s = 0, 1, 2, \dots \ , \tag{2.15}$$

where the closed contour joins fluid particles. The conservation of angular momentum (Kelvin's theorem) follows from Euler's equation (2.12) and states that the circulation around a closed 'fluid' contour does not change in time. This means that within the fluid vortex lines must created in pairs which emerge from a point. The exception is at boundaries, where the wavefunction is clamped to zero and no closed fluid loop can be drawn, e.g. at the surface of an impenetrable object [54], or at the edge of a trapped condensate [57].

2.2 Choice of units

For a homogeneous fluid flow it is convenient to re-scale length and velocity in terms of the healing length, $\xi = \hbar/\sqrt{\rho_0 g}$, and the asymptotic speed of sound, $c = \sqrt{\rho_0 g/m^2}$, respectively. In this case, equation (2.1) becomes

$$\mathrm{i}\partial_t\tilde{\psi}(\boldsymbol{r},t) = \left[-\tfrac{1}{2}\nabla^2 + V(\boldsymbol{r}) + |\tilde{\psi}(\boldsymbol{r},t)|^2\right]\tilde{\psi}(\boldsymbol{r},t) \ , \tag{2.16}$$

where $\tilde{\psi} = \psi/\sqrt{n_0}$ and $n_0 = \rho_0/m$ is the asymptotic number density. Unless otherwise stated we use these units throughout and write ψ instead of $\tilde{\psi}$.

For all particle masses and interaction strengths the NLSE can be reduced to a dimensionless form which implies that, in principle, all weakly-interacting Bose condensates exhibit exactly the same physical behaviour at the appropriate scales of time and space. If n_0 is taken to be the asymptotic density at infinity, the asymptotic mass density is $\rho = mn_0 = (\hbar n_0\xi^2/c)/\xi^3$. In the reduced unit system ξ^3 is the

unit of volume, therefore, mass is measured in units of $\hbar n_0 \xi^2/c$. It follows that the units of mass flux per unit area, momentum flux per unit area and force are $\hbar n_0/\xi$, $\hbar n_0 c/\xi$, and $\hbar n_0 c\xi$, respectively. Accordingly, momentum and energy are measured in multiples of $\hbar n_0 \xi^2$ and $\hbar n_0 c\xi^2$, respectively.

For a dilute alkali gas, the number density ranges from $n_0 = 10^{11}$ cm^{-3} to 5×10^{15} cm^{-3} [33]. The speed of sound and the healing length are of order of $c = 6.2$ mm s^{-1} and $\xi = 0.3$ μm, respectively [24].

To convert between dimensionless units and values for He-II, one may use the measured values of the number density, $n_0 = 2.18 \times 10^{28}$ m^{-3}, the quantum of circulation, $\kappa = h/m = 9.98 \times 10^{-8}$ m^2 s^{-1}, and the healing length $\xi/\sqrt{2} = 0.128$ nm [58] leading to a mass unit, $\tilde{m} = mn_0\xi^3 = 0.13m$, where m is the mass of a helium atom and a speed of sound of $c = 88$ m s^{-1} which is significantly less than the measured value of 238 m s^{-1}. The origin of this disagreement probably lies in the GP model's simplified description of the inter-particle interactions that cause the propagation of sound. Another reason could be the large number of atoms that are not condensed but still contribute to the transport of sound.

2.3 Coordinate systems and Galilean transformation

Consider an object moving through a homogeneous condensate with velocity $\boldsymbol{U}$. The GP equation takes the form

$$\mathrm{i}\partial_t \psi(\boldsymbol{r},t) = \left(-\frac{1}{2}\nabla^2 + V(\boldsymbol{r}-\boldsymbol{U}t) + |\psi(\boldsymbol{r},t)|^2\right)\psi(\boldsymbol{r},t)\ . \tag{2.17}$$

The wavefunction $\psi(\boldsymbol{r})$ describes the condensate around a moving body in the fluid rest frame F and is suppressed near $\boldsymbol{r} = \boldsymbol{U}t$ (see Fig. 2.1(c)) due to the potential term sketched in figure 2.1(b). In the frame of the obstacle F' moving with velocity $\boldsymbol{U}$ with respect to F, $\boldsymbol{r}' = \boldsymbol{r} - \boldsymbol{U}t$ and $t' = t$, the statement of Galilean invariance has the form: if $\psi(\boldsymbol{r})$ is solution to Eq. (2.17), then

$$\mathrm{i}\partial_{t'} \psi'(\boldsymbol{r}',t') = \left(-\frac{1}{2}\nabla'^2 + V(\boldsymbol{r}') + |\psi(\boldsymbol{r}',t')|^2\right)\psi(\boldsymbol{r}',t')\ , \tag{2.18}$$

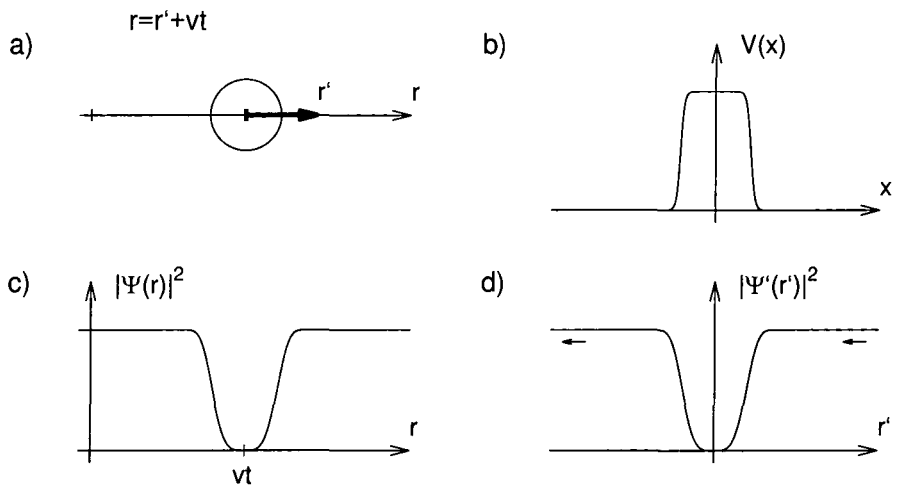

Figure 2.1: (a) Shows the relation of the fluid rest frame F to the object frame F', (b) Typical shape of the potential well used to simulate the effect of an object in a condensate, (c) and (d) Appearance of wavefunctions in F and F'

in which

$$\begin{aligned} \psi'(\boldsymbol{r}',t') &= \exp(-\mathrm{i}\boldsymbol{U}\cdot\boldsymbol{r}' - \tfrac{\mathrm{i}}{2}\mathrm{U}^2t')\psi(\boldsymbol{r}'+\boldsymbol{U}t',t') \\ &= \exp(-\mathrm{i}\boldsymbol{U}\cdot\boldsymbol{r}' - \tfrac{\mathrm{i}}{2}\mathrm{U}^2t')\psi(\boldsymbol{r},t)\ . \end{aligned} \tag{2.19}$$

The reciprocal relation follows from exchanging primed and unprimed coordinates and the mapping $\boldsymbol{U} \to -\boldsymbol{U}$:

$$\begin{aligned} \psi(\boldsymbol{r},t) &= \exp(+\mathrm{i}\boldsymbol{U}\cdot\boldsymbol{r} - \tfrac{\mathrm{i}}{2}U^2t)\psi'(\boldsymbol{r}-\boldsymbol{U}t,t) \\ &= \exp(+\mathrm{i}\boldsymbol{U}\cdot\boldsymbol{r} - \tfrac{\mathrm{i}}{2}\mathrm{U}^2t)\psi'(\boldsymbol{r}',t')\ . \end{aligned} \tag{2.20}$$

The phase gradient of the wavefunction in the object frame at infinity can be eliminated by adding a gradient term to the NLSE so that $\tilde{\psi}'(\boldsymbol{r}',t') = \psi(\boldsymbol{r}'+\boldsymbol{U}t',t')$ is the solution to the equation

$$\mathrm{i}\partial_{t'}\tilde{\psi}'(\boldsymbol{r}',t') = \left(-\frac{1}{2}\nabla'^2 + V(\boldsymbol{r}') + |\tilde{\psi}(\boldsymbol{r}',t')|^2 + \mathrm{i}\boldsymbol{U}\cdot\nabla'\right)\tilde{\psi}'(\boldsymbol{r}',t')\ . \tag{2.21}$$

Here $\tilde{\psi}'(r',t')$ can also be interpreted as the wavefunction in F written down in variables $\boldsymbol{r}'$ and t'.

The following chapter is concerned with the time-independent solutions in the moving frame that are often called *solitary wave solutions* to the NLSE. They can be

written as $\tilde{\psi}'(r',t') = \tilde{\phi}'(r')\mathrm{e}^{-\mathrm{i}\mu t'}$. The chemical potential is constant in space and equal to one if the density of the wavefunction is one at infinity. Omitting the primes, the equations for solitary wave solutions moving with velocity U reads

$$\phi(\boldsymbol{r}) = \left(-\frac{1}{2}\nabla^2 + V(\boldsymbol{r}) + |\phi(\boldsymbol{r})|^2 + \mathrm{i}\boldsymbol{U}\cdot\nabla\right)\phi(\boldsymbol{r}) \ . \tag{2.22}$$

2.4 Lagrangian

The Lagrangian density of the NLSE (2.16) in scaled units is given by

$$\mathcal{L}(\psi,\nabla\psi,\dot{\psi}) = \mathrm{i}\psi^*\dot{\psi} - \frac{1}{2}\nabla\psi^*\nabla\psi - V\psi^*\psi - \frac{1}{2}\left(\psi^*\psi\right)^2 \ . \tag{2.23}$$

Note the $|\psi|^4$ dependence of the free energy according to the Ginzburg-Landau theory, Eq. (1.8). From the Hamiltonian, $\mathcal{H} = \int \mathrm{d}^3r[(\partial\mathcal{L}/\partial\dot{\psi})\dot{\psi} - \mathcal{L}]$, we define the energy and momentum density of the fluid.

2.4.1 Energy

The energy relative to the ground state (i.e. $\psi \equiv 1$ and $V = 0$) having the same number of particles, is defined by

$$\mathcal{E} = \int \mathrm{d}^3r \left[\frac{1}{2}|\nabla\psi|^2 + V|\psi|^2 + \frac{1}{2}\left(|\psi|^2 - 1\right)^2\right] \ . \tag{2.24}$$

Any deviation of the local particle density $|\psi|^2$ from 1 constitutes an excitation. The first term in Eq. (2.24) can be written as

$$\frac{1}{2}|\nabla\psi|^2 = \frac{\left(\nabla|\psi|^2\right)^2}{8|\psi|^2} + \frac{|\psi|^2}{2}\left(\frac{\mathrm{i}}{2|\psi|^2}(\psi\nabla\psi^* - \psi^*\nabla\psi)\right)^2 \tag{2.25}$$

$$= \frac{(\nabla n)^2}{8n} + \frac{n}{2}v^2 \ , \tag{2.26}$$

where $\boldsymbol{v} = \nabla S$ and $n = |\psi|^2$ are the local velocity and density, respectively. It contains the classical kinetic energy of the particles as well as an energy due to density fluctuations.

2.4.2 Momentum

The momentum is given by

$$\boldsymbol{P} = -\frac{\mathrm{i}}{2}\int \mathrm{d}^3r \left\{\psi^*\nabla\psi - \psi\nabla\psi^*\right\} . \tag{2.27}$$

Eq. (2.24) may be re-written using Eq. (2.22) for time-independent wavefunctions in a frame moving with velocity U:

$$\mathcal{E} = \int \mathrm{d}^3r \left\{\frac{1}{2}\left(1 - |\phi|^4\right)\right\} + \boldsymbol{U}\cdot\boldsymbol{P} . \tag{2.28}$$

Here, partial integration has been employed and the surface terms proportional to $\nabla\phi$ have been assumed to be zero.

2.4.3 Dispersion curve

Consider a class of solitary solutions to the equation $\phi = -\frac{1}{2}\nabla^2\psi + |\phi|^2\psi + V\psi + \mathrm{i}U\partial_z\phi$, moving along the z-direction for different values of U. One expects that for an infinitesimal change of the velocity, $U \to U + \delta U$, the wavefunction adapts steadily, $\phi \to \phi + \delta\phi$, where $\delta\phi$ and all its derivatives fall to zero at least quadratically at large distances from the object V. The change in momentum in the z-direction is then given by

$$\begin{aligned} \delta P_z &= P_z(\phi + \delta\phi) - P_z(\phi) && (2.29)\\ &= -\mathrm{i}\int \mathrm{d}^3r \left(\delta\phi^*\partial_z\phi - \delta\phi\partial_z\phi^*\right) . && (2.30) \end{aligned}$$

Using equation (2.22) and after partial integration, we find for the energy of the flow

$$\begin{aligned} \delta\mathcal{E} &= \int \mathrm{d}^3r \left(\delta\phi^*\left(-\frac{1}{2}\nabla^2\phi + |\phi|^2\phi + V\phi - \phi\right) + \right.\\ &\qquad \left. \delta\phi\left(-\frac{1}{2}\nabla^2\phi^* + |\phi|^2\phi^* + V\phi^* - \phi^*\right)\right)\\ &= \int \mathrm{d}^3r \left(\delta\phi^*\left(-\mathrm{i}U\partial_z\phi\right) + \delta\phi\left(+\mathrm{i}U\partial_z\phi^*\right)\right) \end{aligned}$$

$$= U\ \delta P_z\ . \tag{2.31}$$

This means the slope of the dispersion curve for solitary wave solutions is always equal to the group velocity U of the solution.

2.5 Simple solutions to the NLSE

Here we present some special solutions to the NLSE in simple geometries. Many of the properties of these solutions will appear throughout the thesis.

2.5.1 Trapped BECs

Most of the numerical work employing the GP equation has been concerned with BECs that are confined in a potential well, V,

$$\mathrm{i}\partial_t\psi = -\nabla^2\psi + V\psi + g|\psi|^2\psi\ . \tag{2.32}$$

Here V is an ellipsoid quadratic potential of the form $V = \epsilon_x x^2 + \epsilon_y y^2 + \epsilon_z z^2$ and g determines the nature of the inter-particle interaction with $g = 0$ for non-interacting bosons and $g = 1$ or -1 (in dimensionless units) for repulsive and attractive interactions, respectively. Fig. 2.2 shows the ground state solutions in a spherical trap for different interactions. The number of particles, $\int \mathrm{d}^3x|\psi|^2$, is the same in all cases.

In the case of an attractive inter-particle potential, $g = -1$, both the interaction and the trap potential push the wavefunction towards the centre of the trap. However, up to a critical number of particles the kinetic energy term due to the curvature of the wavefunction prevents the condensate from collapsing. Let us approximate ψ by a Gaussian, $a\exp\left(-(\frac{x}{b})^2\right)$ that is normalised to N. The energy of the condensate is given by

$$\mathcal{E}(b,N) = 4\pi\int_0^\infty r^2\mathrm{d}r\left\{|\nabla\psi|^2 + r^2|\psi|^2 - \frac{1}{2}|\psi|^4\right\} \tag{2.33}$$

$$= N\left(\frac{3}{b^2} + \frac{3}{4}b^2 - \frac{N}{2\pi^{3/2}b^3}\right)\ . \tag{2.34}$$

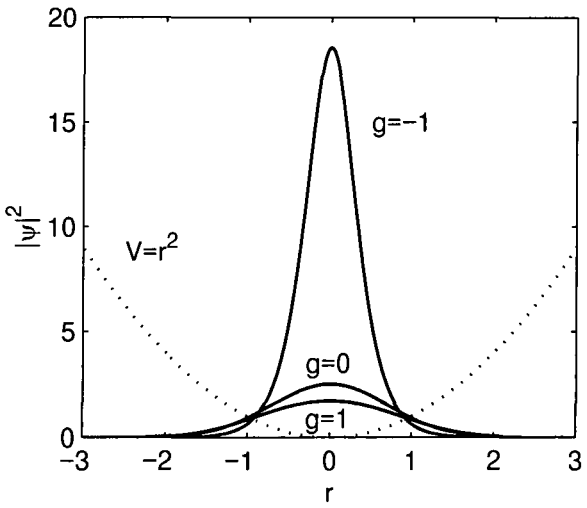

Figure 2.2: Ground state solutions in a spherical trap. A positive scattering length pushes the particles to the edges of the trap whereas for attractive interactions the distribution is narrower. For $g = 0$, the ground state is a Gaussian. The number of particles is normalised to 14 in each case.

We find that there exists a local minimum in the energy for a certain width b of the wavefunction for values of $N < \sqrt{(8\pi)^3/\sqrt{5^5}} \approx 16.9$. From the numerical solution of the wave equation (2.32) we find that the condensate collapses for particle numbers $N > 14.4$, a value close to the one predicted above. The existence of a critical number of atoms in condensates with negative scattering length has been confirmed in experiments [59]. In general, the criterion for collapse depends on the dimensionality and asymmetry of the trap [60]. In the absence of a trap ($V = 0$) condensates with negative interactions are unstable whereas bosons with positive interaction strength form a homogeneous condensate. In the following we will focus on the case $g = 1$.

2.5.2 Objects and walls

A potential term V in the NLSE suppresses the density of the wavefunction and can therefore be used to simulate the effect of a foreign object such as a far detuned laser beam in the condensate. An infinite potential barrier is simulated by applying the condition $\psi = 0$ at the edge of an object. The wavefunction recovers to its mean

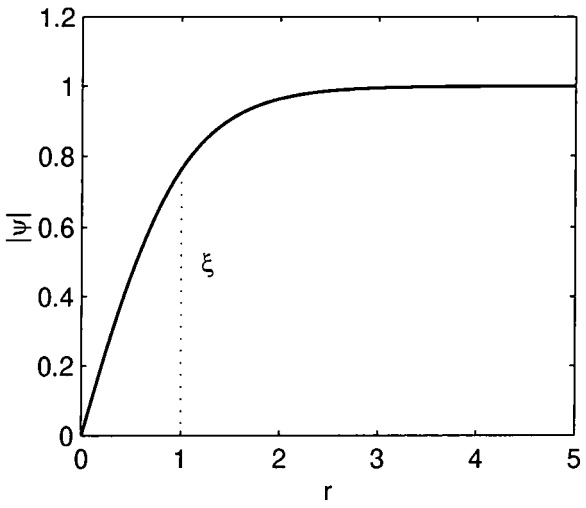

Figure 2.3: The wavefunction recovers from zero to its mean value within a couple of healing lengths. The slope at the origin equals 1.

value, 1 in dimensionless units, within a length scale given by the healing length, ξ. Fig. 2.3 shows a one-dimensional solution to the NLSE with zero boundary condition for the wavefunction at the origin. The solution is given by $\psi(x) = \tanh(x)$.

2.5.3 Vortex tubes and rings

In the Madelung transformation, a gradient in the phase of ψ is interpreted as the local velocity of the fluid. This picture implies that the circulation of the fluid must be quantised and fully contained in one-dimensional so-called vortex lines in space. Assume a wavefunction of the form $\psi(r,\theta) = \rho^{1/2}(r)\exp(im\theta)$, where m is an integer and r measures the distance from the vortex line. The circulation defined in (2.15) is given by $\kappa = 2\pi m$. The density $\rho^{1/2}(r)$ close to the vortex core can be written as an expansion

$$\rho^{1/2}(r) = \sum_{i=0}^{\infty} a_i r^i \ . \tag{2.35}$$

Substituting this Ansatz into the NLSE, we find that coefficients with $i < |m|$ are zero. The exact density profile inside a vortex core with $|\kappa| = 2\pi$ is shown in Fig. 2.4 (solid line). The broken and dotted lines show the series expansion up to the 3$^{\text{rd}}$ and

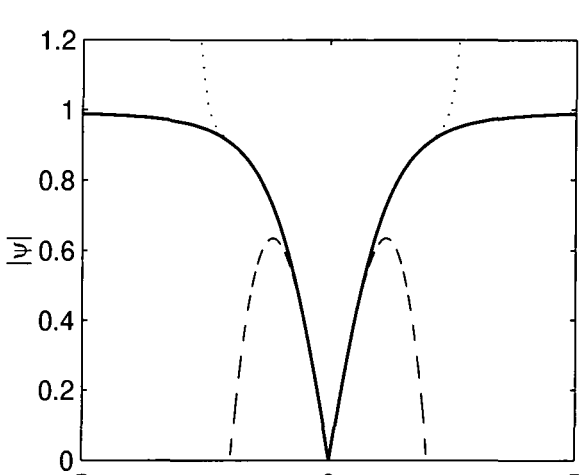

Figure 2.4: The density in a vortex core (solid line). The slope at the origin is about 0.824, smaller than for the tanh solution due to the centrifugal force. The broken (dotted) line show the series expansion, Eq. (2.35) in 3^{rd} (25^{th}) order.

25^{th} order, respectively. The velocity profile around a vortex is given by $1/r$. Vortex tubes therefore constitute one-dimensional singularities in the superfluid velocity.

The mere existence of stable vortices and persistent currents implies the superfluid nature of the liquid.

A vortex tube can be bent to a circular shape to form a vortex ring. Fig. 2.5 shows a surface plot of ring solutions with circulation, $\kappa = 2\pi$, 4π, and 6π. A superfluid vortex ring moves with a constant velocity through the fluid. This self-induced motion is exactly analogous to the propagation of vortex rings in classical fluids. Here, the vortex rings are solitary wave solution to the NLSE in the sense that the they do not change their shape or circulation due to internal friction. In the appropriate frame, a vortex ring is a stationary, time-independent solution to the NLSE.

The corresponding 2D solitary wave solutions are vortex pairs consisting of two vortex tubes with anti-parallel circulation. The flow induced by one of the vortices pushes the other one forward in a direction perpendicular to the circulation and perpendicular to the line that connects the two cores.

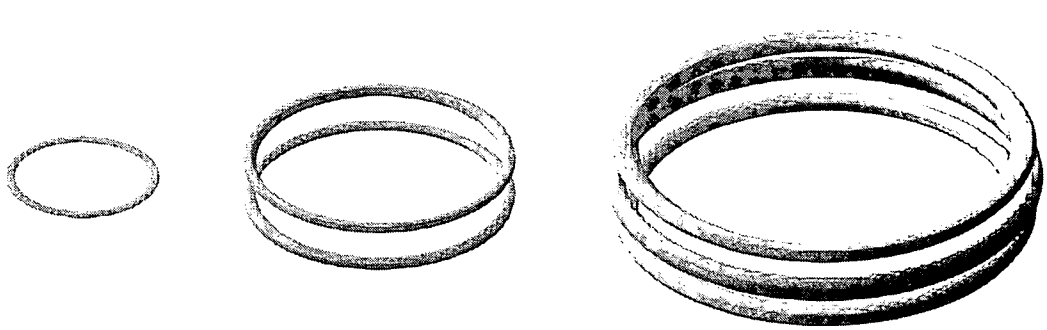

Figure 2.5: Surfaces of constant density ($|\psi|^2 = 0.02$) for vortex rings with $\kappa = 2\pi$, 4π, and 6π for $v = 0.5$. The motion is parallel to the axis of the rings. The core structure is only resolved at very low density: the surface density surface for $|\psi|^2 = 0.08$ appears as a single ring in each case.

The double ($\kappa = 4\pi$) and triple ($\kappa = 6\pi$) rings only exist for $U < 0.56$ and $U < 0.67$, and their cores consists of 2 and 3 lines of zero density, respectively. The separation of the density minima increases with decreasing ring radius, suggesting that it results from the interaction between segments of the ring. For $\kappa = 6\pi$, the central minima has a larger radius (Fig. 2.5). Similar core structures are also found in the corresponding 2D solutions. Although vortex rings with multiple circulation have higher energy ($\mathcal{E} \propto \kappa^2$) than the corresponding number of single rings ($\mathcal{E} \propto \kappa$), we find that they are stable when subject to a perturbation in a time-dependent simulation. Similar robustness has also been found for vortex lines with multiple circulation [61].

Fig. 2.6 shows a plot of the ring propagation velocity and momentum as a function of ring radius, R. For $R > 5$, the velocity can predicted accurately by the expression

$$U = \kappa \left[\ln(8R/a) - b\right] / 4\pi R \,, \tag{2.36}$$

where a is the core radius ($a = 1/\sqrt{2}$ in our units) and b is a constant which depends on the structure of the core ($b = 0.25$ for a classical fluid, whereas $b = 0.615$ has been predicted for a dilute quantum fluid [62]). Numerical fits give $b = 0.615$ (as expected), 1.58, and 2.00 for $\kappa = 2\pi$, 4π and 6π, respectively. For $\kappa = 2\pi$ (single ring), the ring collapses (i.e. the on-axis density becomes zero) when $U = 0.88$, however, the 'collapsed ring' leaves a lower density region, termed a *rarefaction*

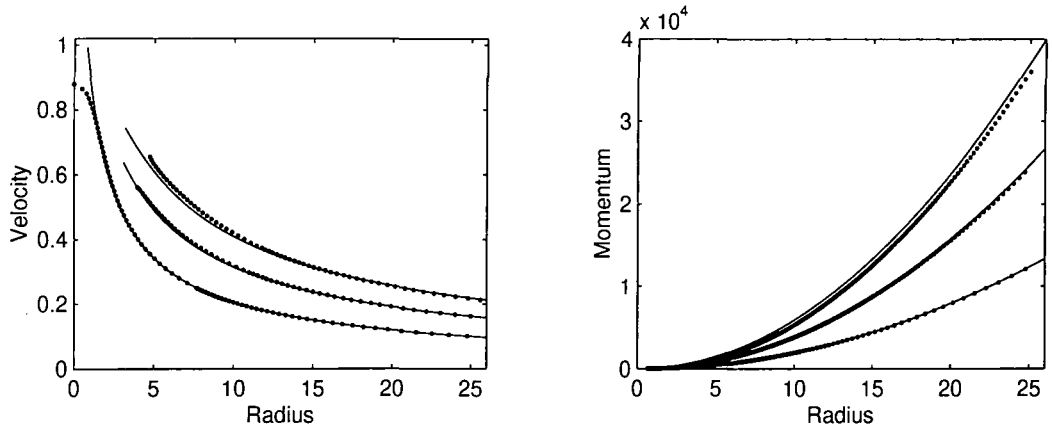

Figure 2.6: Vortex ring velocity (left) and momentum (right) for $\kappa = 2\pi$, 4π, and 6π: The numerical data (dots) are compared to $U = \kappa\left[\ln(8R/a) - b\right]/4\pi R$ ($a = 1/\sqrt{2}$, $b = 0.615$, 1.58, and 2.00), and $P = \pi\kappa R^2$, respectively.

pulse by Jones and Roberts [63] which gradually fills up as the velocity approaches the speed of sound.

A very good estimate for the momentum of a vortex ring is given by the classical formula [7]:

$$P = \kappa\pi R^2 \ . \tag{2.37}$$

For small radius the momentum is slightly smaller due to the hollow core.

2.5.4 1D Solitary wave solutions

The rarefaction pulses or 'collapsed vortex rings' mentioned above have very similar behaviour to one-dimensional solitary wave solutions to the NLSE given by

$$\psi(x,t) = \left[\sqrt{1-U^2}\,\tanh\left(\sqrt{1-U^2}(x-Ut)\right) + iU\right] \mathrm{e}^{-it} \ . \tag{2.38}$$

The density and the local velocity, i.e. the gradient of the phase, are plotted in figure 2.7. The density dips shown in figure 2.7 (a) propagate with a constant velocity U. Their depth decrease with increasing velocity and the wave solution becomes equal to 1 at the speed of sound. In analogy to optical solitons, solitons

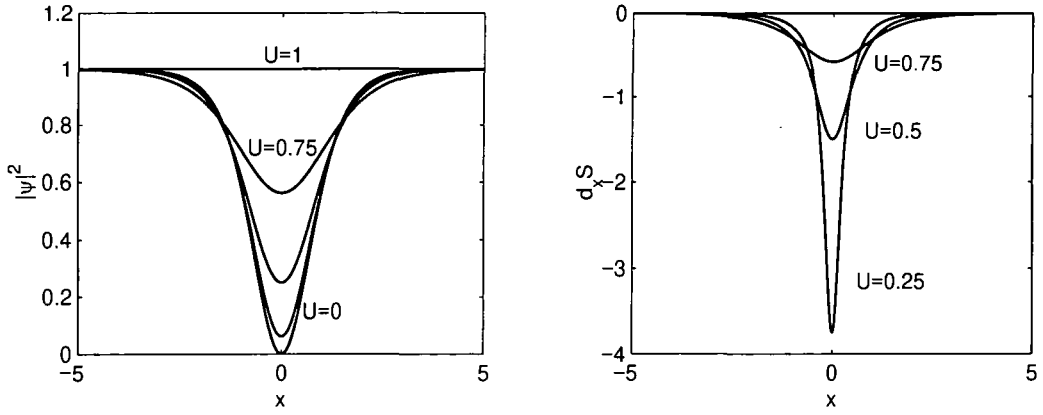

Figure 2.7: Density (left) and local velocity (right) of 1D soliton solutions to the NLSE for different group velocities U.

with zero density ($U = 0$) are termed *black* solitons in contrast to *grey* solitons for $0 < U < 1$.

It is interesting to note, that the local or phase velocity has a different sign to the group velocity U. Assuming that the density wave in figure 2.7 (a) is moving to the right with velocity U, the individual particles of the fluid are moving to the left through the density hollow reaching the largest velocity in the region of lowest density. The phase velocity is given by $-\pi\delta(x)$ for a black soliton.

2.6 Summary

We have reviewed the fluid properties of the Gross-Pitaevskii model and presented some fundamental solutions to the equations. We have investigated vortex line and ring structures and found that vortex tubes with multiple circulation consist of separate minima. In the following chapters we will focus on the flow of a quantum fluid around moving objects.

Chapter 3

Motion of an object through a quantum fluid: The force free case

Vortex structures in dilute quantum fluids are studied using the time-independent Gross-Pitaevskii equation. For a spherical object, we study encircling and pinned ring solutions, and determine their excitation energies as a function of velocity for both penetrable and impenetrable objects. The ring and laminar flow solutions converge at a critical velocity, which decreases with increasing object size. We also study the vortex solutions associated with flow past a surface bump which indicate that surface roughness also reduces the critical velocity.

3.1 Introduction

Vortex solutions of the NLSE equation have been studied for a number of simple geometries. Flow past an object has been studied in one [64, 65] and two dimensions [66], and it is found that stationary vortex solutions exist only for motion slower than a critical velocity. Above this velocity, one observes the periodic emission of vortices leading to a pressure imbalance which produces drag on the object (Chapter 4). Consequently, the critical velocity also determines the transition between superfluid and normal flow.

In the following section, we investigate stationary vortex solutions near an object in three dimensions. For a spherical object there are two vortex solutions: the *encircling ring*, where the object is positioned at the centre of the ring; and the *pinned ring*, where the object lies within the core of the vortex line. For all object potentials laminar flow evolves smoothly into the encircling ring solution. Finally, we study flows parallel to a plane and illustrate the effect of surface roughness on the critical velocity, which may have important implications for the threshold of dissipation in superfluids [67].

All results presented below are calculated by numerically solving the time-independent Gross-Pitaevskii equation,

$$\phi(\boldsymbol{r}) = \left[-\frac{1}{2}\nabla^2 + V(\boldsymbol{r}) + |\phi(\boldsymbol{r})|^2 + \mathrm{i}\boldsymbol{U}\cdot\nabla\right]\phi(\boldsymbol{r}) \ , \tag{3.1}$$

where $\phi(\boldsymbol{r})$ is the wavefunction in the fluid rest frame written in terms of the object frame coordinates, see Appendix 1.

3.2 Motion of a sphere

The free ring solutions discussed in chapter 2 are modified by the presence of an object or surface. In this section, we present results for a spherical object with radius $R = 3.3$ and potential V, i. e. $V(r) = 1$ $(r \leq R)$ and $V(r) = 0$ $(r > R)$ moving with velocity U. Fig. 3.1 shows surface density images of the three possible solutions: *laminar flow*; the *pinned ring* or *vortex loop*; and the *encircling ring* (the corresponding 2D solutions: laminar flow; a free and a bound vortex, and a vortex pair, were studied by Huepe and Brachet [66]). Fig. 3.2 shows a section of the velocity field pattern around the obstacle for each case. As the velocity increases, the ring shrinks in a manner similar to that of a free vortex ring (see Fig. 2.6 (left)). Close to the critical velocity, the vortex core merges into the surface of the object and the flow patterns converge (Fig. 3.2 lower).

The pinned ring solution merges into the encircling ring solution far below the critical velocity as illustrated in Fig. 3.3. The left and the middle figure show the core of

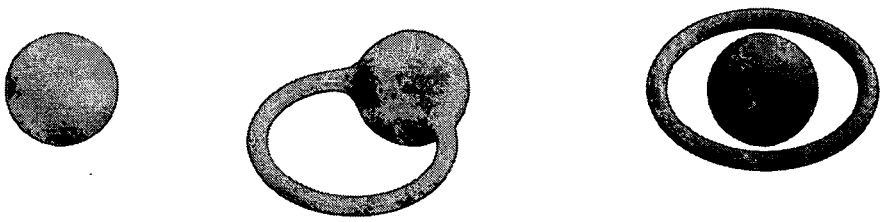

Figure 3.1: Surfaces of constant density ($|\phi|^2 = 0.25$) showing the three steady-state solutions associated with motion of a spherical object: from left to right, laminar flow; pinned ring; encircling ring.

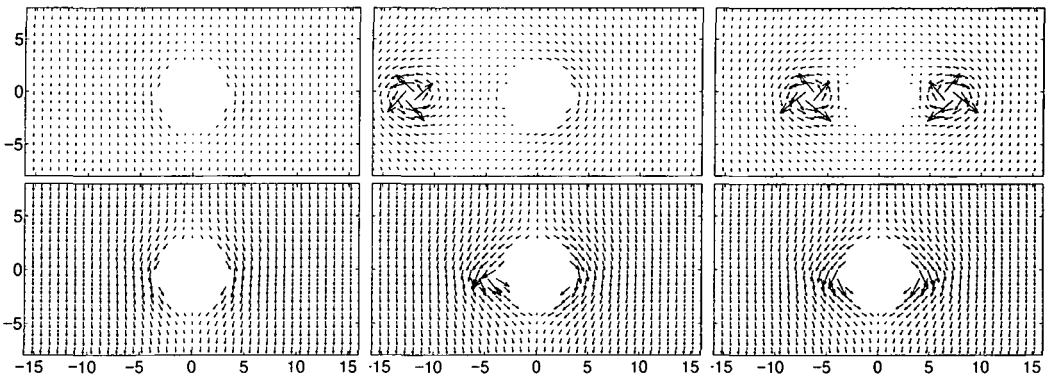

Figure 3.2: The velocity field pattern in the equatorial plane of a spherical object with radius $R = 3.3$ for $U = 0.3$ (above) and $U = 0.56$ (below) (the critical velocity, $U_c = 0.71$). The three columns correspond to laminar flow (left), the pinned ring (middle), and the encircling ring (right). Note the circulation around the object in the pinned ring solution. Only one quarter of actual grid points are shown.

vortex rings at $U = 0.4$ and $U = 0.54$, respectively and the object pinned to it. At low velocities, the vortex tube runs through the centre of the object whereas for vortex rings that are of the size of the object, the object moves towards the centre of the ring. The position of the vortex core relative to the centre of the object is plotted in Fig. 3.3 (right). At $U = 0.58$, the 'pinned' ring solution (broken line) disappears. With increasing velocity, the ring shrinks further but still has a finite size at the critical velocity.

The solid line in Fig. 3.3 that is zero for velocities $U < 0.70$ corresponds to the laminar flow solution. A small vortex ring forms at velocities close to U_c. This point highlights the gradually nature of the transition from laminar flow to flows containing vortices. The conservation of circulation (Kelvin's theorem) requires that vortex lines are created in pairs or as rings which emerge from a point [68], or at

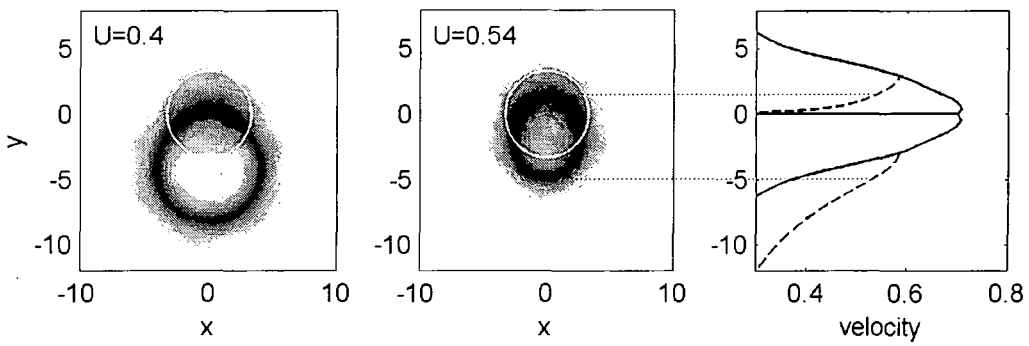

Figure 3.3: The density plots illustrate the steady transition from the pinned to the encircling ring solution. At $U = 0.4$ (left) the vortex line goes through the centre of the object. For a smaller ring (middle, $U = 0.54$), however, a location fully inside the object becomes energetically favourable. The right graph shows the position of the $\psi = 0$ lines with respect to the centre of the sphere for the different solutions: pinned ring (broken line), encircling ring (solid line) and laminar flow (joining into the encircling ring solution at $U_c = 0.71$). Apparent is the emergence of a vortex ring at the centre of the sphere in the laminar flow branch just below the critical velocity.

boundaries [57]. The laminar flow solution converges to the encircling ring solution at U_c. In this and indeed all the following plots, the two solutions appear as two parts of the same continuous graph, the transition between the laminar flow and the vortex flow is smooth.

3.3 Energy of the flow

The energy as a function of velocity for different obstacle heights is shown in Fig. 3.4. For a free ring ($V = 0$), Fig. 3.4 (a), the energy and momentum decrease with increasing velocity, reaching a minimum at $U = 0.93$, which corresponds to the cusp in the dispersion curve (see inset). For $U > 0.93$, the collapsed ring leaves a lower density, higher velocity region (see Section 2.5.3) with energy $E \sim cP$. Inserting $E = cP$ in Eq. (2.28), one finds that as v decreases, $|\phi|^2$ must also decrease, but this becomes impossible when $|\phi|^2 = 0$, so the rarefaction pulse is replaced by a vortex ring. The process of supersonic flow creating a localised sound wave which evolves into a vortex ring (or pair in 2D) appears to be central to the mechanism of vortex nucleation in dilute quantum fluids (see e.g. Fig. 4 in Ref. [68]). For $V > 0$,

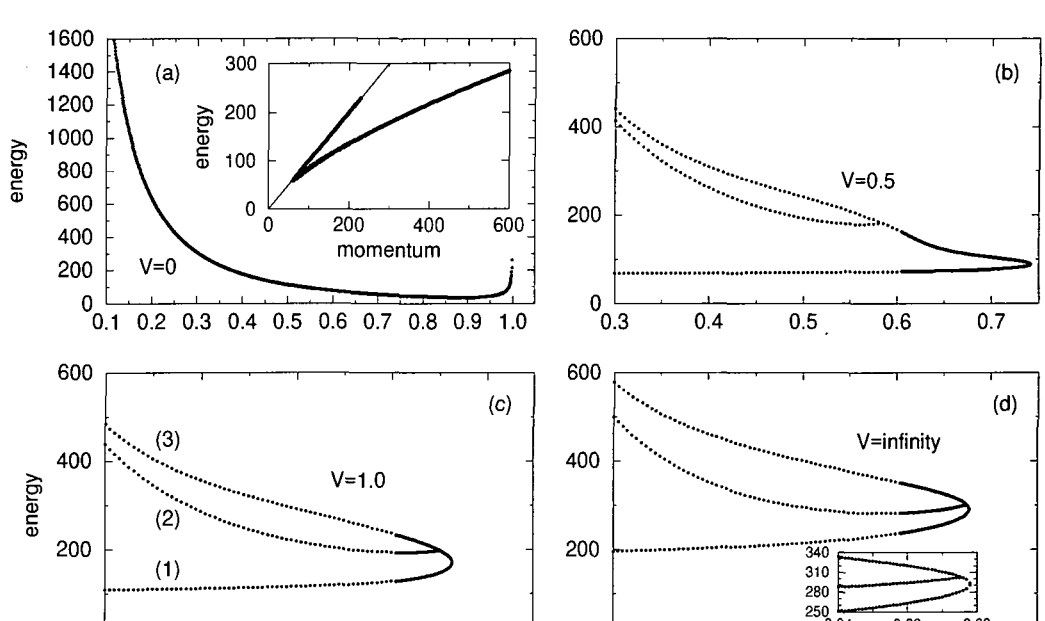

Figure 3.4: The energy of the stationary solutions of the NLSE as a function of the flow velocity. With no obstacle (a), free ring solutions are found up to the speed of sound $U = 1.0$, however, the ring collapses at $U = 0.88$ leaving a localised solitary wave with energy, $E \sim cP$ (see inset). For $V > 0$ ($R = 3.3$) (b)-(d) there are three branches: (1) laminar flow; (2) the pinned ring; and (3) the encircling ring. The encircling and pinned solutions merge below the critical velocity, see (d) inset.

Fig. 3.4 (b), the energy of the laminar flow solution (1) is no longer zero, and the ring solution bifurcates into two branches corresponding to the pinned ring (2) and the encircling ring (3). For low velocities (large radii), the energy of the encircling ring is higher than the pinned ring by an amount corresponding to the energy of the ring segment excluded by the object. Note that the pinned and encircling ring solutions always merge below the critical velocity, Fig. 3.4 (d) inset.

3.4 The critical velocity

The critical velocity for the breakdown of superfluidity is often expressed in terms of the Landau condition [56], $U_c = (\epsilon/p)_{\min}$, where ϵ and p are the energy and momentum of elementary excitations in the fluid, and U_c is the flow velocity in the

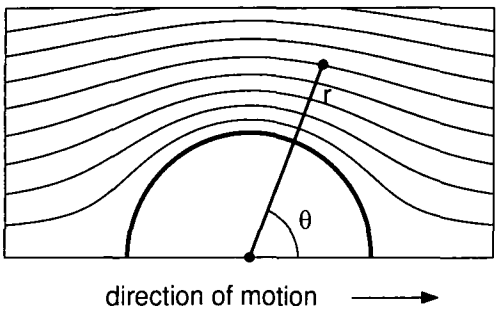

Figure 3.5: Sketch of streamlines around a sphere for an incompressible fluid, Eq. (3.2). The flow velocity at the equator of the sphere ($r = R$ and $\theta = \frac{\pi}{2}$) is enhanced by a factor of $\frac{3}{2}$. The compressibility of the quantum fluid further enhances the local velocity there because the fluid has to go faster in regions of lower density in order to satisfy the continuity equation.

fluid bulk. In the dilute Bose gas, the long wavelength elementary excitations are sound waves and the Landau criterion predicts that $U_c = c$. However, for flow past an object, the *local* velocity near the obstacle, v, can become supersonic even when the flow velocity, U, is sub-sonic. Consequently, the critical flow velocity, U_c, where laminar flow becomes unstable occurs at a fraction of the sound speed.

Fig. 3.5 sketches the streamlines of a flow past a sphere. The flow speed is highest at the equatorial plane of the sphere. To calculate the flow velocity, consider the continuity equation, $0 = \nabla(\rho\nabla S)$, where S is the phase and $v = \nabla S$ the local velocity. For an incompressible fluid ($\rho \equiv$ const) the stream function S is

$$S(r,\theta) = Ur\cos\theta + \frac{U}{2}\frac{\cos\theta\ R^3}{r^2}\ . \tag{3.2}$$

This corresponds to a laminar flow past a sphere with the correct boundary condition at infinity. As expected, the maximum flow velocity occurs at the equatorial plane,

$$v_{\rm equ} = \frac{1}{R}\left.\frac{\partial S}{\partial\theta}\right|_{r=R,\theta=\pi/2} = \frac{3}{2}U\ . \tag{3.3}$$

However, the NLSE describes a compressible fluid and the local density in regions of high velocity is reduced according to Bernoulli's equation (2.14) (neglecting the

quantum pressure),

$$1 + \frac{1}{2}U^2 = \rho(v) + \frac{1}{2}v^2 \,. \tag{3.4}$$

This leads to a further enhancement of the local velocity near the obstacle. The correction can be expressed in a series expansion involving higher order terms of the flow speed at infinity [37]:

$$v_{\rm equ} = \frac{3}{2}U + 0.313U^3 + 0.392U^5 + \dots \,. \tag{3.5}$$

In the limit of large radius, $R \to \infty$ (where one can neglect the boundary layer and hence the quantum pressure term), one can predict the critical velocity analytically using this asymptotic expansion for the speed at the equator. The solution becomes unstable when the flow velocity becomes equal to the sound speed, $v = \sqrt{\rho}$, Eq. (2.9). Combining these results (including terms up to U^{11}) gives $U_c = 0.53004$ for $R \to \infty$.

To illustrate the behaviour of the exact solutions near the critical velocity, we solve equation (3.1) in 3D for an impenetrable sphere with radius $R = 50$. The wavefunction, velocity and quantum pressure term near the object are shown in Fig. 3.6. Note that these parameters are related via the Bernoulli equation (2.14). The intersection of the velocity v and wavefunction amplitude ($|\psi|$) curves defines the position where the velocity is equal to the 'bulk' sound speed (2.9). Note that close to the object the effective sound speed is increased due to the quantum pressure term, (2.8), therefore even though the density is low the flow is not 'supersonic'. The critical velocity is reached when flow velocity exceeds the speed of sound in the bulk of the fluid, i.e., when the intersection between the velocity and wavefunction curves moves into the region where the quantum pressure term is close to zero, see Fig. 3.6 (right).

For $R = 50$ we find a critical velocity of $U_c = 0.53285$ in good agreement with the value obtained from the analysis of the laminar flow around a large sphere. The critical velocity decreases with increasing R tending asymptotically towards the $R = \infty$ value of $U_c = 0.53004$, see Fig. 3.8.

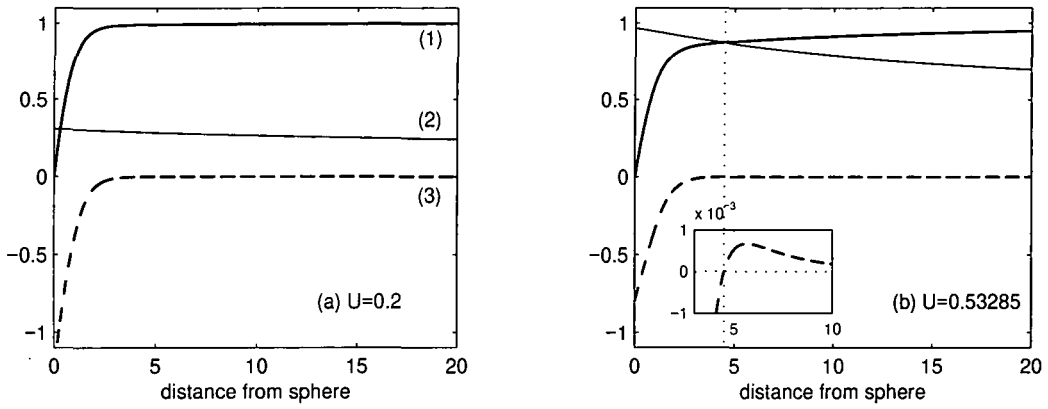

Figure 3.6: Laminar flow past a sphere with radius $R = 50$ for two flow velocities (a) $U = 0.2$ and (b) $U = 0.53285$. The three curves show, (1) the 'bulk' sound speed $c = \sqrt{n} = |\psi|$, (2) the velocity, v, and (3) the quantum pressure, $\nabla^2|\psi|/2|\psi|$, as a function of position. Note that at the critical velocity $U_c = 0.53285$ (b), the fluid velocity is equal to the sound speed where the quantum pressure is exactly zero.

3.5 Flow adjacent to a plane boundary

Two classes of solution may be distinguished for flow adjacent to a plane boundary: laminar flow and vortex loops. The loop behaves similarly to a free ring, i.e., the radius decreases with increasing velocity, and merges into the plane at a critical velocity, $U = 1$. To comment on the flow of superfluids in real systems, we consider the effect of a surface bump. In this case, the vortex loop can either encircle or pin to the bump (again the pinned loop has a lower energy). The key effect of the bump is to reduce the critical velocity, U_c, see Fig. 3.8. In the limit of large radius, $R = 10^4$, the critical velocity tends to ~ 0.53 for both surface and volume defects.

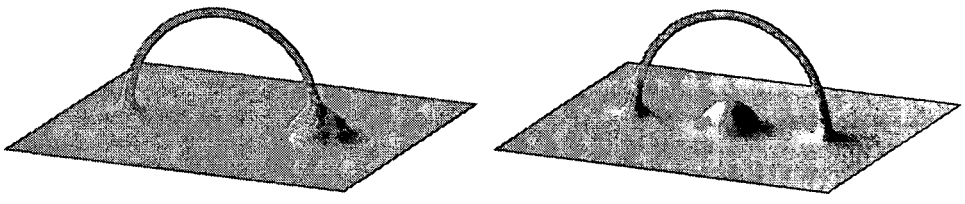

Figure 3.7: Surfaces of constant density illustrating the stationary vortex structures near a bump on a plane surface: vortex loops pinned (left) or encircling the bump (right).

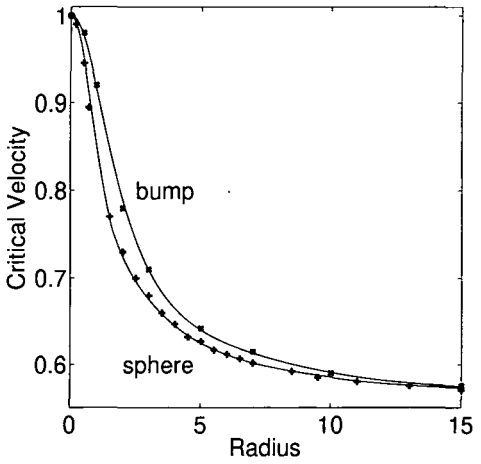

Figure 3.8: The critical velocity as a function of the defect radius, R, for an impenetrable hemisphere on a plane and sphere in the bulk. For large radii, $U_c \to 0.53$.

As U_c coincides with the appearance of drag in superfluids, one may conclude that surface roughness is a significant factor in determining the dissipation at low flow velocities.

3.6 Summary

We have investigated the flow of a quantum fluid around a moving sphere and find three classes of solutions. Ordered according to their energy, these are laminar flow, encircling ring solutions and pinned ring solutions. Both laminar flow and vortex solutions become unstable at a critical velocity. The critical velocity is equal to the speed of sound for an unbounded flow or adjacent to a wall, but decreases near an object or surface bump. As the critical velocity corresponds to a transition between normal and drag-free flow, this dependence indicates how impurities and surface roughness can produce a marked effect on the flow of superfluids.

Chapter 4

Motion of an object subject to an external force

We simulate the motion of a massive object through a dilute Bose-Einstein condensate by numerical solution of the Gross-Pitaevskii equation coupled to an equation of motion for the object. Under a constant applied force, the object accelerates up to a maximum velocity where a vortex ring is formed which slows the object down. If the applied force is less than a critical value, the object becomes trapped within the vortex core. We show that the motion follows the time-independent solutions, and use these solutions to predict the conditions required for vortex detachment.

4.1 Introduction

One of the most elementary questions that can be asked about a fluid is how will an object move through it? In quantum fluids, it is expected that the object moves without resistance at velocities, U, up to a critical value, U_c, where energy and momentum conservation allow excitations. Experiments on the motion of small objects in superfluid helium (He-II) suggest that the appearance of drag is often associated with the formation of vortices [7]. For example, ions dragged through He-II nucleate vortex rings and become trapped within the vortex core [7, 58]. However, it is not known whether the rings emerge via *quantum transition*, where the ion creates an encircling ring and subsequently attaches itself to the vortex core; or

peeling, where the ion creates a vortex loop which grows to form a pinned ring [6, 7].

Here, we study the general case of the motion of an object with finite mass moving through a dilute Bose-Einstein condensate and include the fluid back-action on the object. The time-evolution is found by solving the GP equation coupled to an equation of motion for the object. The grid contains 140 points in each dimension and we use a time step $\mathrm{d}t = 0.02$. For the object we choose a penetrable sphere with mass $M = 200$ and radius $R = 3.3$ ($V = 1.0$ for $|\boldsymbol{r}| \leq 3.3$ and 0 elsewhere). For He-II, these parameters correspond to 25 helium atoms with radius 0.6 nm (see Section 2.2), similar to the 'snowball' that surrounds a positive ion [7]. For an atomic condensate our object would correspond to a small cluster or condensate of impurity atoms in a sphere with a diameter of a few microns.

4.2 Evolution of the object velocity

An important result is that the time-dependent evolution of the object velocity is found to follow the time-independent stationary solutions, $\psi(\boldsymbol{r}', t) = \phi(\boldsymbol{r}')\mathrm{e}^{\mathrm{i}\mu t}$, of the uniform flow equation, (3.1). For an object velocity below the critical velocity, one finds three solutions, which in order of increasing energy correspond to laminar flow, a vortex ring pinned to the object, and a vortex ring encircling the object (see chapter 3). The velocity vs. momentum for these solutions for a spherical object with mass $M = 200$ and radius $R = 3.3$ are plotted as thin lines in Fig. 4.1. The laminar, encircling ring, and pinned ring branches are labelled (1), (2), and (3), respectively.

The time-dependent evolution of the object velocity due to a constant applied force, $\boldsymbol{F}$, is plotted as a bold line in Fig. 4.1. With increasing momentum, $\boldsymbol{P} = \boldsymbol{F}t$, the object velocity increases along the laminar flow branch, (1). Even though there is no drag, momentum is transferred from the object to the fluid. This momentum transfer can be described in terms of an increase in the effective or hydro-dynamical mass of the object, $m_{\mathrm{eff}} = (\partial U/\partial P)^{-1}$. The effective mass becomes infinite at the critical velocity, $U_c = 0.68$, and then negative as the object begins to slow down.

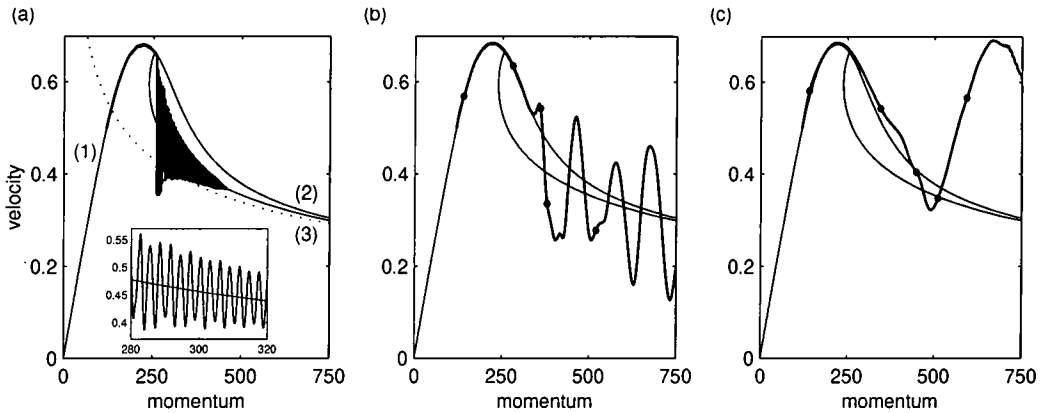

Figure 4.1: The evolution of the object velocity due to a constant applied force, $\boldsymbol{F}$. The velocity is plotted (bold line) against the total momentum $\boldsymbol{P} = \boldsymbol{F}t$ for (a) $\boldsymbol{F} = 0.05$, (b) $\boldsymbol{F} = 2$ and (c) $\boldsymbol{F} = 4$. The other curves, (1) to (3), show the time-independent solutions of the uniform flow equation, (3.1). The dotted line in (a) shows the velocity vs. momentum curve for a free vortex ring. The dots in (b) and (c) correspond to the times of the isosurface plots shown in Fig. 4.2. In each case, we begin with a laminar flow state with velocity $U = 0.5$. The applied force accelerates the object along the laminar flow solution (1) up to a peak velocity, $U_c = 0.68$, where an encircling vortex ring emerges and begins to slow the object down. In (a), an abrupt decrease in velocity occurs when the object moves into the vortex core, i.e., when the time-dependent curve switches from the encircling ring solution (2) to the pinned ring solution (3). This jump excites vibrations of the ring leading to large oscillations of the object velocity (inset). The oscillations are damped as the vortex ring grows. When the ring radius is large the object velocity tends to the velocity of a free vortex ring, indicated by the dotted line in (a). In (c), the force is sufficient to detach the object from the ring and the cycle repeats.

Close to the peak velocity, U_c, a vortex ring emerges encircling the object. The encircling vortex ring is apparent in frame 2 of Fig. 4.2 (a) which shows an isosurface of constant fluid density. The object is weakly bound in the direction of motion, therefore as the ring grows, it decelerates the object.

When the vortex core begins to separate from the object boundary, the encircling ring configuration, corresponding to the stationary solution (2), becomes unstable with respect to transverse motion, and stochastic fluctuations induce a transition to a pinned ring solution (3), where the object is bound within the vortex core as in frame 4 of Fig. 4.2 (a). In our simulations, defining the external force, $\boldsymbol{F}$, at a slight angle to the numerical grid axis is sufficient to induce the transition. On

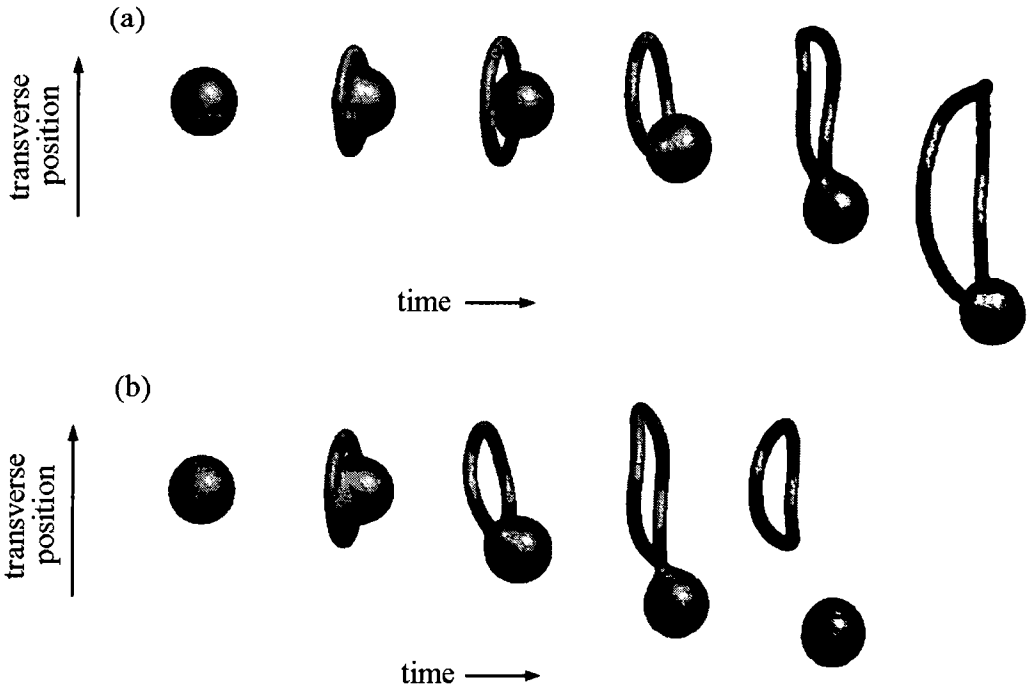

Figure 4.2: Sequence of surface contour plots of the fluid density for (a) $\boldsymbol{F} = 2$ and (b) $\boldsymbol{F} = 4$. The motion is from left to right, and the real space deflection due to the attraction of the vortex core is indicated by the transverse position. The momentum (or time) of each frame is indicated by a dot in Fig. 4.1 (b) and (c), except for the last frame in (a), where $P = 1562$. Note that after detachment, (b), the ring size remains constant and the object and ring move at different velocities.

moving into the core, the object acquires a transverse velocity thereby deflecting its trajectory (Fig. 4.2). The deflection angle is a few degrees, so this effect could be observable in experiments. Because the object slows down in the direction of the force but keeps a constant velocity in the transverse direction, the trajectory is bent (Fig. 4.3) and the deflection angle increases steadily.

If the ring detaches, a second ring forms and the object is pulled back in the opposite direction. Consequently, vortices are emitted on alternating sides of the object, similar to the vortex shedding behaviour observed in classical fluids.

The jump into the core also leads to the excitation of oscillatory modes of the vortex ring Fig. 4.2 (a). One mode of oscillation dominates [69] and the frequency is independent of the applied force. As the fluid is compressible, an accelerating object creates sound waves which damp the motion. This damping is apparent

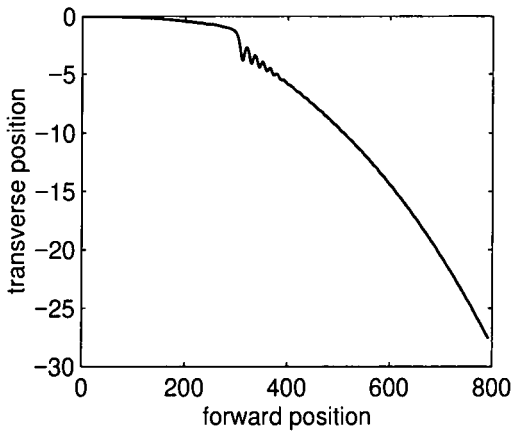

Figure 4.3: The trajectory of an ion for $M = 200$ and $F = 0.05$. On hopping into the core, the ion acquires a transverse momentum and moves with constant velocity in the transverse direction. The trajectory is bent because the system slows down in forward direction under the influence of a constant force.

in the oscillations of the object velocity in Fig. 4.1 (a) inset. If the applied force is maintained the vortex radius continues to increase and eventually the motion becomes indistinguishable from that of a free vortex ring, indicated by the dotted line in Fig. 4.1 (a).

From Fig. 4.1 (a) it follows that, excluding the ring excitations, the motion closely follows the time-independent solutions, therefore these solutions may be used to predict the motion of more complicated objects. To test whether a spherical object favours the encircling vortex ring configuration, we performed calculations on a sphere ($R = 3.3$) with a hemispherical surface bump ($R = 1.5$). The largest effect occurs when the bump lies in the equatorial plane. In this case, the critical velocity is reduced from 0.68 to 0.65, and the vortex ring emerges asymmetrically with its axis pulled towards the bump. However, the initial ring radius is still similar to the no bump case. Subsequently, the object or ring rotate such that the vortex core is pinned to the bump.

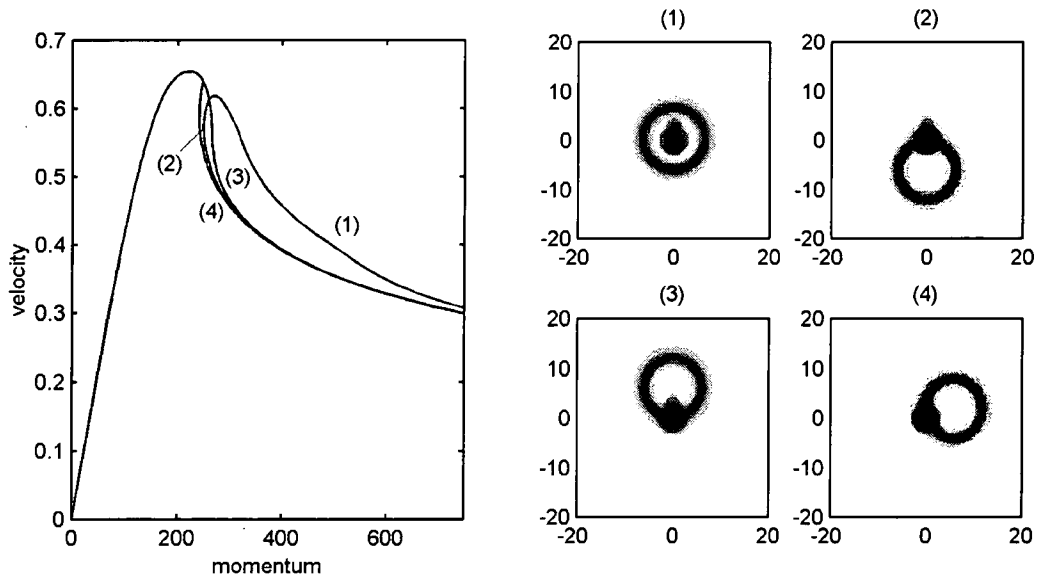

Figure 4.4: Uniform flow solutions for a sphere ($R = 3.3$) with a bump ($R = 1.5$). Left: The velocity-momentum dependence of the laminar and four vortex solutions. Right: Cross sections showing the fluid density (dark corresponds to low density around the object) for the four allowed vortex configurations: (1) Vortex ring encircling the object and bump; (2) pinned to the object; (3) encircling the bump; and (4) pinned to the bump. Note that laminar flow evolves continuously into a vortex ring encircling the bump, solution (3). Subsequently, the system evolves to the lowest energy state (4).

4.3 Oscillations in the vortex core

As is apparent in Fig. 4.3, large amplitude oscillations of the object in the transverse direction decay rapidly whereas small oscillations in the direction of motion can persist for hundreds of cycles before they decay into sound waves, see Fig. 4.1 (a). To study these oscillations, we prepare a time-independent solution for $U = 0.3$ which corresponds to a vortex ring with radius $R = 6.0$ and elongate the object with a short impulse of $P = 10$. The subsequent oscillation is shown in Fig. 4.5 (a). The amplitude is smaller than the healing length in this case. An object trapped in the core (bold line) oscillates about twice as fast as an object at the centre of the ring (thin line) due to a stronger coupling. The Fourier spectrum of the oscillation in the core are plotted for different masses, $M = 30$, $M = 60$, and $M = 200$ in Fig. 4.5 (b).

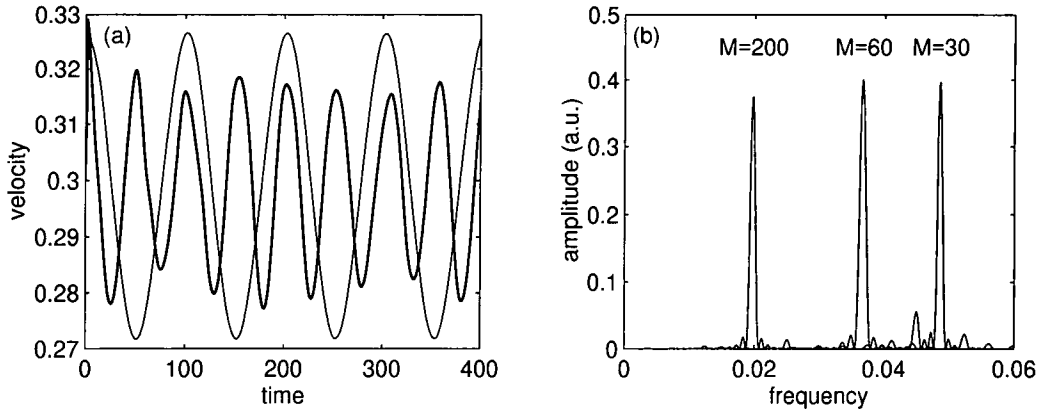

Figure 4.5: (a) Oscillations of an object of M=200 in the vortex core (bold line) and in the centre of the ring (thin line) after a small kick of momentum $P = 10$. The frequency of the oscillation in the core is higher due to a stronger binding. (b) The frequency spectra are shown for oscillations in the core for different masses

The frequency spectra are sharply peaked which suggests a simple oscillation of two linearly coupled masses with a frequency,

$$f = \frac{1}{2\pi}\sqrt{\frac{k}{\mu}}\ , \quad \text{where } \mu = \frac{Mm}{M+m}\ . \tag{4.1}$$

Here M is the mass of the object and m the mass of a part of the fluid. From the simulations, we find $m = 1400$ and a coupling constant of $k = 2.7$. Apparently, the long-lasting oscillations do not involve the entire vortex ring because its mass m_{vr} is negative (which can be seen from the negative curvature of the dispersion curve, Fig. 3.4 (a) inset).

4.4 Vortex detachment

If the applied force is sufficient, the object can detach from the vortex ring as in Fig 4.2 (b). After detachment the size of the ring remains constant, and the object can accelerate again up to the critical velocity where another ring forms. This process repeats. The beginning of this repetitive cycle is apparent in the time evolution shown in Fig. 4.1 (c). If detachment occurs, the initial encircling ring system evolves into an object and a free vortex ring which moves more slowly as in

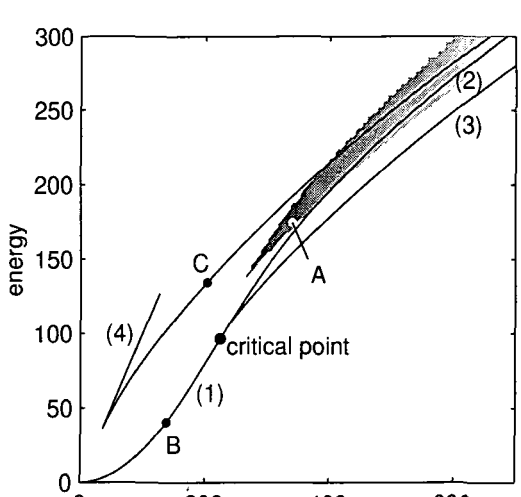

Figure 4.6: Energy and momentum conservation during vortex formation and detachment. The allowed energy and momentum states of a moving object with mass $M = 200$ (1-3) and a free vortex ring (4) determined from the time-independent solutions of the uniform flow equation, Eq. (3.1). Under a constant force, the object moves up the laminar flow branch of the dispersion curve (1) passing through the critical point where a vortex ring is formed, then continues along or just above the encircling ring branch (2). When the system reaches the shaded region, it is possible for the bound object-vortex ring (A) to decay into an object dressed by a laminar flow (B) and a free vortex ring (C). If, before detachment, the object moves into the core, the energy tends towards the pinned ring branch (3), and detachment is forbidden. The grey scale indicates the radius of the scattered vortex ring (darker is smaller). The velocity is determined by the slope of the dispersion curves.

Fig. 4.2 (b). One can regard this as a 'decay' of an encircling ring state into a free vortex ring and a new laminar flow state. In Fig. 4.6, we plot the dispersion curves for a moving object and a free vortex ring [63] obtained from the time-independent solutions of Eq. (3.1). The shaded region indicates the range of initial energies and momenta where vortex detachment may occur, i.e., for which there exists final vortex ring and laminar states which satisfy the conservation laws. In a time-dependent simulation with a constant external force, the object moves up the dispersion curve passing through the critical point where a vortex is formed and then continues along the encircling ring branch (2). When the system enters the shaded region, (point A in Fig. 4.6), energy and momentum conservation permit 'decay' into an object dressed by laminar flow (B) and a free vortex ring (C). Note that the energy at point

A is higher than the time-independent value because the object is dragged out of the plane of the ring (see Fig 4.2). If the applied force is low, the object moves into the vortex core and the system relaxes towards the lower branch of the dispersion curve (3) and detachment is forbidden.

4.5 Comparison with ions in He-II

As discussed in the Introduction, the GP equation cannot be expected to model the dynamics of He-II correctly. However, it is interesting to note that the velocity vs. momentum profile shown in Fig. 4.1 (a) is similar to the velocity vs. electric field profiles observed for ions in He-II (see e.g. [70]). If we define the healing length, $\xi = 0.18$ nm [58], we obtain a critical velocity $U_c \sim 60$ ms^{-1}, in rough agreement with experiments [70].

However, it should be noted that the situation in the He-II experiments is very different to that modelled here due to the effects of roton and impurity (^{3}He) scattering. In the experiments, the ions are accelerated up to a constant velocity where the external force is equal to the drag force due to roton/impurity scattering. This would correspond to sitting at a fixed point on the laminar flow branch of the velocity-momentum curve (labelled (1) in Fig. 4.1). From there, the transition to higher momentum (higher energy) pinned vortex state (labelled (3) in Fig. 4.1) is driven by thermal or quantum fluctuations. For ions in He-II, there is strong experimental evidence that vortex nucleation involves an energy barrier [71]. In the GP model the energy barrier corresponds to the energy required to transfer from the laminar flow (1) to the pinned ring solution (3). This energy decreases with increasing flow velocity but remains finite at the critical velocity because the pinned ring branch (3) joins the laminar-encircling ring curve (1) - (2) at an energy above the critical point, as apparent in Fig. 4.6. The size of the energy barrier depends on the object radius, mass, and penetrability. For an impenetrable sphere with radius $R = 3.3$, we find an energy barrier of approximately $8\hbar n_0 c\xi^2$. For He-II, this would correspond to ~ 3.8 K, similar to the value derived by Muirhead *et al.* using arguments based on classical fluid mechanics [8].

4.6 Summary

In summary, we have studied the motion of an object with finite mass through a dilute quantum fluid. We include the back action of the fluid on the object and show that under a constant applied force there is a continuous transition from laminar flow to an encircling ring followed by a jump where the object moves into the vortex core. This jump leads to a deflection of the object trajectory and excitations of the vortex ring. If the object has a surface bump near the equator, the encircling vortex emerges asymmetrically. If the applied force is large, the object evades capture by the ring leading to periodic vortex shedding. We show that the motion and the conditions required for vortex detachment can be predicted from the allowed time-independent states. This approach could be extended to provide useful insight into other complex problems in quantum fluid mechanics such as vortex re-connections and sound emission. Finally, we consider the applicability of the model to experiments on ions in He-II.

Chapter 5

Motion at constant velocity

Above the critical velocity, the motion of an object through a dilute Bose gas becomes dissipative. In this chapter, we study the mechanism of energy transfer from the object to the fluid for a cylinder moving at constant velocity. We observe vortex emission at supercritical velocities and, in addition, the formation of bow waves at supersonic velocities. We measure the drag force on the object and discuss the link between vortex shedding and dissipation. We compare the drag law with that of an ideal Bose gas, and show that interactions reduce the drag force. Also, we show that the effective size of the obstacle is increased due to the healing length of the fluid, and consequently the drag is non-zero even for point-like objects.

5.1 Introduction

A central issue in fluid flow concerns the origin of resistance or drag. In a viscous fluid, shear stresses induced by friction at a surface lead to *skin drag*. In a superfluid, the effects of shear stress vanish, but normal stresses induced by pressure gradients across an obstacle still produce *pressure drag*.

One could envisage an experiment to measure the pressure drag in a dilute Bose-Einstein condensate by studying the flow past an obstacle such as a far-detuned laser beam [68] or a foreign condensate species [72, 73].

A recent experiment at MIT [24] measured the heating effects of a far-detuned laser beam that was swept back and forth at constant velocity within the central region of an inhomogeneous condensate, where the density is approximately uniform. The heating rate is directly proportional to the velocity, U, of the laser beam and the drag force exerted on the fluid:

$$\frac{\mathrm{d}E}{\mathrm{d}t} = \boldsymbol{F}_{\mathrm{drag}}.\boldsymbol{U} \ . \tag{5.1}$$

At low velocities, no significant energy transfer could be measured. Above a critical velocity, $U_c \sim 0.1$ (in units of the sound speed), the drag force increases approximately linearly with velocity. However, only a small range of velocities could be studied.

In a previous numerical simulation [74], it was predicted that for a uniform system, there is a critical velocity $U_c \sim 0.4$ for the onset of drag, and that for velocities, $U > U_c$, the drag force increases linearly. However, we find that the drag force varies nearly *quadratically* with U, similar to an ideal Bose gas, i.e. a condensate of non-interacting bosons.

5.2 The linear fluid

For non-interacting bosons, the drag law may be derived analytically. We scale the units of time and space in the same way as for the weakly interacting Bose gas (Section 2.2) to be able to compare the results directly. Consider the time-independent Schrödinger equation

$$\left(\frac{1}{2}\nabla^2 + \frac{1}{2}U^2 - V\right)\psi = 0, \tag{5.2}$$

where V is a potential used to model an object. The solutions to this equation describe steady state flows of particles with momentum or velocity U and energy $U^2/2$. The particles scatter off the potential as sketched in Fig. 5.1. We assume an infinitely high barrier V and pin the wavefunction to zero at $r = R$. In cylindrical

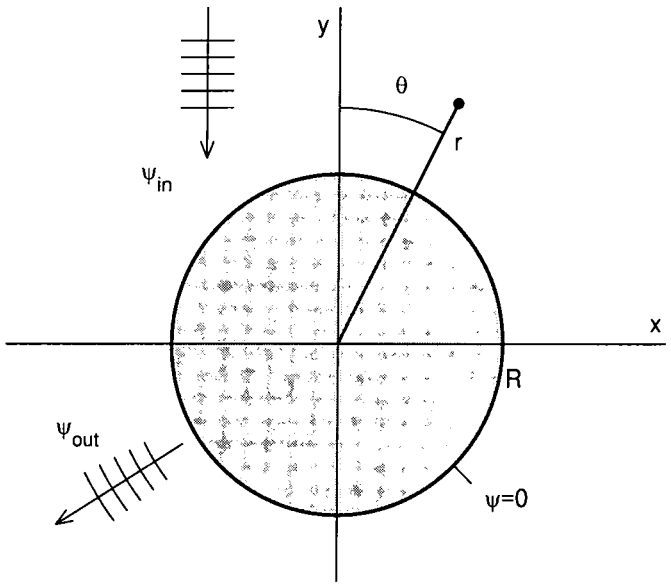

Figure 5.1: Incoming plane waves scatter off the obstacle of radius R. We use polar coordinates to solve the linear wave equation. The boundary condition at the cylinder is chosen to be $\psi = 0$ which corresponds to an infinitely high potential.

coordinates, the Nabla-operator takes the form

$$\nabla^2 \equiv \frac{\partial^2}{\partial r^2} + \frac{1}{r}\frac{\partial}{\partial r} + \frac{1}{r^2}\frac{\partial^2}{\partial \theta^2} \; . \tag{5.3}$$

We employ the following Ansatz to separate the wavefunction into a radial and an angular part

$$\psi(r,\theta) = f(r)g(\theta) \quad \text{with} \quad g(\theta) = \begin{cases} \cos m\theta, & m = 0, \pm 1, \pm 2, ... \\ \sin m\theta, & m = 0, \pm 1, \pm 2, ... \; . \end{cases} \tag{5.4}$$

In general, ψ is a linear combination of functions of the form $f(r)g(\theta)$. As apparent in Fig. 5.1, the flow solutions are symmetric about θ. Therefore, the wavefunction is only composed of the even functions $\cos m\theta$. We substitute the Ansatz (5.4) into the Schrödinger equation (5.2), to obtain

$$\left(\frac{\partial^2}{\partial r^2} + \frac{1}{r}\frac{\partial}{\partial r} - \frac{m^2}{r^2} + U^2 \right) f(r) \;=\; 0 \; , \tag{5.5}$$

$$\frac{1}{r^2}\left((Ur)^2 \frac{\partial^2}{\partial (Ur)^2} + (Ur)\frac{\partial}{\partial (Ur)} + \left((Ur)^2 - m^2 \right) \right) f(r) \;=\; 0 \; . \tag{5.6}$$

This is Bessel's differential equation. Its solutions are the so-called Hankel functions,

$$f(r) = H_m^{(1)}(Ur) = J_m(Ur) + \mathrm{i}N_m(Ur). \tag{5.7}$$

where J_m are Bessel functions and N_m the Neumann functions of order m. The Hankel functions $H_m^{(1)}$ describe a complete set of solutions to the Bessel equation. Alternatively, their complex conjugates $H_m^{(2)} \equiv \overline{H_m^{(1)}}$ may be used as a basis set for the solution. The wavefunction around the cylinder is the superposition of incoming plane waves ψ_{in} and outgoing scattered waves ψ_{out}. We write down the plane wave solutions as a series expansion involving Hankel functions:

$$\mathrm{e}^{\mathrm{i}Uy} = \mathrm{e}^{\mathrm{i}Ur\cos\theta} \tag{5.8}$$

$$= J_0(Ur) + 2\sum_{m=1}^{\infty} \mathrm{i}^m \cos(m\theta) J_m(Ur)\ . \tag{5.9}$$

Adding a general expression for the scattered wave leads to

$$\psi(r,\theta) = J_0(Ur) + 2\sum_{m=1}^{\infty} \mathrm{i}^m \cos(m\theta) J_m(Ur) + \sum_{m=1}^{\infty} A_m \cos(m\theta) H_m^{(1)}(Ur). \tag{5.10}$$

The coefficients A_m can be determined from the boundary condition at the obstacle $\psi(r = R) = 0$:

$$\begin{aligned} m = 0: &\quad A_0 = -\frac{J_0(UR)}{H_0^{(1)}(UR)} \\ m \neq 0: &\quad A_m = -\frac{2\mathrm{i}^m J_m(UR)}{H_m^{(1)}(UR)}\ . \end{aligned} \tag{5.11}$$

We have found the explicit solution to equation (5.2) and are now able to calculate the drag force analytically. In cylindrical coordinates and dropping the interaction pressure, Eq. (2.10) becomes

$$F_y = R\int_0^{2\pi} \mathrm{d}\theta\ \cos\theta \left|\frac{\partial\psi}{\partial r}\right|^2_{r=R}\ . \tag{5.12}$$

The slope of the wavefunction at the edge of the cylinder is given by

$$\left.\frac{\partial\psi}{\partial r}\right|_{r=R} = -\frac{2\mathrm{i}U}{\pi(UR)}\left(\frac{1}{H_0^{(1)}(UR)} + \sum_{m=1}^{\infty}\frac{2\mathrm{i}^m\cos m\theta}{H_m^{(1)}(UR)}\right). \tag{5.13}$$

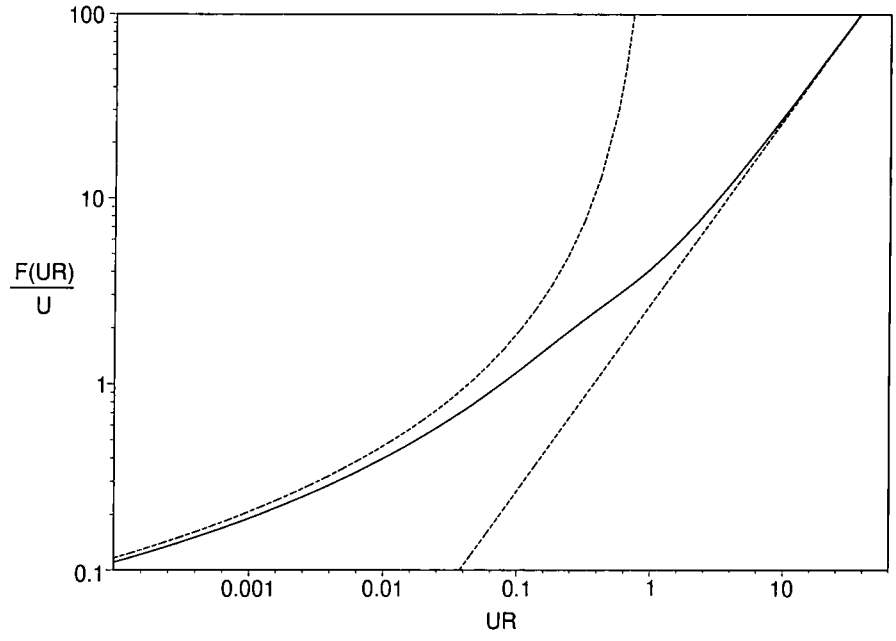

Figure 5.2: The force on a cylinder in a linear fluid calculated from Eq. (5.14) including all terms up to the 250^{th} order. The limits for short and long wavelengths, Eq. (5.15), are indicated by the dashed lines.

After some algebra we find the following expression for the drag force in flow direction

$$F_y = \frac{16U}{\pi(UR)} \sum_{m=0}^{\infty} \frac{\mathrm{Im}\left(H_m^{(1)} H_{m+1}^{(2)}\right)}{H_m^{(1)} H_m^{(2)} H_{m+1}^{(1)} H_{m+1}^{(2)}} , \tag{5.14}$$

where all Hankel functions are evaluated at UR which is a dimensionless parameter in our units. Fig. 5.2 shows the drag force on a cylinder together with its two asymptotic functions given by

$$F_y \approx \begin{cases} \dfrac{\pi^2 U}{\ln^2(UR)} & UR \ll 1 \\ \dfrac{8}{3} U^2 R & UR \gg 1 \, . \end{cases} \tag{5.15}$$

For high velocity or large object size ($UR \gg 1$), the force per unit length on an impenetrable cylinder of radius R approaches its classical limit that can be found by summing over all momenta transfered by massive particles colliding with the cylinder per unit time. As apparent in figure 5.2, the drag force exerted on the

cylinder by long wavelength particles can be many orders of magnitude larger than one would expect from the classical calculation.

In summary, a steady state solution to the linear Schrödinger equation exists for all values of U. In principle, time-dependent solutions leading to an additional drag force may be superimposed to this solution. However, due to the infinite volume of the system, they are expected to spread out or decay in the limit of long times. The drag force is non-zero for all velocities U. This can be explained by asymmetry of the solution given in (5.10) about the angle $\theta = \pi/2$ which results is a pressure difference across the object. In the following section we will see that the effects of the nonlinear term are firstly to symmetrisise the solution at small velocities and therefore cancel the pressure imbalance across the object and secondly to prohibit time-independent solutions at larger velocities.

5.3 The nonlinear fluid

For a weakly-interacting condensate the drag force must be evaluated numerically. We solve the time-dependent NLSE,

$$\mathrm{i}\partial_t\psi = -\frac{1}{2}\nabla^2\psi + V\psi + |\psi|^2\psi + \mathrm{i}\boldsymbol{U}\cdot\nabla\psi \ , \tag{5.16}$$

in two dimensions for both penetrable (V finite) and impenetrable (V infinite) cylindrical objects.

The calculations are performed using a time step, $\Delta t = 0.01$, in a box of 200×200 healing lengths, divided into 800×800 points (Appendix 2). In order to minimise the reflection of sound waves from the edges of the box, the amplitude of waves within an absorbing border of width $\Delta = 20$ is reduced each time step by the replacement $\psi \to \psi\left(1 + (|\psi| - 1)(\delta/\Delta)^3\right)$, where δ is the distance to the edge of the box.

As we have seen in the previous chapters, the solutions to (5.16) relax to time-independent flow solutions below a critical velocity which depends on the geometry of the object. This section is concerned with the dynamics *above* the critical velocity.

5.3.1 Vortex formation

The critical velocity for an infinitely long cylinder of radius $R = 3$ is approximately $U_c = 0.45$. For higher velocities there are no steady-state flow solutions. Instead, vortices are emitted almost periodically at the poles of the cylinder. The motion of the vortices is complex: the first pair may be overtaken by subsequent pairs and becomes 'trapped' for a while behind the obstacle. A snapshot of the superfluid density is shown in Fig. 5.3.

In the frame of the object, the background flow is from right to left in Fig. 5.3 and the vortex - anti-vortex pairs generate a flow which opposes the background flow. Consequently, the two vortex trails create a stationary wake behind the object.

For supersonic velocities ($U > 1$), standing waves are formed in the front of the object similar to those arising in a non-interacting Bose gas. For very large velocities ($U > 3$), steep sound waves are emitted around the object which eventually decay into vortex pairs of opposite sign. A similar behaviour has been found for grey solitons [75].

Fig. 5.4 shows a comparison between the time-averaged density distribution for a nonlinear (interacting) quantum fluid (left) and a linear (non-interacting) quantum fluid (right). One sees that the finite compressibility of the nonlinear fluid tends to suppress large density fluctuations leading to a smoothing of the standing wave

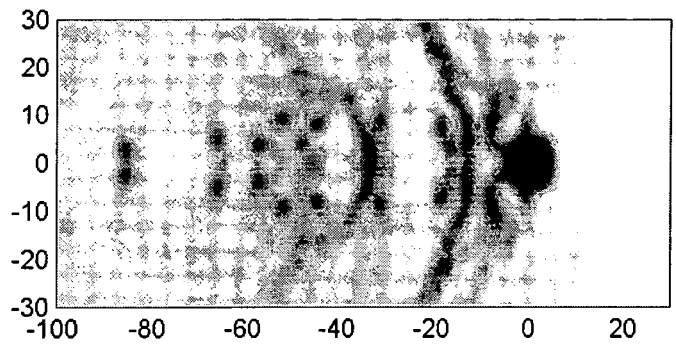

Figure 5.3: Cylinder moving through the condensate at a velocity $U = 0.6$. At the poles of the disk vortex pairs are nucleated which drop back as the obstacle moves faster than a pair of vortices separated by the diameter of the object.

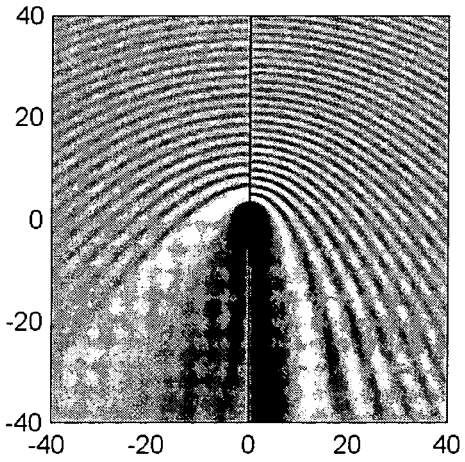

Figure 5.4: The time-averaged density distribution for $U = 2.0$ with (left) and without (right) interactions. The obstacle is an impenetrable cylinder with radius $R = 3$ centred at the origin and moving upward. The repulsive particle interactions tend to smooth density variations, thereby reducing the pressure experienced by the obstacle. For the nonlinear fluid (left), the dark line in the wake, close to the axis of symmetry, corresponds to the vortex 'street'.

in front of the obstacle. This smoothing reduces the pressure experienced by the obstacle.

The direction of the bow waves approaches the Mach angle, $\alpha = \sin^{-1}(c/U)$ [54], whereas for the non-interacting fluid Fig. 5.4 (right), $c = 0$ and $\alpha = 0$, i.e., the bow waves run adjacent to the geometric shadow behind the obstacle. In the nonlinear fluid, the 'shadow' is far less pronounced: the dark streaks in the wake, close to the axis of symmetry, correspond to sound waves emitted by interacting vortices. As a pair of vortex lines loses energy they move closer together and eventually annihilate. Far downstream, a significant fraction of the vortex energy is converted into sound. This conversion of vortex energy into sound due to vortex motion and re-connections is an important contributory process in the the decay of superfluid turbulence [76].

5.3.2 Vortex shedding frequency

The vortices separate an almost stationary wake behind the object from the background flow. The vortex shedding frequency follows from the phase-slip between

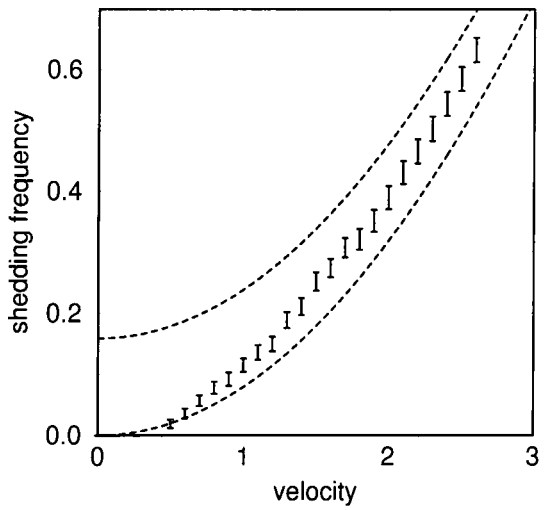

Figure 5.5: The vortex shedding frequency, f, as a function of the object velocity, U. The numerical results lie between the dashed lines, $U^2/4\pi$ and $(U^2+2)/4\pi$, which correspond to the upper and lower bounds predicted by considering the phase-slip between the main flow and a stationary wake. The error bars reflect the fluctuations in the vortex shedding frequency. At sub-critical velocity, the shedding frequency drops to zero.

the two regions. The wavefunctions for the flow and the wake may be written as $\psi = \mathrm{e}^{-\mathrm{i}(1+U^2/2)t}\mathrm{e}^{-\mathrm{i}Uy}$ and $\psi = n^{1/2}\mathrm{e}^{-\mathrm{i}nt}$, respectively, where n is the mean density behind the obstacle ($0 < n < 1$, decreasing at higher velocity). A vortex pair is emitted each time the phase difference accumulates to 2π, giving a shedding frequency, $f = (1+U^2/2-n)/2\pi$. Fig. 5.5 shows a comparison between the numerical results and the phase-slip model. As expected, the shedding frequency is close to the lower bound (corresponding to maximum wake density, $n = 1$) at low velocity, and approaches the upper bound at higher velocity as the wake density decreases.

Small fluctuations as indicated by the error bars in Fig. 5.5 in the vortex shedding frequency occur because as the vortices move downstream they interact with each other creating fluctuations in the flow pattern around the object.

5.3.3 Drag force

In principle, the instantaneous drag force can be determined by numerical integration of the stress tensor at the surface of the obstacle, Eq. (2.10). However, for penetrable objects, this procedure is complicated because the fluid-object boundary is ill-defined. For impenetrable objects, the finite grid size introduces errors in the differencing approximations. At the boundary of an impenetrable object, $\psi = 0$, however, the product $\psi^* \partial_{ij} \psi \neq 0$. If these terms are neglected in the calculation of the drag force, the numerical results reported in Ref. [74] are obtained. The numerical integration can be greatly simplified by recognising that the time-averaged drag force must be equal to the back-action on the fluid, i.e., the instantaneous force,

$$F_k(t) = -\int_{\partial\Omega} \mathrm{d}s_j \; T_{jk}(t) - \frac{\partial}{\partial t}\left[\int_{\Omega} \mathrm{d}A \; J_k(t)\right] , \tag{5.17}$$

where $\partial\Omega$ defines the outer border of a simply-connected region of fluid, Ω, encircling the object. The second term corresponds to the rate of change of the fluid momentum within Ω and averages to zero if the flow velocity remains constant. Eq. (5.17) may be used to calculate the drag for both penetrable and impenetrable objects.

Fig. 5.6 shows a plot of the instantaneous drag, $F_y(t)$, on an impenetrable cylinder with radius $R = 3$ moving with velocity $U = 1.5$. Initially, the force is dominated by transients which depend on how the flow is turned on. For an instantaneous turn-on, reflections from the obstacle produce sound waves, which are subsequently absorbed at the edges of the box. However, for longer times the time-averaged drag is independent of the initial conditions. Also, the time-averaged force is independent of the integration path $\partial\Omega$, and for barrier height $V > 1$, only weakly dependent on the penetrability of the obstacle.

The oscillatory behaviour of the instantaneous drag is produced by the periodic emission of vortex pairs, therefore the data shown in Fig. 5.6 (right) correspond to an average over many vortex emission cycles. The error bars correspond to the residual fluctuations after averaging. The drag curve for an ideal Bose gas (linear fluid), Eq. (5.14), is shown as a dashed line. One sees that the main effect of the

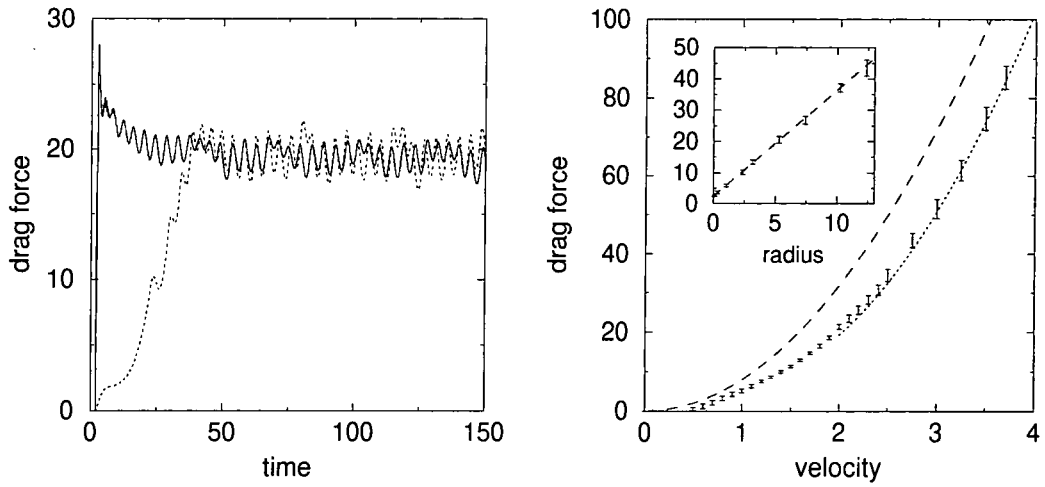

Figure 5.6: The instantaneous force (left), F_y in units of $\hbar n_0 c\xi^2$, on an obstacle placed in a nonlinear quantum flow with velocity $U = 1.5$, as a function of the time t. The two curves correspond to switching on the flow gradually (solid) or instantaneously (dashed). The oscillations are produced by the periodic emission of vortex pairs. The time-averaged drag (right) does not depend on the initial conditions. It is plotted as a function of flow velocity U, for an impenetrable cylinder with radius $R = 3$. The error bars indicate the magnitude of residual fluctuations in the time-averaged drag. The drag law for a non-interacting fluid is indicated by the dashed line. The effect of the nonlinearity is to reduce the drag which can be understood in terms of collisional screening of the object. The reduced drag predicted for a screened object is indicated by the dotted line. The force as a function of the object size for $U = 1.5$ is shown inset. Note that the drag is non-zero even for objects much smaller then the healing length.

repulsive particle interactions is to reduce the drag. For the weakly-interacting fluid, below a critical velocity, U_c, the shedding frequency (Fig. 5.5) and the drag (Fig. 5.6) fall to zero.

Above the critical velocity, a pressure drag appears with a velocity dependence similar to an ideal Bose gas. In fact, the force can be predicted accurately by a semi-classical modification of the ideal gas drag law, i. e.

$$F = \frac{8}{3} R' U'^2 \,, \tag{5.18}$$

where R' and U' are an effective object radius and flow velocity, respectively. A plot of the drag force as a function of object size, Fig. 5.6 (right, inset), indicates that the effective object size is extended by the healing length of the fluid. For $U = 1.5$

we find that $R' = R + 0.6$. An important consequence of this result is that the force does not vanish for small objects, $R \ll 1$.

The effective flow velocity, U', may be estimated by considering how the flow is modified by the collisional mean-field. Above the critical velocity, incoming waves are reflected by the obstacle producing a standing wave or bow wave [54] (see Fig. 5.4), with a density $0 < |\psi| < 2$. The resulting interaction potential $E_{\rm int} = |\psi|^2$ varies in the range from 0 to 4. In a semi-classical treatment, an oscillatory potential slows incoming particles by an amount corresponding to half the maximum barrier height above the background level, i. e. $(E_{\rm int} - 1)/2$, and therefore the effective flow velocity, U' is given by $U'^2/2 = U^2/2 - (E_{\rm int} - 1)/2$. The dotted line in Fig. 5.6 is a plot of Eq. (5.18) using values of $E_{\rm int}$ obtained from the numerical solution. This 'collisional screening' model is only accurate at high velocity, $U > 2$, where a semi-classical particle treatment is valid.

5.3.4 Vortex shedding, sound radiation, and drag

The main significance of the critical velocity is that it marks the threshold for the breakdown of superfluidity and the on-set of dissipation. The motion of objects at supercritical velocities, $U > U_{\rm c}$, results in periodic vortex shedding. The energy and momentum transfer to the fluid leads to a drag force on the object.

The contribution of vortex shedding to the total drag force can be estimated by considering the momentum transfer due to vortex emission, i. e.

$$\boldsymbol{F}_{\rm vp} = f_{\rm vp}\boldsymbol{p}_{\rm vp} \ , \tag{5.19}$$

where $f_{\rm vp}$ is the vortex shedding frequency and $\boldsymbol{p}_{\rm vp}$ is the momentum of a vortex pair as it is created in the equatorial plane. The momentum $p_{\rm vp}$ is given by $2\pi d$, where d is the separation of the vortices [63].

The comparison between the measured drag force and (5.19) shown in Fig. 5.7 suggests that for $U < c$, $(c = 1)$, vortex shedding is the dominant dissipation mechanism, whereas for $U > c$, an increasingly significant contribution arises from

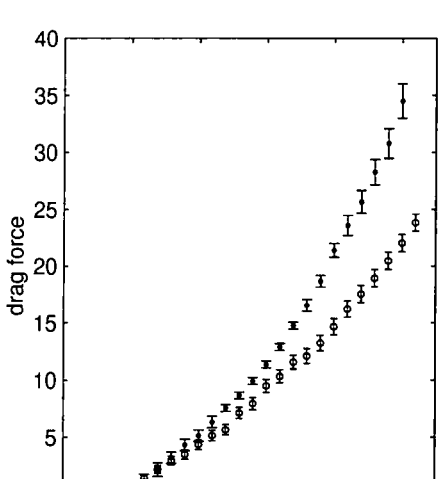

Figure 5.7: The time-averaged drag force as a function of velocity for an impenetrable cylinder with radius $R = 3$. The open circles indicates the contribution due to vortex shedding. The error bars indicate the residual fluctuations in the time-averaged drag.

sound waves. For $U > c$, the reflected matter waves create a standing wave pattern in front of the object as shown in the time-averaged density images of Fig. 5.8.

5.3.5 The critical velocity in inhomogeneous condensates

Experiments on moving laser beams in trapped atomic condensates suggest a critical velocity of $U_c \sim 0.1$ [24, 77], much lower than the homogeneous value for an cylindrical object $U_c \sim 0.4$. Vortex stretching [78] and enhanced phonon excitation at low velocity due to the spatial inhomogeneity [79] have been proposed as possible mechanisms for this reduction. Numerical simulations of trapped atomic condensates in three dimensions indicate that $U_c \sim 0.1 - 0.2$ [25] in rough agreement with experiment. It is suggested that the lower critical velocity is mainly due to formation of vortices where the object intersects lower density regions of the condensate [25].

The inhomogeneous density profile and finite size of trapped condensates means that a steady, uniform flow is difficult to achieve. The MIT experiment [24] partially overcame this problem by sweeping the object back and forth at constant velocity

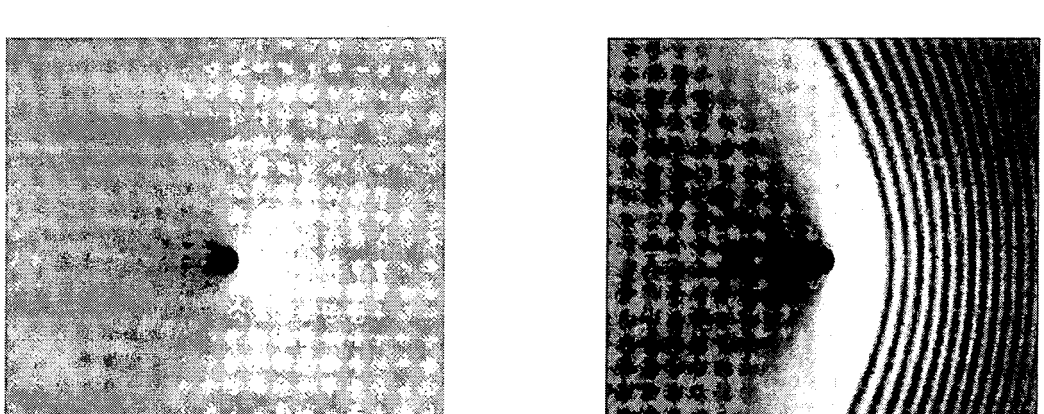

Figure 5.8: Time-averaged density of the wavefunction around a moving cylinder (radius $R = 3$) for speeds of 0.9 (left) and 1.2 (right). For supersonic flow a standing wave pattern appears in front of the object. The area shown has a dimension of 100×100 healing length whereas the computational box is 200×200 healing length.

within the central region of the condensate, where the density is approximately uniform. In this case, the object moves through its own low-density wake, and consequently the drag law is different from the uniform flow case discussed above.

5.4 Summary

The motion of an object through a dilute Bose-Einstein condensate provides an ideal system to study the fundamental problem of the onset of dissipation in superfluids. We have explained the role of vortex shedding and sound emission in energy transfer between the object and the condensate. No energy transfer is observed under the condition of uniform, steady flow at speeds below a critical velocity. Above the critical velocity vortices are emitted leading to a drag force and energy transfer to the fluid. Vortex shedding dominates the energy transfer for intermediate velocities, while sound emission becomes increasingly important for supersonic motion. The drag force is proportional to the screened energy of the flow, and to the object cross-section extended by the effect of fluid healing.

Chapter 6

The rotating Bose gas

In this chapter we study the dynamics of a superfluid under rotation. The circulation of the fluid is quantised and given by the number of vortices. In the lowest energy state vortices of equal sign are arranged in regular arrays so that the averaged density of circulation equals its classical value. The effect of a centrifugal potential on a superfluid is very similar to the effect of a magnetic field on a superconductor as will be seen in the next chapter.

6.1 Introduction

The description of the superfluid by a macroscopic wave function, $\psi = \sqrt{n}\exp(\mathrm{i}S)$, leads to a straightforward definition for the superfluid velocity, $\boldsymbol{v}$, Eq. (2.2). The circulation of the fluid is usually defined as

$$\kappa = \oint_\Gamma \boldsymbol{v} \cdot d\boldsymbol{l} = \oint_\Gamma \nabla S \cdot d\boldsymbol{l} \ . \tag{6.1}$$

Since the superfluid wavefunction is single-valued, going around a closed contour Γ must leave it unchanged, with the result that the change in the phase S can be only an integral multiple of 2π or zero. Therefore, the circulation is fully contained within the zeros of ψ and is quantised in units of 2π.

The quantised character of the superfluid circulation has been proved in many experiments with He II [6]. For equilibrium rotation, hexagonal vortex arrays have been predicted theoretically [6, 80] and have been observed in experiments [81]. Theoretical [82, 83] and experimental [22, 23] work has also been done to investigate vortex arrays and vortex nucleation in trapped atomic condensates under rotation. Here, stable vortex arrays are presented as solutions to the Gross-Pitaevskii equation for a flat-bottom potential (rotating bucket). It is known that these solutions minimise the free energy and are, therefore, stable. However, in the case of dilute Bose condensates, no dissipation occurs and it cannot be expected that dynamically produced vortices arrange in these stable patterns by relaxation. The rotation of the container is modelled by an additional centrifugal term in the NLSE:

$$\mathrm{i}\partial_t\psi = -\frac{1}{2}\nabla^2\psi + |\psi|^2\psi + V\psi + \omega L_z\psi \ , \tag{6.2}$$

where L_z is the angular momentum operator (in Cartesian coordinates $L_z = \mathrm{i}(y\partial_x - x\partial_y)$) and ω the angular frequency. The geometry of an infinitely long cylinder is modelled by adding the following potential term:

$$V(r) = \begin{cases} 0 & \text{if } r < R \ , \\ \infty & \text{if } r \geq R \ . \end{cases} \tag{6.3}$$

6.2 Vortex arrays

Hexagonal arrays of vortices are found by solving the time-independent NLSE:

$$\mu\psi = -\frac{1}{2}\nabla^2\psi + |\psi|^2\psi + V\psi + \omega L_z\psi \ . \tag{6.4}$$

Here, the chemical potential μ depends on the particular solution and has to be chosen in such a way that the average particle density is conserved and equal to 1 in dimensionless units. Eq. (6.4) is solved by Newton's method (see Appendix 1).

Fig. 6.1 (left) shows an array of $K = 56$ vortices in the rotating cylinder. The average density at the axis of rotation is suppressed due to the centrifugal force. Such arrays

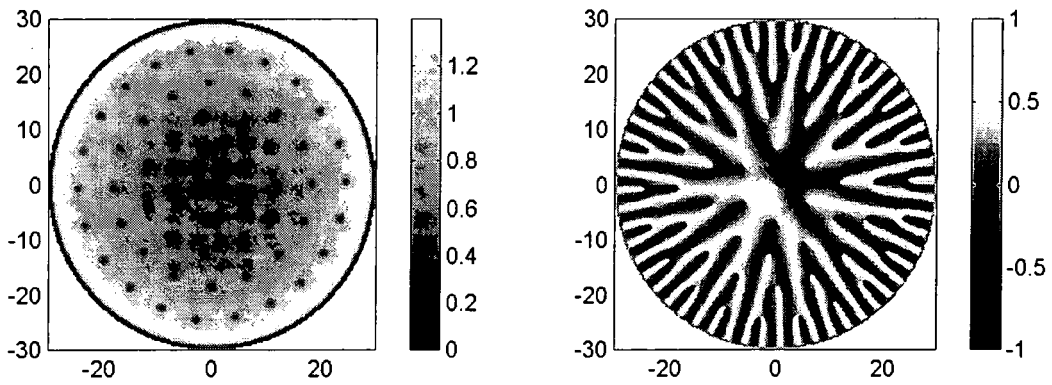

Figure 6.1: A stable array of $K = 56$ vortices in a container with $R = 29$ rotating with $\omega = 0.08$. The density of the fluid between the vortex cores clearly shows a meniscus (left). The circulation of the entire fluid in the bucket is given by the sum of the circulations of each single vortex as can be seen from the phase pattern (right).

of vortices exist only in confined geometries because each vortex is balanced by an image vortex behind the wall of the container. In an infinite system, two or more equally charged vortices repel each other [84].

Fig. 6.1 (right) shows the phase pattern of a large vortex array. The number of phase slips of 2π at the edge of the cylinder equals the number of vortices. The velocity at the edge is fairly constant with an average value of $2\pi K/2\pi R = K/R$. This velocity and the actual velocity of the container wall ωR differ by not more than a critical velocity which gives a range for the number of vortices depending on the rotation speed,

$$R(\omega R - U_c) \leq K \leq R(\omega R + U_c) \ . \tag{6.5}$$

The critical velocity U_c is close to one for a flat wall and lower for a rough surface. The equilibrium value for which the fluid velocity matches that of the wall is $K = R^2\omega$. This picture suggest that monotonic acceleration from rest always produces a state with fewer vortices than the equilibrium state and similarly deceleration produces states with more vortices. This hysteresis behaviour has been found in experiments [81].

The meniscus in the density profile along the radius of the cylinder arises as a result of the balance between the centrifugal and the interaction pressure. For a time-independent solution in the rotating frame, the mass density performs a solid body rotation in the rest frame, i.e. all mass elements revolve around the axis of the container with a velocity $\boldsymbol{\omega} \times \boldsymbol{r}$. Therefore, the circulation per unit area, which is proportional to the number of vortices per unit area, is constant. Neglecting the density holes around the vortex cores one obtains for the centrifugal force of a ring with radius r and width $\mathrm{d}r$:

$$\mathrm{d}F = 2\pi r \, \mathrm{d}r \, n(r)\omega^2 r \; , \tag{6.6}$$

where $n(\boldsymbol{r})$ is the number density of the Bose gas at a distance $\boldsymbol{r}$ from the axis of rotation. The effect of the interaction pressure is proportional to the number density,

$$\begin{aligned} \mathrm{d}F &= 2\pi r \, \mathrm{d}p = 2\pi r \, \frac{1}{2}\mathrm{d}n^2(r) \\ &= 2\pi r \, n(r)n'(r) \, \mathrm{d}r \; . \end{aligned} \tag{6.7}$$

In equilibrium, the two forces balance, $\omega^2 r = n'(r)$, giving

$$n(r) = n_0 + \frac{\omega^2 r^2}{2} = 1 - \frac{\omega^2 R^2}{4} + \frac{\omega^2 r^2}{2} \; . \tag{6.8}$$

The constant n_0 is determined by the total number of particles in the cylinder of radius R. A comparison of this parabolic profile to the actual density profile in a bucket containing 137 vortices is shown in Fig. 6.2. Apart from the density dips that correspond to seven concentric circles of vortices, the two shapes agree very well. At very large angular velocities, if $\omega > 2/R$, or expressed by the equilibrium number of vortices, if $K > 2R$, single vortices merge to form multiply charged vortices in the centre of the container, forming a 'giant vortex' state.

The chemical potential in Eq. (6.4) can be estimated with a similar approach. The solid body rotation suggests a wavefunction of the form $\psi(r, \varphi) = \sqrt{n(r)}\exp(\mathrm{i}k(r)\varphi)$. From the simulation it can be seen that the vortices lie on concentric circles. The

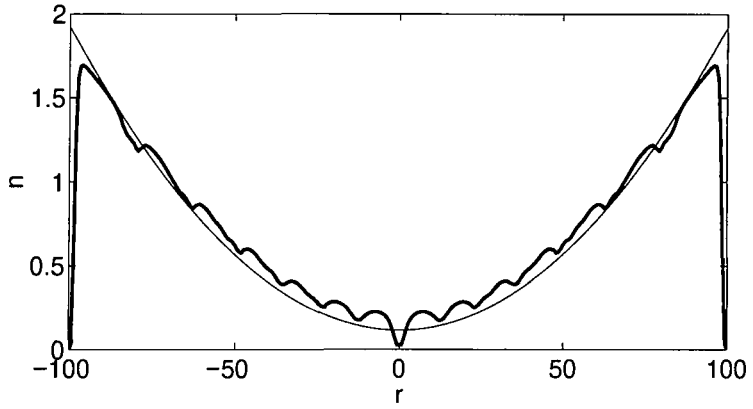

Figure 6.2: This figure shows the meniscus of the particle density in a bucket of radius $R = 99$, rotating with an angular frequency of $\omega = 0.019$. The particle density n is averaged over all angles φ. The density minima correspond to 137 vortices arranged in concentric circles. The numerical result (thick line) is in good agreement with the theoretical profile (thin line) which follows from the assumption of a constant density of vorticity.

number of vortices $k(r)$ enclosed in a circle with radius r increases in steps with increasing r. However, we assume a smooth quadratical increase of $k(r)$ that corresponds to a classical solid body rotation and should give good estimates for large numbers of vortices. With K being the total number of vortices within the radius R of the cylinder, an approximate wave function in the rotating frame is given by

$$\psi(r,\varphi) = \sqrt{n}\exp\left(\mathrm{i}\frac{Kr^2}{R^2}\varphi\right) . \tag{6.9}$$

For the chemical potential we then have

$$\mu = n(r) + \frac{Kr^2}{R^2}\left(\frac{K}{2R^2} - \omega\right) . \tag{6.10}$$

Replacing K by the equilibrium number of vortices, $R^2\omega$, and using the approximated density profile Eq. (6.8), we find

$$\mu = 1 - \frac{K^2}{4R^2} . \tag{6.11}$$

The chemical potential becomes zero when multiple charged vortices start to form and is negative for higher speeds of rotation.

6.3 Spin up of a superfluid

An array of vortices having all the same sign of rotation as the wall corresponds to the ground state of the system (except for very special cases, where the geometry plays a role, see [85]). The question is whether the vortex arrays can be formed in a rotating bucket-type of experiment, i. e. by a rotating the wall. In a time-dependent simulation, a stirrer is used to transfer angular momentum to the fluid. Below a critical angular velocity, the fluid flows in a laminar way around the stirrer and remains irrotational. At higher speeds, a number of vortices of equal sign are nucleated which increase the angular momentum of the fluid until the fluid velocity at the edge roughly matches the velocity of the stirrer. However, the vortices keep close to the edge of the container and do not arrange in stable patterns (see Fig. 6.3). Note, that one vortex of opposite sign has formed in Fig. 6.3 that has paired up with one of the other vortices and moves with constant velocity across the bucket. The state of lowest energy is not found using dynamic creation of vortices because no mechanism of dissipation is contained in the Gross-Pitaevskii equations. However, dissipation can easily be incorporated in the GP model by propagating the wavefunction in 'complex' time:

$$\mathrm{i}\partial_t\psi - D\partial_t\psi = -\frac{1}{2}\nabla^2\psi + |\psi|^2\psi + V\psi + \omega L_z\psi - \mu\phi \; . \tag{6.12}$$

The imaginary part of the time changes the character of the equation from a wave-equation to a diffusion equation. Here D denotes the diffusion constant. The system is driven towards the ground state. The chemical potential μ is subtracted to avoid a relaxation to the state $\psi \equiv 0$. For large values of D, the vortices quickly arrange into hexagonal arrays. This corresponds to the scenario observed for superconducting disks in a magnetic field (see next Chapter).

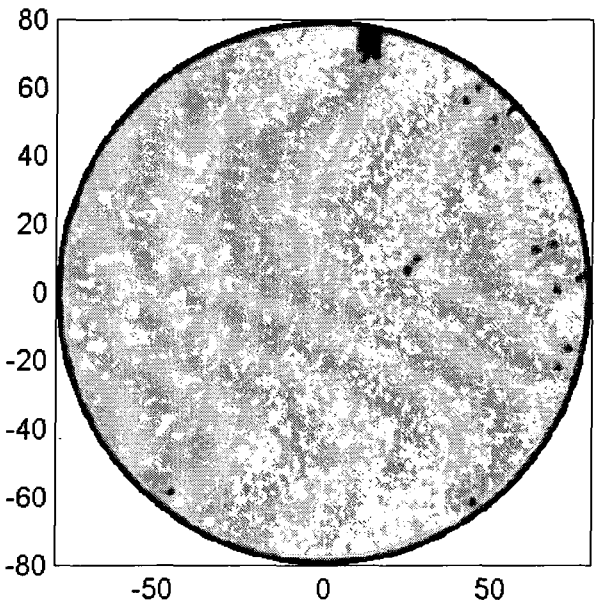

Figure 6.3: Density plot of a time-dependent solution after the stirrer has moved along the edge of the bucket with a velocity of $v = 0.5$ for $t = 1100$. The obstacle sets the fluid into rotation by nucleating single vortices of equal sign of circulation. The subsequent motion of the vortices is complex. Two equally charged vortices rotate around the centre of symmetry with a frequency of about $4/d^2$ (d is the distance between the vortices), whereas a vortex close to the edge of the container moves along the wall with a velocity of about $1/d$ (d is the distance to the wall), following the stirrer. If a vortex comes very close to the edge it reaches high velocities and eventually hits the stirrer. In the above simulation, such an event nucleated a vortex of opposite sign which combined with one of the other vortices to form a vortex pair. This pair moves with a constant velocity through the bucket.

6.4 Summary

Above a critical angular velocity, circulation enters the superfluid along vortices. Effectively the superfluid is set into rotation although the superfluid velocity is still irrotational. At equilibrium the average circulation of the fluid matches the angular rotation of the wall. The lowest energy state corresponds to a stable array of vortices all having the same sign. As we will see in the following chapter, the effect of an external magnetic field on charged particles is very similar to the effects of rotation on a neutral Bose gases.

Chapter 7

The Ginzburg-Landau Model

The time-dependent Ginzburg-Landau (TDGL) equations are obtained from the free energy functional by assuming that the order parameter relaxes towards an energy minimum with a rate proportional to the gradient of the free energy. It follows that the dynamics of a superconductor is driven by a diffusion of particles in contrast to the convection-type dynamics we have seen in superfluids. For the ground state, the order parameter obeys the same equation as the wave function of a superfluid except that it can interact with external electric and magnetic fields. In the following chapter, general properties of the solutions to the GL equations are discussed and the magnetisation of a thin disk in an external field is studied as an example.

7.1 The time-dependent Ginzburg-Landau equations

In the Ginzburg-Landau model, a superconductor is characterised by a complex order parameter ψ. The local density of superconducting electrons is represented by $|\psi|^2$. The theory postulates that close to the critical temperature, the free energy can be expanded in a series of the form

$$\begin{aligned}\mathcal{F}(\psi, \nabla\psi, \boldsymbol{A}, \nabla\times\boldsymbol{A}) &= a|\psi|^2 + \frac{1}{2}b|\psi|^4 + \frac{\hbar^2}{2m_s}\left|\left(\nabla - \mathrm{i}\frac{e_s}{\hbar}\boldsymbol{A}\right)\psi\right|^2 \\ &\quad + \frac{1}{2\mu_0}\left|\nabla\times\boldsymbol{A} - \mu_0\boldsymbol{H}\right|^2,\end{aligned} \tag{7.1}$$

where a and b are phenomenological constants which depend on external parameters such as temperature; $\boldsymbol{A}$ denotes the vector potential; $\boldsymbol{H}$ an external magnetic field; and e_s and m_s are the effective charge and the effective mass of the Cooper pairs. Below the transition temperature T_c, a becomes negative, whereas $b > 0$ for all T.

The equations of motion for the order parameter and the vector potential are the Euler-Lagrange equations of the free energy functional,

$$\frac{\hbar^2}{2m_s D}\left(\partial_t + \mathrm{i}\frac{e_s}{\hbar}\Phi\right)\psi = \frac{\hbar^2}{2m_s}\left(\nabla - \mathrm{i}\frac{e_s}{\hbar}\boldsymbol{A}\right)^2\psi + |a|\psi - b|\psi|^2\psi \tag{7.2}$$

$$\frac{1}{\mu_0}\nabla \times (\nabla \times \boldsymbol{A} - \mu_0 \boldsymbol{H}) = \boldsymbol{j}_s + \boldsymbol{j}_n \tag{7.3}$$

where

$$\boldsymbol{j}_s = \frac{\hbar e_s}{2m_s \mathrm{i}}(\psi^*\nabla\psi - \psi\nabla\psi^*) - \frac{e_s^2}{m_s}|\psi|^2\boldsymbol{A} \tag{7.4}$$

$$\boldsymbol{j}_n = \sigma(-\nabla\Phi - \partial_t \boldsymbol{A})\ . \tag{7.5}$$

D is a phenomenological diffusion constant, and Φ is the electric potential, included to retain the gauge invariance of the equations. Equation (7.3) is the Maxwell equation for the magnetic field, where the displacement current $\epsilon_0 \dot{\boldsymbol{E}}$ has been neglected [86]. The total current is given by the sum of the supercurrent, $\boldsymbol{j}_s$, and the normal current, $\boldsymbol{j}_n$, which obeys Ohm's law.

7.2 Dimensionless units

We scale length in multiples of the coherence length, $\xi = \hbar/\sqrt{2m|a|}$; time in $\tau = \xi^2/D$; the wavefunction in $\psi_0 = \sqrt{|a|/b}$; the vector potential in $A_0 = \sqrt{2}\kappa H_c \xi$; where $H_c = \mu_0|a|^2/b$; the electric potential in $\Phi_0 = (\xi/\tau)A_0$; and resistivity in units of the normal resistivity $\sigma_0 = 1/\kappa^2 D\mu_0$. The so-called Ginzburg-Landau parameter is given by $\kappa^2 = 2m^2 b/e^2\hbar^2\mu_0$. The characteristic length scale for variations of the magnetic field is $\lambda = \kappa\xi$ and $\nabla \times \boldsymbol{A}$ measures the magnetic field in units of $\sqrt{2}\kappa H_c = H_{c2}$.

Metals that undergo a superconducting phase transition, e. g. Ga, Al, Sn, Hg, Pb and Nb, have a critical temperature of $T_c < 10$ K, a critical field of H_c in the range 0.01 to 0.1 T and the coherence length ξ and London penetration depth λ range between 30 and 160 nm, and 10 and 40 nm, respectively. Commercially used metallic compounds (such as NbTi, Nb_3Sn, Nb_3Ge, V_3Ga); high-temperature superconductors (e.g. $YBa_2Cu_3O_7$); and the recently discovered MgB_2 [41] have a $T_c > 10$ K and show a much larger critical field, typically $H_{c2} > 15$ T, a shorter coherence length, $\xi = 2$ nm to $\xi = 5$ nm and a larger penetration depth, $\lambda = 100$ nm to $\lambda = 300$ nm.

In scaled units equations (7.2) and (7.3) become

$$(\partial_t + \mathrm{i}\Phi)\,\psi = (\nabla - \mathrm{i}\boldsymbol{A})^2\,\psi + \psi - |\psi|^2\psi \tag{7.6}$$

$$\kappa^2 \nabla \times \nabla \times \boldsymbol{A} = \underbrace{(\nabla S - \boldsymbol{A})|\psi|^2}_{\boldsymbol{j}_s} + \underbrace{(-\nabla\Phi - \partial_t \boldsymbol{A})}_{\boldsymbol{j}_n} + \underbrace{\kappa^2 \nabla \times \boldsymbol{H}}_{\boldsymbol{j}_{ext}}\,, \tag{7.7}$$

where S denotes the phase of ψ. The last term in equation (7.7) can be understood as an external current $\boldsymbol{j}_{ext}$ with $\nabla \boldsymbol{j}_{ext} = 0$ and can be used to model external fields or magnetic impurities in the material. In dimensionless units, the dynamics of the superconductor depends on the dimensionless Ginzburg-Landau parameter κ only.

7.3 Charged BEC

The main difference between the first Ginzburg-Landau equation, Eq. (7.6), and the NLSE for superfluids, Eq. (2.16), is the missing imaginary constant in front of the time derivative. Let us replace the time t in (7.6) by $-it$ and the electric potential by $\mathrm{i}\Phi$ to retain the general gauge invariance of the equations (see Section 7.4). The consequences of this substitution are discussed below. Eq. (7.6) becomes

$$\mathrm{i}\partial_t \psi = -(\nabla - \mathrm{i}\boldsymbol{A})^2\psi + (|\psi|^2 - 1 + \Phi)\psi\,. \tag{7.8}$$

With this replacement, we obtain an equation that is very similar to the NLSE and we can employ the Madelung transformation as discussed in Section 2.1. The

continuity equation $\dot{n}+\nabla \boldsymbol{j} = 0$ is satisfied if we define $n = |\psi|^2$ as the number density and $\boldsymbol{j} = 2(\nabla S - \boldsymbol{A})|\psi|^2$ as the current density. The local velocity is identified as $\boldsymbol{v} = 2(\nabla S - \boldsymbol{A})$. Following the same steps as in Section 2.1, Eq (7.8) becomes

$$n\partial_t \boldsymbol{v} = -\nabla p - \frac{1}{2} n \nabla \Phi - 2n\partial_t \boldsymbol{A} \ , \tag{7.9}$$

where

$$p = -n\nabla^2 \ln n + n^2 \ . \tag{7.10}$$

As in the superfluid, the dependence of the pressure p on the particle density is given by a non-local and non-linear expression. Simplifying further, one obtains

$$\partial_t \boldsymbol{v} = -\nabla w - \frac{1}{2}\nabla v^2 - 2\nabla \Phi - 2\partial_t \boldsymbol{A} \ , \tag{7.11}$$

where $w = -\nabla^2 n^{1/2}/2n^{1/2} + 2n$. With help of the relation $\frac{1}{2}\nabla v^2 = (\boldsymbol{v}\nabla)\boldsymbol{v} + \boldsymbol{v} \times \nabla \times \boldsymbol{v}$, one arrives at the Euler equation with an additional force term due to the Lorentz force:

$$\underbrace{\partial_t \boldsymbol{v} + (\boldsymbol{v}\nabla)\boldsymbol{v} = -\nabla w}_{\text{Euler fluid}} - 2\boldsymbol{v} \times \nabla \times \nabla S + \underbrace{2(\boldsymbol{E} + \boldsymbol{v} \times \boldsymbol{B})}_{\text{Lorentz force}} \ . \tag{7.12}$$

Here $E = -\nabla\Phi - \partial_t \boldsymbol{A}$, $\boldsymbol{B} = \nabla \times \boldsymbol{A}$. The term $\boldsymbol{v} \times \nabla \times \nabla S$ is zero everywhere except in the vortex core where it acts in the radial direction pushing particles away from the vortex line. Clearly, equation (7.12) describes a Bose-Einstein condensate of charged particles. This agrees with the picture that the Cooper pairs in a superconductor are condensed to form a macroscopic wavefunction just like the bosons in dilute alkali condensates.

However, the dynamics is greatly changed due to the 'imaginary time' derivative in the TDGL equations. The flow of superelectrons does not necessarily conserve energy and momentum as suggested from the above analysis. Instead the superelectrons constantly exchange energy with the lattice of the superconductor thereby

minimising the free energy. The lattice acts at a heat bath for the Cooper pairs. Therefore, the TDGL equations model a constant *temperature*[1] whereas the NLSE describes the motion of bosons under the assumption that the *energy* is conserved. As mentioned in the Introduction, the phenomenological diffusion constant in (7.2) must be chosen to be a complex number to account for the small Hall effect observed in superconductors [53]. Therefore, the dynamics of supercurrents may be understood as the motion of charged bosons in the limit of strong damping towards the ground state.

7.4 Gauge transformation

The measurable quantities $\boldsymbol{E}, \boldsymbol{B}, |\psi|^2$, and $\boldsymbol{j}$ are invariant under the transformation

$$\begin{cases} \boldsymbol{A} & \to \boldsymbol{A} + \nabla\Lambda \\ \psi & \to \psi \mathrm{e}^{\mathrm{i}\Lambda} \\ \Phi & \to \Phi - \dot{\Lambda} \, , \end{cases} \tag{7.13}$$

where Λ is an arbitrary scalar field. We choose the zero potential gauge, $\Lambda(\boldsymbol{r}, t) = \int \mathrm{d}t \Phi(\boldsymbol{r}, t)$, in other words, $\Phi(\boldsymbol{r}) \equiv 0$ at all times. For this choice, equations (7.6) and (7.7) become

$$\partial_t \psi = (\nabla - \mathrm{i}\boldsymbol{A})^2 \psi + \psi - |\psi|^2 \psi \tag{7.14}$$

$$\partial_t \boldsymbol{A} = (\nabla S - \boldsymbol{A})|\psi|^2 - \kappa^2 \nabla \times (\nabla \times \boldsymbol{A} - \boldsymbol{H}) \, . \tag{7.15}$$

In Appendix C, we suggest a fast and reliable numerical method to find an approximate solution to these equations.

7.5 The depairing current

Within the zero potential gauge it is possible to write down the TDGL equations using only measurable quantities. We write the order parameter as a product of the

[1] From the microscopic theory it can be shown that $T/T_c = 1 - \frac{1}{2}\sqrt{\frac{|a|}{b}}$ [9]

superelectron density and a phase factor, $\psi = \sqrt{n}\exp(\mathrm{i}S)$, and separate Eq. (7.14) into real and imaginary parts,

$$\partial_t\sqrt{n} = \nabla^2\sqrt{n} + \left(1 - n - j^2/n^2\right)\sqrt{n} \tag{7.16}$$

$$n\partial_t S = -\nabla \boldsymbol{E} \tag{7.17}$$

$$\partial_t \boldsymbol{A} = \boldsymbol{j} - \kappa^2\nabla\times(\boldsymbol{B} - \boldsymbol{H})\ . \tag{7.18}$$

In this gauge, $\boldsymbol{E} = -\partial_t\boldsymbol{A}$, $\boldsymbol{B} = \nabla\times\boldsymbol{A}$ and $\boldsymbol{j} = (\nabla S - \boldsymbol{A})|\psi|^2$, and clearly the time derivative of the phase must be interpreted as a local charge. From the first equation it can be seen that in equilibrium and in homogeneous regions, the superelectron density and supercurrent are related: $j^2 = n^2 - n^3$. Thus, the supercurrent reaches a maximum for $n = 2/3$, in other words $j \leq j_D = \frac{2}{3\sqrt{3}}$, where j_D is known as the *depairing current*, an upper limit for the critical current density in superconductors characteristic for every material.

7.6 Energy

The free energy in dimensionless units reads

$$\mathcal{E} = \int \mathrm{d}^3r \left\{ |(\nabla - \mathrm{i}\boldsymbol{A})\psi|^2 + \frac{1}{2}\left(1 - |\psi|^2\right)^2 + \kappa^2|\nabla\times\boldsymbol{A} - \boldsymbol{H}|^2 \right\}\ , \tag{7.19}$$

where the different contributions to the energy can be understood as the kinetic energy of particles in an external field, the condensation energy, and an energy related to the difference of the magnetic field inside and outside the superconducting sample. In analogy to Eq. (2.26), the kinetic term may be written in the form

$$|(\nabla - \mathrm{i}\boldsymbol{A})\psi|^2 = \frac{\left(\nabla|\psi|^2\right)^2}{4|\psi|^2} + (\nabla S - \boldsymbol{A})^2|\psi|^2 \tag{7.20}$$

$$= \frac{(\nabla n)^2}{4n} + \frac{1}{4}v^2 n\ , \tag{7.21}$$

where $\boldsymbol{v} = 2(\nabla S - \boldsymbol{A})$. As for superfluids, the kinetic energy is made up of a term arising from density variations and a classical term.

The possibly unexpected appearance of factors of 2 and $\frac{1}{2}$ in the local velocity and kinetic energy are due to the choice of dimensionless units, namely the coherence length which differs by a factor of $\sqrt{2}$ from the healing length defined in Section 2.2.

7.7 Boundary conditions

For a superfluid wavefunction we choose the boundary condition near objects and walls to be $\psi = 0$. This boundary condition is not appropriate for the order parameter as it wrongly predicts a zero current through wires that are thinner than a couple of coherence lengths [87]. Using the microscopic theory, de Gennes [88] has shown that for a metal-superconductor interface with no current, the following boundary condition for the order parameter must be used

$$(\nabla - \mathrm{i}\boldsymbol{A})\psi|_n = \frac{\mathrm{i}}{b}\psi \,, \tag{7.22}$$

where b is a real constant ranging from zero for a magnetic material to infinity for an insulator. In the following, we model a superconductor - vacuum interface and set the supercurrent across the boundary to zero, $(\nabla - \mathrm{i}\boldsymbol{A})\psi|_n = 0$.

7.8 GL vortices

The simplest property of a superconductor is its ability to conduct an electrical current, if it is small enough, without any resistance. In other words, the existence of persistent currents. In a superfluid, stable vortices demonstrate the presence of persistent currents. The GL equations also exhibit vortex solutions characterised by a circular flow pattern with a central core. In cylindrical coordinates, the wavefunction can be put in the form $\psi = \phi^{1/2}(r)\mathrm{e}^{\mathrm{i}m\varphi}$, where $\phi(r)$ is real-valued and m is restricted to integer numbers. The phase gradient of the order parameter combined with the vector potential determine the direction of the supercurrent. For a circular flow pattern we set $\boldsymbol{A} = (0, A_\varphi(r), 0)$. The magnetic field is then parallel to the vortex line, $\boldsymbol{B} = \left(0, 0, \frac{1}{r}\frac{\partial}{\partial r}(rA_\varphi)\right)$. Thus, the time-independent GL equations for

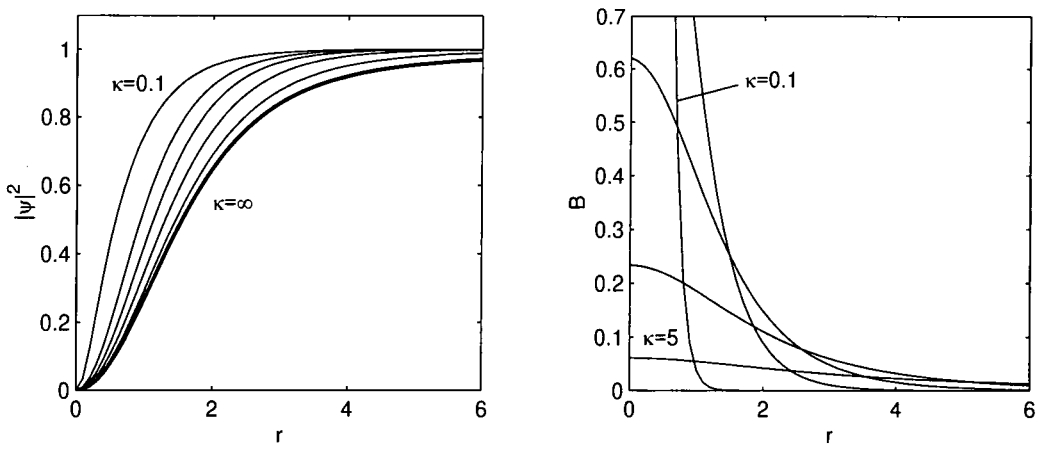

Figure 7.1: Density (left) and magnetic field (right) around a vortex line of unit circulation ($|m| = 1$) for different values of the Ginzburg-Landau parameter, $\kappa = 0.1, 0.5, 1, 2, 5, \infty$. For small κ the the magnetic flux is confined in a narrow tube, whereas for large κ the magnetic field becomes more homogeneous. Note, that in the limit $\kappa \to \infty$, the shape of the vortex core tends to the profile of a superfluid vortex (left, bold line). The magnetic flux carried by a vortex is quantised as $2\pi \int_{r=0}^{\infty} r \, \mathrm{d}r B_z(r) = 2\pi m$. The peak value of the magnetic field in the vortex core is given by $B_z(0) \approx 0.6302\kappa^{-1.444}$.

an isolated vortex line are

$$0 = \frac{1}{r}\frac{\mathrm{d}}{\mathrm{d}r}\left(r\frac{\mathrm{d}\phi}{\mathrm{d}r}\right) - \left(\frac{m}{r} - A_\varphi\right)^2 + \phi - \phi^3 \tag{7.23}$$

$$0 = \left(\frac{m}{r} - A_\varphi\right)\phi^2 + \kappa^2 \frac{\mathrm{d}}{\mathrm{d}r}\frac{1}{r}\frac{\mathrm{d}}{\mathrm{d}r}(rA_\varphi) \ . \tag{7.24}$$

The profiles of the density and magnetic field are shown in Fig. 7.1. Note, that in the limit of large κ, the solutions to the GL equation converge to the solutions of the Gross-Pitaevskii equation, i. e. the magnetic field and the vector potential tend to zero everywhere and the current density is given by r^{-1}. For finite κ, the current density drops faster which leads to a reduced centrifugal force. In effect, the vortex core is narrower for finite κ (see Fig. 7.1).

At large distances form the vortex line, the order parameter can be approximated by unity and Eq. (7.24) may be solved analytically:

$$\frac{j_{s,\varphi}}{n} = \frac{m}{r} - A_\varphi(r) = mH_m^{(1)}(r/\kappa) \ , \tag{7.25}$$

where $H_m^{(1)}$ is the Hankel function (see Section 5.2). The supercurrent $j_{s,\varphi}$ encircling the vortex line drops to zero exponentially as $r \to \infty$ and thereby faster than in a superfluid vortex. Therefore, the total flux through a circle of radius $R \ll \kappa$ is quantised as

$$2\pi \int_{r=0}^{\infty} r \, \mathrm{d}r B_z(r) = \int_{r=R} \mathrm{d}\boldsymbol{s} \cdot \boldsymbol{A}(r) = 2\pi m \; . \tag{7.26}$$

If a vortex is located near the surface of a superconductor, the magnetic flux may be less than $2\pi m$ as the integral in Eq. (7.26) does not extend to infinity.

7.9 The Meissner effect

The second fundamental property of a superconductor was discovered by Meissner and Ochselfeld in 1933 and consists of the complete exclusion of magnetic flux from the specimen for applied fields H less than a critical value H_c. More precisely, the magnetic field drops from its value at the surface of the superconductor to zero over a distance $\lambda = \kappa\xi$, called the London penetration depth. Figure 7.2 shows a one-dimensional scenario of a superconductor placed in an external H field perpendicular to the surface. Both the vector potential and the magnetic field drop to zero as $\exp(-|x|/\kappa)$.

The Meissner effect is due to surface currents that exactly cancel the external magnetic field. Figure 7.2 also shows the current density j_y which peaks just below its theoretical limit of $j_D \approx 0.385$. Note that the current along the surface is not associated with a phase gradient of the order parameter in this particular gauge.

The simplest argument for the existence of the Meissner state, i. e. $|\psi| = 1$ and $\boldsymbol{A} = 0$ in the bulk, is that, up to a critical field, it has a lower energy than the *normal state*, i. e. a zero order parameter and $\nabla \times \boldsymbol{A} = H$. According to Eq. (7.19), the energy of the Meissner state and normal state for a volume Ω is $\mathcal{E}_M = \kappa^2 H^2 \Omega$ and $\mathcal{E}_n = \frac{1}{2}\Omega$, respectively. Thus, the Meissner state becomes energetically favourable when $H < H_c = 1/\sqrt{2}\kappa$.

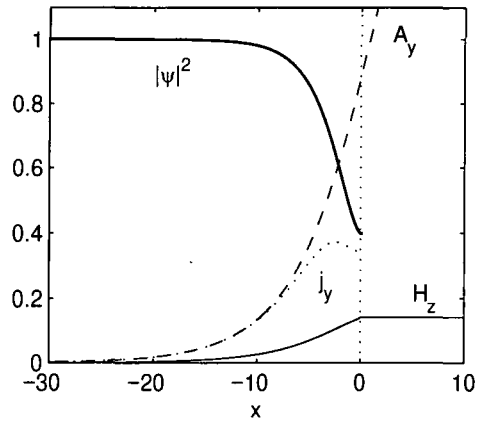

Figure 7.2: Meissner effect for a one-dimensional superconductor with $\kappa = 5$. The vector potential $\boldsymbol{A} = (0, A(x), 0)$ that is associated with a magnetic field H_z generates a persistent supercurrent j_y along the the superconductor that exactly cancels the external magnetic field. The external field is just below $H_c = 1/\sqrt{2}\kappa$.

The value of H_c is changed in small samples with more complicated geometry. Consider firstly a cylinder of radius R in an longitudinal field $\boldsymbol{H} = (0, 0, H_z)$. To minimise the energy, the superelectrons will create surface currents going around the cylinder. Unless the radius is much larger than κ, the magnetic flux at the axis of the cylinder is non-zero and the surface currents do not completely cancel the external field. For a given external field, the current density in a thin cylinder is smaller than in the 1D case discussed above and the critical current density is reached at a higher value of the external field. Therefore, the curvature of the cylinder increases H_c as shown in Figure 7.3 (left).

As a second example of how the curvature of a superconducting sample influences the Meissner critical field, consider a cylinder in a circular external field $\boldsymbol{H} = (0, H_\varphi(R)R/r, 0)$, where $H_\varphi(R)$ is the magnetic field strength at the surface of the cylinder. The induced surface currents now run parallel to the axis or the cylinder. This models a superconducting wire with a transport current $I = 2\pi R\kappa^2 H_\varphi(R)$. In this case, the total current is restricted by the depairing current, $I \leq \pi R^2 j_D$ which for the magnetic field means $H_\varphi(R) \leq Rj_D/2\kappa^2$. Fig. 7.3 (right) shows the exact behaviour of the Meissner critical field on a current carrying wire as well as the upper limit set by the depairing current (bold line at $1/R = 0.1$).

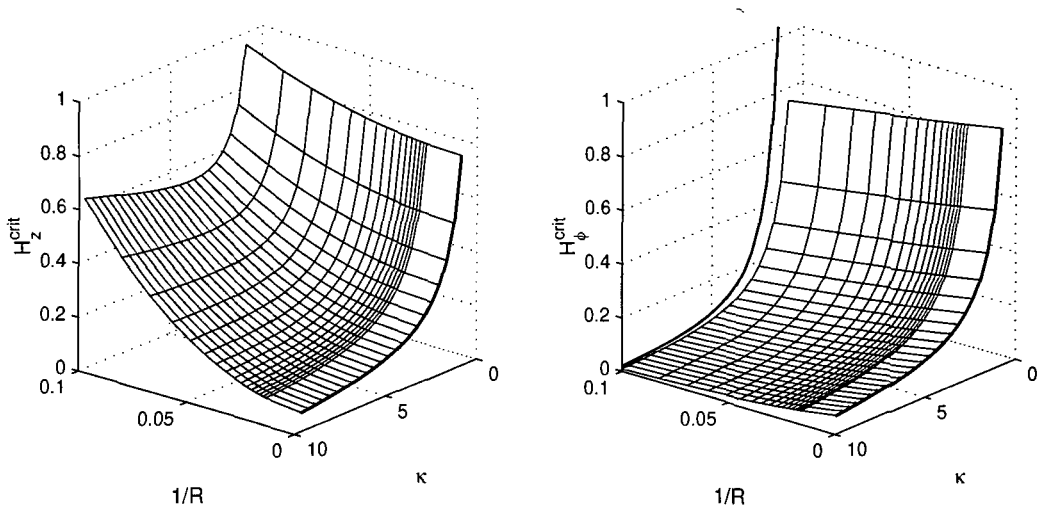

Figure 7.3: Meissner critical fields for a cylinder of radius R placed in a field parallel to the axis of the cylinder (left) and in a circular field (right). For large radius, $1/R \to 0$, the critical field converges to its 1D value $H_c = 1/\sqrt{2}\kappa$. A finite radius increases the critical field parallel to the wire but decreases the circular critical field. The bold line at $1/R = 0.1$ in the right plot indicates an upper estimate for the critical field, $H_\varphi(R) \leq Rj_D/2\kappa^2$, where j_D is the depairing current.

In summary, the critical magnetic field can always be related to a critical current density which corresponds to the critical velocity in superfluids.

7.10 The mixed state

For certain values of the Ginzburg-Landau parameter κ and the external field H, the presence of a vortex line lowers the free energy given in Eq. (7.19) compared to the Meissner state. Figure 7.4 (left) shows the energy difference, $\Delta\mathcal{E}$, between a vortex line solution and Meissner state for different values of the external field. For zero field, the currents and density variations of the vortex constitute a higher energy than the homogeneous Meissner state for all κ. However, if the magnetic field of the vortex is aligned with some non-zero external field, the last term in Eq. (7.19) is lowered locally so that $\Delta\mathcal{E}$ changes sign for a certain value of κ. The bold line shows the energy difference for $H = 1$ which becomes zero at $\kappa = 1/\sqrt{2}$. For higher fields, no Meissner state exists for $\kappa > 1/\sqrt{2}H$ and $\Delta\mathcal{E} > 0$ for all other κ.

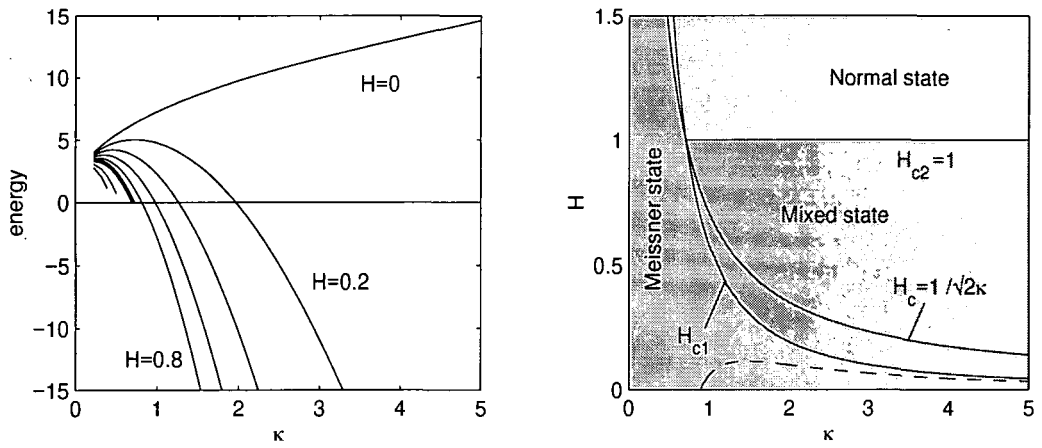

Figure 7.4: Left: Energy difference between a vortex and a homogeneous solution for external fields $H = 0, 0.2, 0.4, 0.6, 0.8, 1, 1.4, 1.8$. The vortex solution becomes energetically favourable from some value of κ that depends on the external field. The bold line shows the energy for $H = 1$ which becomes zero at $\kappa = 1/\sqrt{2}$. For higher fields, no Meissner state exists for $H > 1/\sqrt{2}\kappa$ and vortex solutions always have higher energy than the Meissner state. Right: Phase diagram showing the lowest energy state for given external field and Ginzburg-Landau parameter. The Meissner critical field $H_c = 1/\sqrt{2}\kappa$ is higher than the field H_{c1} at which the mixed state becomes energetically favourable. The first critical field may be approximated by $H_{c1} \approx (\ln\kappa + 0.116)/2\kappa^2$ (dashed line) for large κ [46]. The density of the order parameter falls to zero in the mixed state at $H_{c2} = 1$ [46].

For a given value of $\kappa > 1/\sqrt{2}$, vortices have a lower energy than the Meissner state for $H > H_{c1}$, the value at which $\Delta\mathcal{E}(\kappa, H)$ becomes negative. For those fields, the superconductor fills up with vortices and the magnetic flux runs through the sample in the form of flux tubes. This so-called mixed state is an intermediate state between the Meissner and the normal state. The average density of the order parameter goes to zero as $H \to H_{c2} = 1$ [46], which marks the transition from the mixed to the normal state. The complete phase diagram for superconductors with different κ is shown in Fig. 7.4 (right). In general, one distinguishes between *type-I* superconductors for $0 < \kappa < 1/\sqrt{2}$ and *type-II* superconductors for larger values of the Ginzburg-Landau parameter. Most metals such as Ga, Al, Sn, Hg and Pb are type-I superconductors whereas all compounds and high temperature superconductors show a mixed state.

The vortices in the mixed state are arranged in triangular arrays which were first studied by Abrikosov [89]. The density of the vortices increases with increasing external magnetic field. In equilibrium, the average internal field matches the applied external field.

7.11 Magnetisation of a disk

As an example, we study the magnetisation of a thin disk placed in a magnetic field perpendicular to its cross-section. The order parameter is expected to be homogeneous along the height of the disk and the field lines are approximately parallel so that the problem is equivalent to that of an infinitely long superconducting cylinder with a longitudinal magnetic field. This geometry has been studied experimentally [90] and theoretically [91, 92]. A type-I superconductor is found in the Meissner state up to the critical field H_c where the order parameter vanishes abruptly. Here, we present some results for a type-II superconductor ($\kappa = 5$) and a disk radius of $R = 10$.

Fig. 7.5 shows the the density of the order parameter in the Meissner state and in mixed states with up to nine vortices. The mean density decreases with increasing field and goes to zero at $H = H_{c2} = 1$. Each vortex carries a magnetic flux of 2π so that the field partially penetrates the superconductor. Outside the disk or the cylinder the field is constant. Because the value of κ is large compared to the separation of the vortices, the magnetic field inside the cylinder can be approximated to be homogeneous, $\boldsymbol{B} = (0, 0, B_z)$. In Cartesian coordinates, a possible choice for the vector potential is given by $\boldsymbol{A} = \frac{B_z}{2}(-y, x, 0)$. With this choice, the time-independent GL equation (7.14) reads,

$$0 = -\nabla^2\psi - B_z L_z\psi + \frac{B_z}{4}(x^2 + y^2)\psi - \psi + |\psi|^2\psi \ , \tag{7.27}$$

where $L_z = \mathrm{i}(y\partial_x - x\partial_y)$ is the angular momentum operator. Comparing this equation to Eq. (6.2) which described a superfluid in a rotating frame, one can see that a homogeneous magnetic field has exactly the same effect on the order parameter

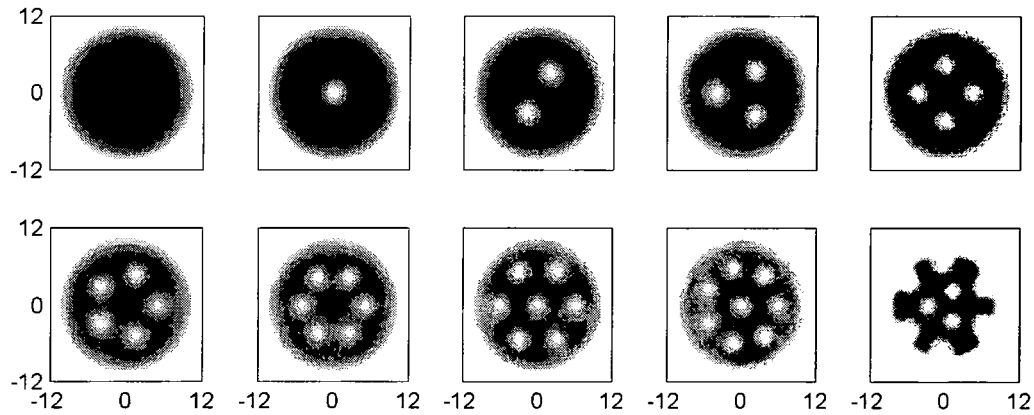

Figure 7.5: Vortex states in a small disc of radius $R = 10$ and $\kappa = 5$ at different applied fields ($H = 0 \cdots 0.6$). Shown is the density of the order parameter from white ($|\psi|^2 = 0$) to black ($|\psi|^2 = 1$) The average density decreases with increasing field and reaches zero at $H = H_{c2} = 1$ independent of the vortex configuration.

as a centrifugal potential. In a superfluid, a meniscus forms in the density profile due to rotation. However, the additional quadratic potential term, $\frac{B_z}{4}(x^2 + y^2)$, in the above equation suppresses the meniscus and leads to array of vortices in a homogeneous background density.

The states shown in Fig. 7.5 are solutions to the time-independent GL equations. The dynamics modelled by the TDGL is expected to drive the system to the lowest energy solution. We plot the energy (compared to the normal state) for each of the states shown in Fig. 7.5 versus the applied field, Fig. 7.6 (left). At very small fields, the Meissner state has lowest energy. As expected for a type-II superconductor, vortex solutions become energetically favourable for intermediate fields. First one vortex enters, then a second one and so on. With increasing field, there is a sequence of numbers of vortices characterising the lowest energy state that for our parameters is given by

$$0 \to 1 \to 2 \to 3 \to 4 \to 5 \to 6 \to 7 \to 8 \to 7 \to 6 \to 1_4 \to 1_3 \to 1_2 \to 1 \ ,$$

where a subscript m stands for vortices with a circulation $m > 1$. Multiple vortices at the axis of the disk are often called *giant vortex states.*

The right plot in Fig. 7.6 shows the magnetisation of the disk in the different states,

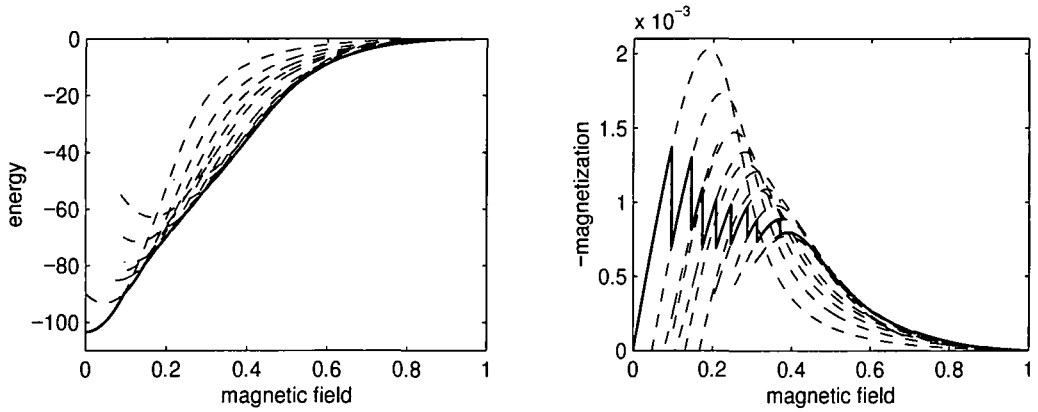

Figure 7.6: Energy of different vortex states in a small disk ($R = 10$) versus external field (left) and the according magnetisation curves (right). At small fields, the Meissner state with no vortex is the ground state and the disk shows perfect diamagnetic behaviour. If the system follows the path of lowest energy solutions (bold line), the first vortex enters at $H = 0.097$ reducing the magnetisation. Further vortices enter one by one if the field is increased further. For external fields close to the upper critical field $H_{c2} = 1$, giant vortex states, i. e. states with a multiply charged vortex at the axis of the disk become energetically favourable.

where magnetisation is simply defined as the difference of internal and external magnetic field multiplied by the (two-dimensional) volume. The bold line indicates the lowest energy solution for each field.

In practise, the magnetisation curve of a disk in a varying field may not follow the path of lowest energy states because there is an energy barrier for vortices to enter or leave the disk [93]. This nucleation barrier was first proposed by Bean and Livingston [94] and depends very strongly on the surface curvature and roughness [51].

In figure 7.7 we plot a complete cycle of the magnetisation curve for a larger disk, $R = 40$, that is found by integrating the TDGL (see Appendix 3). For this size of the disk, the jumps in the magnetisation curve are far less pronounced. Like in the rotating bucket experiment, we observe a hysteresis in the magnetisation, i. e. the disk contains fewer vortices when the external field is ramped up than in the case of a decreasing field.

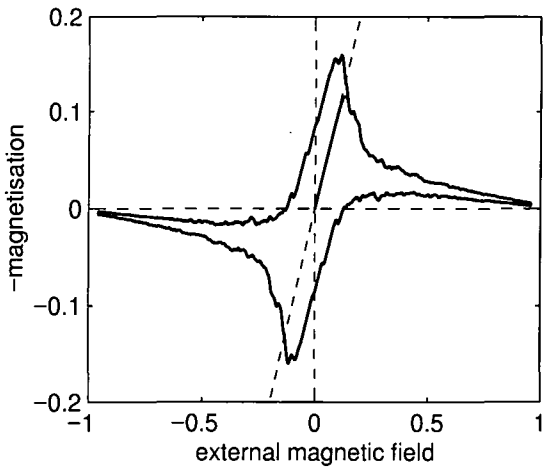

Figure 7.7: Magnetisation curve for a larger disk, $R = 40$ and $\kappa = 5$. This curve has been obtained by integrating the TDGL equations. The magnetisation does not follow the sequence of lowest energy states. For example, the magnetisation is non-zero even if the external field is zero (remanent magnetisation). Some vortices remain in the disk and their sign depends on the history of the magnetisation process. The area enclosed is determined by the energy barrier and the mobility of the vortices inside.

Starting from the Meissner state (at the origin of the plot 7.7) one still observes a perfect diamagnetic behaviour of the superconductor. The field at which vortices start overcoming the nucleation barrier and penetrating the disk is called the third critical field, H_{c3} and can be as high as $H_{c3} = 1.695 H_{c2}$ [9, 95].

7.12 Summary

We have reviewed the properties of the Ginzburg-Landau equations of superconductivity and shown the connection between the various phases that can be observed to internal and external parameters. As an example, we have presented results on the magnetisation of a mesoscopic type-II superconductor subjected to external fields.

Chapter 8

Vortex dynamics, pinning, and critical currents

The dynamics of vortices in a type-II superconductor with defects are studied by solving the time-dependent Ginzburg-Landau equations in two and three dimensions. We show that vortex flux tubes are trapped by volume defects up to a critical current density where they begin to jump between pinning sites along static flow channels. We study the dependence of the critical current on the pinning distribution and find for random distributions a maximum critical current equal to a few percent of the depairing current at a pinning density three times larger than the vortex line density. Conversely, for a regular triangular pinning array, the critical current is significantly larger when the pinning density matches the vortex line density.

8.1 Introduction

In a type-II superconductor dissipation is associated with the motion of the vortex lattice [9, 86, 96]. Consider a slab of superconductor in a transverse magnetic field, Fig. 8.1. Above H_{c1}, an Abrikosov vortex lattice forms so that, in equilibrium, the internal magnetic field matches the external field ($\boldsymbol{B} = \boldsymbol{H}$). If a current is passed through the sample in the x-direction, a gradient of the magnetic field builds up,

$$\kappa^2 \frac{\partial B_z}{\partial y} = j_x \ . \tag{8.1}$$

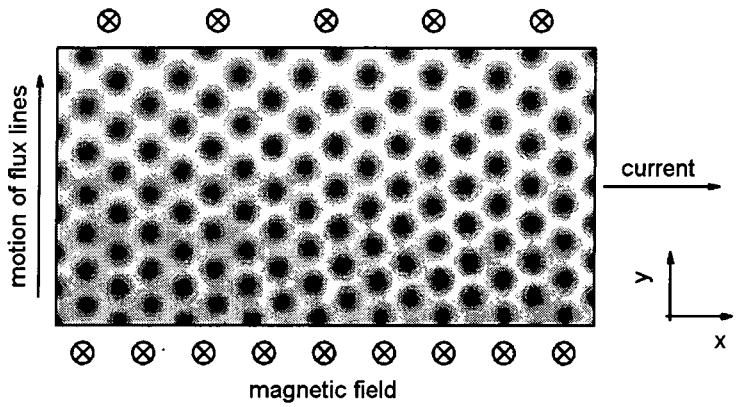

Figure 8.1: Schematic representation of a flux flow state in a slab of type-II superconductor. A sufficiently strong external magnetic field passes through the material along vortex tubes (black in this density plot). A current in the x-direction generates a field gradient in transverse direction. A Lorentz force arises that leads to motion of the flux lattice.

We have assumed a homogeneous current density. Across the slab, the magnetic field, $B_z(y)$, varies from $B_z^0 + \Delta B_z$ to B_z^0 and the total current is given by $I = \kappa^2 \Delta B_z$. The energy density associated with the magnetic field is $\kappa^2 B_z^2(y)$, Eq. (7.19). Its gradient, the Lorentz force density, Eq. (7.12) or the magnetic pressure, is given by

$$F_y = \frac{\partial}{\partial y}\left(\kappa^2 B_z^2(y)\right) = 2\kappa^2 B_z \frac{\partial B_z}{\partial y} = 2B_z j_x, \tag{8.2}$$

and pushes the vortices in the y-direction. Consequently, vortices enter the sample at the underside (see figure 8.1), move across and leave the specimen on the upper side, thereby transporting magnetic flux from a region of high magnetic field to a region of lower magnetic field. Because the energy density is given by the square of the magnetic field strength, this transport releases energy that is converted into a voltage along the slab. The local density of the vortices is proportional to the local magnetic field, $B(y)$. Therefore, the velocity of the vortices is related to the local field by $v_y(y) = \alpha / B_z(y)$. To determine the coefficient α we relate the energy released from the relaxing magnetic field to the electrical energy, $-\Delta\mathcal{E} = VI\,\Delta t$, where $V = El$ is the voltage along the slab and l its length. A magnetic flux $v_y(y)\,\Delta t\, B_z(y)$ enters and leaves the superconductor, and we can write for the total

dissipated energy per time unit Δt:

$$\Delta\mathcal{E} = l\,\Delta t\left(\frac{\alpha}{B_0}\kappa^2 B_0^2 - \frac{\alpha}{B_0+\Delta B}\kappa^2(B_0+\Delta B)^2\right) . \tag{8.3}$$

Under the simplest assumption that the electric field does not depend on y (no local charges) we find for the velocity of the vortices

$$v(y) = \frac{E}{B_z(y)} . \tag{8.4}$$

The above analysis is also correct if $|B_z^0| < |\Delta B_z|$, in other words, if $B_z(y) = 0$ on some line. In this case, vortices of opposite sign enter from both sides of the sample and annihilate where $B_z(y) = 0$.

This dissipation associated with the flux flow is reduced by the presence of defects, which pin the vortex lattice up to a critical current density where depinning occurs. In many applications, such as superconducting magnets, one is interested in optimising the vortex pinning to achieve the maximum critical current. However, the details of the depinning transition are complex, involving the non-equilibrium dynamics of an elastic lattice in a disordered medium. Theoretical studies based on molecular dynamics simulations suggest the existence of various dynamical phases of vortex motion including plastic flow, uncoupled static channels and coupled channels [10, 11, 98]. It is also possible to simulate vortex dynamics by solving the TDGL equations [51, 99, 100], where the vortex-vortex interaction is completely characterised by the GL parameter, κ. However, previous studies are restricted to two dimensions and often the limit $\kappa \to \infty$ and they do not show the effect of pinning of a sliding vortex lattice. To solve the three-dimensional equations for finite κ is computationally intensive, in part because the standart explicit integration methods require very small time-steps.

We have developed a semi-implicit method to solve the time-dependent Ginzburg-Landau equations in three dimensions (see Appendix 3). For intermediate values of κ, the semi-implicit method is two orders of magnitude faster than explicit methods, making it feasible to study dynamical vortex phases, depinning, and the de-

pendence of the critical current on the density and distribution of pinning sites. Although pinning may arise due to magnetic defects, dislocations, grain boundaries, and correlated disorder such as twin planes in high-T_c superconductors, we restrict the current study to volume defects which exclude the supercurrent.

The time-dependent Ginzburg-Landau equations (7.14) and (7.15) are discretised using a grid of $51 \times 51 \times 51$ points with a grid spacing $h = 0.4$. A current flow along x is induced by imposing a magnetic field difference, ΔB_z, between the upper ($y = 10$) and lower ($y = -10$) boundaries. The supercurrent across the boundary is set to zero. We impose periodic boundary conditions at $x = \pm 10$ and $z = \pm 10$. The average current density is given by $j = \kappa^2 \Delta B_z / d$, where d is the width of the superconductor.

8.2 Three dimensional vortex flow

A pinning array is produced by adding a potential term to equation (7.14) consisting of a random distribution of cubic potential steps with side length $a = 1.2$ and height $V_0 = 5.0$. In agreement with other studies [101], we find that the pinning strength increases with a for $a < \xi$, and saturates for $a > \xi$. A more sophisticated pinning model would be needed to account for the larger pinning forces observed for small defects [102].

Fig. 8.2 shows a sequence of images illustrating the motion of the vortex lattice through the pinning array. In frame 1, six flux tubes are visible. By comparing frames 1, 2 and 3, one sees that the central flux tubes are moving whereas the two pairs on either side are pinned. However, between frames 4 and 5 the flux tubes on the left and right jump to the next pinning site. This differential motion between neighbouring planes in the vortex lattice plays an important role in the voltage-current characteristic (see Section 8.4). After frame 6, a similar but not identical sequence recurs. For the simulations presented in Fig. 8.2, the bending of the vortex lines is increased by the choice of a larger value of κ and strong pinning. However, no entangling of vortex lines is observed. For smaller κ, the vortex lines become more

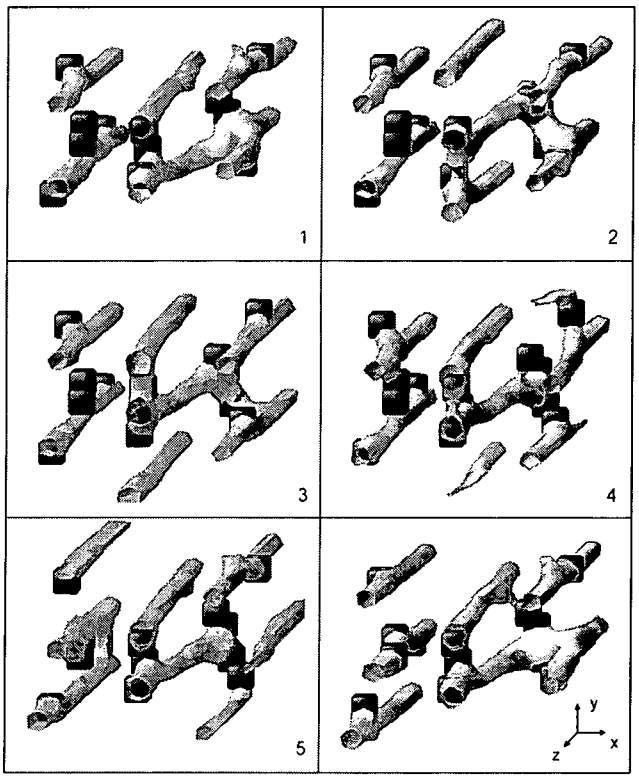

Figure 8.2: A sequence of three dimensional images showing the motion of a $\kappa = 5$ vortex lattice through a random pinning array. The axes are shown inset in frame 6. The current flows along x, the external magnetic field is along z, and the vortices move in the $-y$ direction. Each frame shows a region with dimensions $9 \times 7 \times 20$ coherence lengths containing 12 pinning sites (shown in black, not to scale). The external magnetic field and current are $B_{\text{ext}} = 0.4$ and $j = 5{\times}10^{-3}$, respectively. The grey flux tubes corresponds to surfaces of constant supercurrent density, $|\psi|^2 = 0.05$. The time interval between successive frames is 100.

rigid, and the behaviour of the three dimensional system and a two dimensional cross section are qualitatively very similar. For high-T_c superconductors, a comparison between the two and three dimensional dynamics should consider possible effects of the layered structure [103].

8.3 Two dimensional vortex flow

We use two dimensional simulations to study the effect of pinning on the voltage-current characteristic or $V - I$ curve of a superconductor with $\kappa = 3$, where three dimensional effects are suppressed. In addition, we reduce the size and strength of the pinning sites to $a = 0.8$ and $V_0 = 2.0$, respectively. In Fig. 8.3 we present contour plots illustrating the vortex lattice in two dimensions. Fig. 8.3 (a) shows the instantaneous vortex distribution for a perfect superconductor (no pinning). The vortex density is proportional to the magnetic field which decreases linearly from the bottom to the top. The vortices move upwards with a speed $v = E/B$, where B is the local magnetic field and the electric field, E, is constant throughout the sample. Consequently, the vortex flow obeys a Bernoulli-like equation where the flow is faster in regions of lower density (lower magnetic field) and the dissipation can be thought of as a relaxation of the magnetic flux lattice.

Adding defects transforms the triangular lattice into an irregular vortex glass, see Fig. 8.3 (b). For low driving fields, the vortex glass is frozen. As the current is increased, individual vortices begin to jump between pinning sites. As in the three dimensional simulations, Fig. 8.2, this motion begins along channels. The existence of static channels confirms the results of molecular dynamics simulations [10, 11]. In the Ginzburg-Landau model channels can merge or divide at intermediate drive currents, as shown in Fig. 8.3 (c). At larger currents, all the vortices are moving but the channels are still evident, Fig. 8.3 (d).

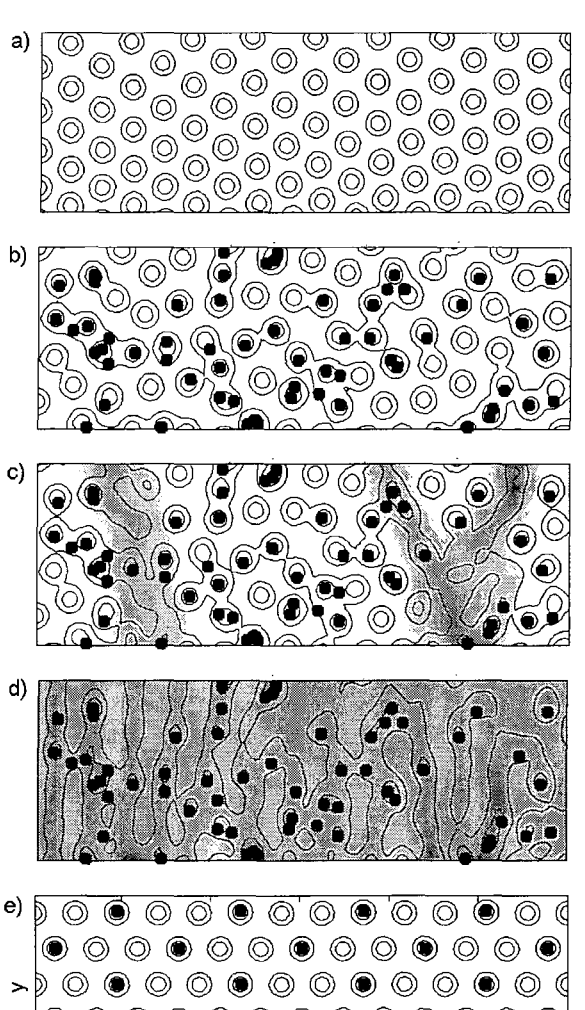

Figure 8.3: Contour plots of the supercurrent density for a section of a superconductor with dimensions 60×20 coherence lengths, and $\kappa = 3$, subject to an external magnetic field in the z direction, $B_{\text{ext}} = 0.4$. The current flows in the x direction and the vortices move in the y direction. (a) For a current $j = 0.06$ and no pinning, the vortices form a triangular lattice with lattice spacing proportional to the local magnetic field. (b) The addition of pinning (density $0.056\ \xi^{-2}$) creates a vortex glass, which at low currents, $j = 0.004$, is pinned. (c) At intermediate currents, $j = 0.005$, vortex motion begins along channels, indicated by the grey scale image of the local electric field, superimposed on a time-averaged contour plot of the supercurrent density. (d) At larger currents, $j = 0.011$, all the vortices are moving and the electric field is non-zero everywhere, however, the channels, where vortex motion mainly occurs, are still visible. (e) A regular array of volume defects pins the vortex lattice more effectively. Here, the density of vortices is three times the density of pinning sites and $j = 0.005$.

8.4 V-I curve

The on-set of vortex motion coincides with the on-set of dissipation or breakdown of superconductivity. In Fig. 8.4 we plot the $V - I$ curve for a two-dimensional thin film for different defect densities. The voltage is measured by decreasing the current at a very slow rate of $\partial_t j = -1.2 \times 10^{-7}$, and the $V - I$ curves is obtained from a 200 point moving average. As our sample size is relatively small, surface effects tend to dominate. The critical current due to the Bean-Livingston barrier for vortices entering and leaving the calculation region [51] is the same order of magnitude as the pinning effect. In order to study pinning only we remove the surface effects by adding a boundary layer of width 9 ξ on either side of a calculation region with width 30 ξ. Within the boundary layer, a linear ramp potential reduces the supercurrent density gradually to zero. The current density and the voltage are measured within the calculation region ($|y| \leq 15$) only.

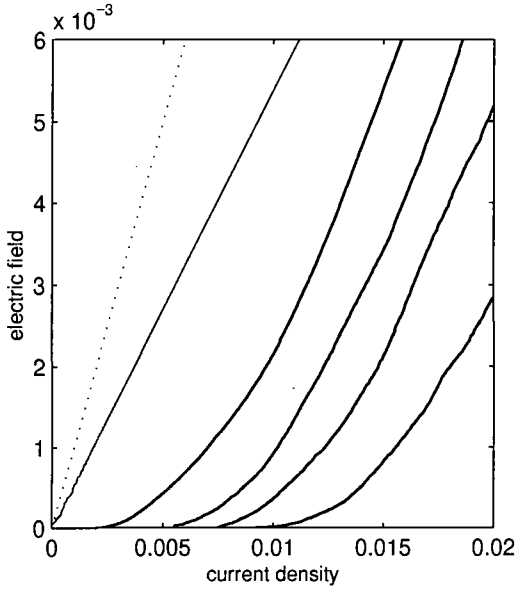

Figure 8.4: The $V - I$ curves for a two dimensional section of superconductor with pinning densities (from the right) 0.14, 0.28, 0.39, and 0.56 ξ^{-2} (at these relatively high densities, the critical current decreases with increasing pinning density). The thin black line corresponds to the $V - I$ curve without pinning, and the dotted line shows the normal resistance, $E = j$. Note that at large currents the slope of the $V - I$ curves is similar to the normal resistance curve.

The shape of the $V - I$ curve is dependent on the details of the vortex dynamics. The characteristic 'curved foot' can be explained by the combination of an increase in the number of vortex flow channels and increased flow along each active channel, as illustrated in Fig. 8.3 (c) and (d). The $V - I$ curve becomes linear when all the vortices start to move. The ratio between the $V - I$ curves and the normal resistance (the dotted line in Fig. 8.4) gives the dimensionless resistivity, which measures the fraction of current carried by normal electrons.

8.5 Critical current density

As the current is decreased the voltage becomes zero, i.e., all the vortices become pinned, at some finite current which we define as the critical current density, j_c. In the absence of finite temperature induced fluctuations or vortex creep, the value of j_c is well defined. However the critical current is sensitive to the exact distribution of pinning sites, therefore we average over six random distributions with the same density. Fig. 8.5 shows a plot of the average value of j_c against pinning density. The maximum critical current density is about 2 % of the depairing current, j_D. For comparison, the optimum critical current density of Nb-Ti alloy is $\sim$ 3 % of j_D. The maximum value of j_c occurs at a pinning density about three times larger than the vortex line density (indicated by the dotted line in Fig. 8.5).

The dependence of the critical current on the defect density fits reasonably well to a function of the form $Ax\exp(-Bx)$. The linear increase at low pinning density follows from the linear dependence of the critical current on the pinning force. However, at large pinning densities the effect of supercurrent depletion by defects leads to the exponential decrease. The shape of the curve and the relatively high optimum pinning density also agree qualitatively with experimental results on silver doped high-T_c superconductors [104].

For certain random distributions one finds persistence static channels which can dramatically reduce the critical current. This is illustrated in Fig. 8.5 (inset), where the curve with lower dissipation at large currents has a much lower critical current.

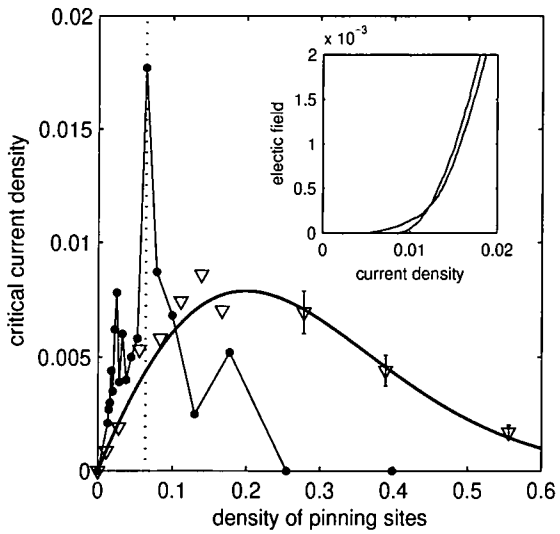

Figure 8.5: The critical current density as a function of the defect density (in units of ξ^{-2}) for both random distributions ($\bigtriangledown$) and regular triangular arrays ($\bullet$). The data points are determined from an average of six random distributions. The error bars (shown for the high density distribution only) indicate the standard deviation. An example illustrating the effect of the distribution on the $V - I$ curves is shown in the inset. The bold curve is a fit using the function $Ax\exp(-Bx)$, where A and B are fit parameters. The critical current density for a regular triangular array is a maximum when the pinning density is equal to vortex line density (indicated by the dotted line).

One approach to increase the critical current is to introduce a regular pinning array by nanostructuring [105, 106, 107]. In Fig. 8.5 we show that a regular triangular array increases the critical currents by more than a factor of two, however, the optimum pinning density is sharply peaked around the vortex line density. Consequently, the enhancement is only obtained within a narrow range of the external magnetic field. This agrees with experimental studies where a sharp enhancement peak is obtained at matching magnetic field values [107]. There are two additional critical current peaks, one at one third the vortex line density where every third vortex is trapped (see Fig. 8.3 (e)), and one at half the vortex line density, which is weaker because the matching only occurs on alternate planes. For small pinning sites ($a = 0.8$ compared to the vortex cores size of 2) the maximum critical current is about 5 % of the depairing current, j_D. For $a = 2$ we obtain $j_c = 0.074 j_D$, which suggests that other pinning mechanisms may be needed to obtain $j_c \sim j_D$.

8.6 Summary

We have studied vortex dynamics and pinning in a three dimensional superconductor by solving the time-dependent Ginzburg-Landau equations. We find that above a critical current density vortex flux tubes jump between pinning sites following specific channels. The main features of the dynamics are reproduced by two dimensional simulations. We study the effect of pinning on the voltage-current characteristic of the superconductor, and show that the breakdown of superconductivity is associated with the appearance of channelled vortex flow. The characteristic curved foot in the $V - I$ curve arises due to the combination of the formation of more channels and faster vortex flow along each channel. For a random pinning array we find a maximum critical current equal to 2 % of the depairing current occurring at a pinning density of about three times the vortex line density. Finally, we study the critical currents produced by vortex matching pinning arrays. The results suggest that time-dependent Ginzburg-Landau simulations are ideally suited to provide quantitative predictions of critical currents in type-II superconductors.

Conclusion

In this thesis we have studied the dynamical properties of quantum fluids by numerically solving nonlinear equations of motion.

The Gross-Pitaevskii equation, which is a form of the non-linear Schrödinger equation, describes a gas of weakly interacting bosons under the assumption that energy is conserved. The dilute Bose gas is an Euler fluid that differs from a classical fluid only by the restriction to quantised vorticity and a non-linear and non-local dependence of the pressure on the particle density. The excitation spectrum has a finite slope in the limit of long wavelength for repulsive inter-particle interactions. This fact, and the lack of a viscosity term, are the essential ingredients to superfluidity. According to the Landau criterion, the system energy cannot be lowered by creating an elementary excitation when the flow velocity is smaller then the speed of sound. We have studied stable vortex and vortex ring solutions in the vicinity of a moving object.

If the object is subject to a small external force, it accelerates up to the critical velocity where a vortex ring forms that slows the object down. We observe a smooth transition from laminar flow to a state where a vortex ring encircles the object. A small perturbation drives the object towards the vortex core where it becomes trapped. The hopping of the object into the core excites oscillations that decay rapidly. Apart from the transition between the encircling ring and the pinned ring state, the dynamics closely follows a sequence of time-independent states which indicates that the entire energy transfered to the fluid is stored in the vortex ring and that the process is reversible. Above a critical force, a succession of vortex

rings may detach from the object. We consider the vortex ring as an elementary excitation of the fluid and extend the Landau criterion to objects with finite mass. At very large forces, when the object velocity exceeds the speed of sound, energy is also transfered into sound waves and the drag force on the object approaches its classical limit.

Our simulations of objects moving through a dilute Bose gas agree surprisingly well with experimental results on ions in superfluid helium. In particular, the observations that the motion of ions is governed by the nucleated vortex ring and that the energy transferred to the system is fully contained in the ring suggest that the Gross-Pitaevskii model does not miss any essential physics as long as only hydro-dynamical properties of helium are probed. The situation becomes more complicated if rotons, normal fluid or ^{3}He are present in He-II. Extensions to the GP model that include a more detailed description of the inter-particle interactions and finite temperature effects are discussed in the Introduction and may be able to explain experimental results that indicate a stochastic tunnelling during vortex formation. The description of a quantum fluid as a macroscopic wavefunction is certainly superior to previously used semi-classical models in which quantum effects such as tunnelling and the quantisation of circulation were introduced in an ad-hoc manner. In summary, the GP model provides a relatively simple and accurate method for modelling dilute Bose gases and gives new qualitative insight into the more complex dynamics of superfluid helium.

The time-dependent Ginzburg-Landau equations describe a charged Bose gas under the assumption that the temperature is held constant. We have developed a fast algorithm for solving the TDGL equations by recognising that the time evolution is dominated by a diffusion of the order parameter and vector potential.

We have studied the flow of an electrical current through a superconductor placed in an external magnetic field transverse to the current and observed vortex motion due to the Lorentz force in a clean superconductor. This flux flow can be suppressed up to a critical current density by introducing a number of randomly distributed volume defects in the sample. We have measured the voltage along the superconducting

sample that is associated with the flux flow and explained the curved foot of the $V-I$ curve that marks the onset of dissipation. We have also determined the density of pinning sites at which optimum vortex pinning occurs. The critical current density can be increased for a certain strength of the external magnetic field by arranging the pinning sites in a regular triangular array so that each vortex is trapped by one pinning site. However, even for perfect matching of the vortex lattice and the pinning centres we find a critical current density of only about 5% of the depairing current indicating that other pinning mechanisms (e. g. magnetic impurities) must be applied to achieve current densities close to the theoretical limit.

The theoretical study of superconductors using the TDGL equations is computationally very expensive and has only very recently become feasible. However, it is a very promising method especially because different boundary conditions; structures in the material; and finite temperature effects can be included very easily and modelled accurately.

As discussed in the Introduction, Bose-Einstein condensation is of great importance in many areas of modern physics. We have studied two very different systems in which macroscopic quantum phenomena occur and have demonstrated that the direct numerical solution of appropriate wave equations is a fruitful approach and can provide new insight and answers to long standing questions.

Appendix A

Newton's method

The following appendices give some details about the numerical methods that have been applied in the simulations. Here, we describe a globally convergent method for nonlinear systems of equations, known as the Newton-Raphson method [108]. It has been used to find all time-independent solutions to the Gross-Pitaevskii and to the Ginzburg-Landau equations.

A.1 Root finding in one dimension

Perhaps the most basic of tasks is to solve a given equation numerically. Moving all terms of the equation to the left hand side, the problem can be written as

$$f(x) = 0 \, . \tag{A.1}$$

A very efficient root-finding routine is Newton's method, also called the Newton-Raphson method. Starting with an initial guess, $x^{(1)}$, it approximates the function $f(x)$ locally by its tangent line at the current point $x^{(p)}$ and uses the crossing point of the tangent with the abscissa as the next guess $x^{(p+1)}$ (see Fig. A.1). Algebraically, the function $f(x)$ is approximated by the first two terms of its Taylor series expansion:

$$f(x + \delta x) \approx f(x) + f'(x)\delta x \, . \tag{A.2}$$

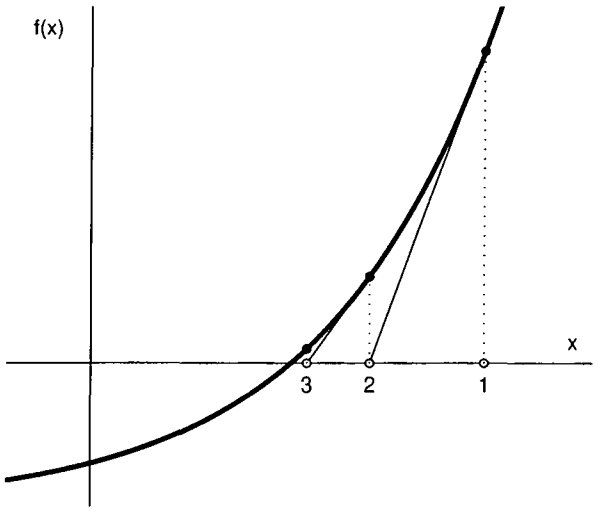

Figure A.1: Newton's method extrapolates the local derivative to find the next estimate of the root.

In many cases, the method converges quadratically, i. e. near the root, the number of significant digits approximately doubles with each step. However, the method can fail, for example, if the approximations encounter a local extremum. In this case, the tangent line is almost horizontal and a the next Newton step δx changes the initial guess dramatically. A cure for this problem will be discussed later. Implicit problems of the form (A.1) may have none or several solutions. Therefore, different initial values might cause the algorithm to converge to different roots. For some equations or initial values, the method might not converge at all.

A.2 Non-linear sets of equations

Newton's method is readily generalised to an N-dimensional problem

$$\boldsymbol{f}(\boldsymbol{x}) = 0 \,, \tag{A.3}$$

where $\boldsymbol{x}$ denotes the vector $\{x_u\}_{u=1,\ldots,N}$ and $\boldsymbol{f}$ the vector of functions $\{f_u\}_{u=1,\ldots,N}$. The first derivative is now replaced by the Jacobian matrix. In the neighbourhood

of $\boldsymbol{x}$, each component f_u can be approximated by

$$f_u(\boldsymbol{x}+\delta\boldsymbol{x}) \approx f_u(\boldsymbol{x}) + \sum_{v=1}^{N} \frac{\partial f_u}{\partial x_v}\delta x_v = 0 \; . \tag{A.4}$$

For each Newton step, $\boldsymbol{x}^{(p+1)} = \boldsymbol{x}^{(p)} + \delta\boldsymbol{x}$, the $N \times N$ matrix $J_{u,v}$ given by

$$J_{u,v} \equiv \frac{\partial f_u}{\partial x_v} \; , \tag{A.5}$$

has to be inverted. The algorithm fails if the procedure runs into a local extremum, i. e. the Jacobian matrix becomes singular.

As an example, we demonstrate how Newton's method can be applied to find time-independent solutions to the Gross-Pitaevskii equation in a moving frame,

$$\mathrm{i}\partial_t\psi = -\tfrac{1}{2}\nabla^2\psi + V\psi + |\psi|^2\psi + \mathrm{i}\boldsymbol{U}\cdot\nabla\psi \; . \tag{A.6}$$

Stationary flow solutions correspond to wavefunctions $\psi(\boldsymbol{r},t) = \mathrm{e}^{-i\mu t}\phi(\boldsymbol{r})$ with a chemical potential of $\mu = 1$. We discretise the equation on a three-dimensional Cartesian grid and separate the wavefunction into real and imaginary parts, because the term $|\psi|^2\psi$ cannot be differentiated unambiguously in the complex plane. The spatial derivatives are then approximated by second order accurate finite difference approximations. Defining $\phi_{ijk0} = \mathrm{Re}(\phi(x_i,y_j,z_k))$ and $\phi_{ijk1} = \mathrm{Im}(\phi(x_i,y_j,z_k))$, and taking the flow direction to define the z-axis, Eq. (A.6) becomes

$$\begin{aligned} f_{ijkr} \equiv \; & - \left(\phi_{i-1,j,k,r} - 2\phi_{i,j,k,r} + \phi_{i+1,j,k,r}\right)/2h_x^2 \\ & - \left(\phi_{i,j-1,k,r} - 2\phi_{i,j,k,r} + \phi_{i,j+1,k,r}\right)/2h_y^2 \\ & - \left(\phi_{i,j,k-1,r} - 2\phi_{i,j,k,r} + \phi_{i,j,k+1,r}\right)/2h_z^2 \\ & + \left(V_{i,j,k} + \phi_{i,j,k,0}^2 + \phi_{i,j,k,1}^2 - 1\right)\phi_{i,j,k,r} \\ & + (2r-1)U(\phi_{i,j,k+1,1-r} - \phi_{i,j,k-1,1-r})/2h_z = 0 \; , \end{aligned} \tag{A.7}$$

where h is the grid spacing (values between $\frac{1}{16}$ and $\frac{1}{2}$ were used). The solution of these equations is found using the linearisation

$$f_{ijkr}(\phi^{(p)}_{lmns}) + \sum_{lmns} \left(\phi^{(p+1)}_{lmns} - \phi^{(p)}_{lmns}\right) \left[\frac{\partial f_{ijkr}}{\partial \phi_{lmns}}\right]^{(p)} \approx 0 \,, \tag{A.8}$$

where $\phi^{(p+1)}$ is determined from the approximation $\phi^{(p)}$ by solving Eq. (A.8) using the bi-conjugate gradient method explained below. The iterative solution depends on the initial guess $\phi^{(1)}$; for example, laminar flows are found by choosing $\phi^{(1)} = 1$, whereas vortex solutions are found by imposing the vortex phase pattern on $\phi^{(1)}$, and then relaxing the imposed phase after a few iterations.

A.3 Bi-conjugate gradient method

Newton's method requires the solution of a linear system,

$$J\delta\boldsymbol{x} = -\boldsymbol{f} \,, \tag{A.9}$$

where J is the Jacobian of the non-linear system of equations and $\delta\boldsymbol{x}$ the Newton step. In our simulations, we use grid sizes up to 100^3 points. The length of the vectors $\boldsymbol{x}$ and $\boldsymbol{f}$ is $2 \cdot 100^3$ because the complex wavefunction is represented by two real-valued fields. That means the Jacobian matrix contains $4 \cdot 10^{12}$ elements. There are very few computers that could store this amount of data and even fewer that can invert such a matrix within a reasonable time. Luckily, the Jacobian matrix corresponding to Eq. (A.7) is very sparse; indeed, about 99.9995% of the matrix elements are zero.

We employ the so-called bi-conjugate gradient method [108] to find a solution to the matrix equation (A.9). The attractiveness of this method is that it references J only through its multiplication of a vector or the multiplication of its transpose and a vector, and J can be stored in a compact way making use of its sparseness.

The idea is to minimise the value of the scalar function

$$g(\boldsymbol{x}) = \frac{1}{2}\boldsymbol{x}^T \cdot J \cdot \boldsymbol{x} + \boldsymbol{f} \cdot \boldsymbol{x} \ . \tag{A.10}$$

which is equivalent to solving (A.9). The minimisation is performed by creating a succession of linearly independent search directions and going 'downhill' in each direction. After $N = \dim J$ iterations, the algorithm arrives at the global minimum of $g(\boldsymbol{x})$ and therefore at the solution of (A.9). However, an *approximate* solution of the form

$$|J\delta\boldsymbol{x} + \boldsymbol{f}|^2 < \alpha\,|\boldsymbol{f}|^2 \ , \qquad \alpha \sim 10^{-2} \ , \tag{A.11}$$

which is often sufficient for the Newton method, is typically generated after fewer than 10^3 iterations making it possible to solve very large sets of non-linear equations.

A.4 Truncated Newton steps

As discussed above, Newton's method converges quadratically close to a simple root of an equation but also has the tendency to jump away from the actual guess $\boldsymbol{x}^{(p)}$ if it encounters any local extremum. Far away from the solution, it is not clear if the linearised equation (A.4) is a good approximation to the the original set of the equations. However, it is guaranteed that $|\boldsymbol{f}|^2$ decreases initially as we move along the direction of the Newton step. To ensure global convergence of the algorithm, only a fraction of the calculated step is taken to update the approximation for the root,

$$\boldsymbol{x}^{(p+1)} = \boldsymbol{x}^{(p)} + \lambda\ \delta\boldsymbol{x} \ , \qquad 0 < \lambda \leq 1 \ . \tag{A.12}$$

Close to a solution, λ can be set to 1 and the algorithm will converge rapidly. For the first couple of steps, a value of about 0.1 is often necessary to guide the Newton steps along the N dimensional surface described by the system (A.3).

A.5 Coordinate system and the choice of variables

Symmetries in the underlying geometry can reduce the expense of the calculations. For example, if the potential V is symmetric along the flow direction $V(-z) = V(z)$, then clearly $\phi^*(-z) = \phi(z)$, and only half of the wavefunction needs to be modelled if appropriate boundary conditions are applied at $z = 0$. Both the GP and the GL equations have been solved using a number of different coordinate systems, namely

- Cartesian coordinates in one, two and three dimensions: x, y, z,
- polar and cylindrical coordinates: ρ, φ, z,
- spherical coordinates: r, φ, θ, and
- 'stretched' coordinates: $\hat{x}, \hat{y}, \hat{z}$ or $\hat{r}$.

The 'stretched' coordinates have been used to model very large box sizes by mapping the axis to the interval $[-1, 1]$ using the transformation $\hat{x} = x/(|x| + D)$, where D is a constant which determines the scaling. A more sophisticated example is the transformation

$$r = R + \frac{D\hat{r}^3}{1 - \hat{r}^3} , \qquad \hat{r} = [0, 1) , \tag{A.13}$$

that allows to study the flow around very large spheres with radii up to $R = 10000$. The non-linear transformation provides both sufficient point coverage of the healing length and a good resolution of the flow at large distances from the sphere.

It is important to note that the Newton method in combination with the bi-conjugate gradient method only finds *simple* zeros. For the time-independent Ginzburg-Landau equations,

$$\begin{aligned} 0 &= (\nabla - \mathrm{i}\boldsymbol{A})^2\psi + (1 - |\psi|^2)\psi \\ 0 &= (\nabla S - \boldsymbol{A})|\psi|^2 - \kappa^2 \nabla \times \nabla \times \boldsymbol{A} , \end{aligned} \tag{A.14}$$

a whole class of solutions exists due to the gauge freedom ($\boldsymbol{A} \to \boldsymbol{A} + \nabla\Lambda$ and $\psi \to \psi \mathrm{e}^{\mathrm{i}\Lambda}$). There is one particular choice of gauge that removes all the phase

gradients from the wavefunction. Writing $\psi = Re^{iS}$ and setting $\Lambda = -S$, the equations (A.14) become

$$\begin{aligned} 0 &= \nabla^2 R + (\boldsymbol{A}^2 + 1 - R^2)R \\ 0 &= \boldsymbol{A}R^2 + \kappa^2 \nabla \times \nabla \times \boldsymbol{A} \; . \end{aligned} \tag{A.15}$$

This set of equations is ideal for studying the Meissner state because all gauge freedom has been removed. However, in this gauge, the vector potential $\boldsymbol{A}$ diverges inside a vortex core so that a finite-difference approximation of the spatial derivatives cannot be used. We therefore rewrite the equations (A.15) using the gauge-invariant quantities: density, $D = R^2$, and the supercurrent, $\boldsymbol{j} = \boldsymbol{A}R^2$:

$$\begin{aligned} 0 &= \frac{D}{2}\nabla^2 D - \frac{1}{4}(\nabla D)^2 + \boldsymbol{j}^2 + D^2 - D^3 \\ 0 &= D^3 \boldsymbol{j} + \kappa^2 \left(\nabla \times \nabla \times (D^2 \boldsymbol{j}) - 3\nabla \times (D \nabla D \times \boldsymbol{j}) \right. \\ &\qquad \left. -3\nabla D \times \nabla \times (D\boldsymbol{j}) + 6\nabla D \times (\nabla D \times \boldsymbol{j}) \right) \; . \end{aligned} \tag{A.16}$$

These equation have been used to calculate the vortex solutions in Chapter 7. Both the density and the supercurrent are smooth functions inside a vortex core as shown in Fig. A.2.

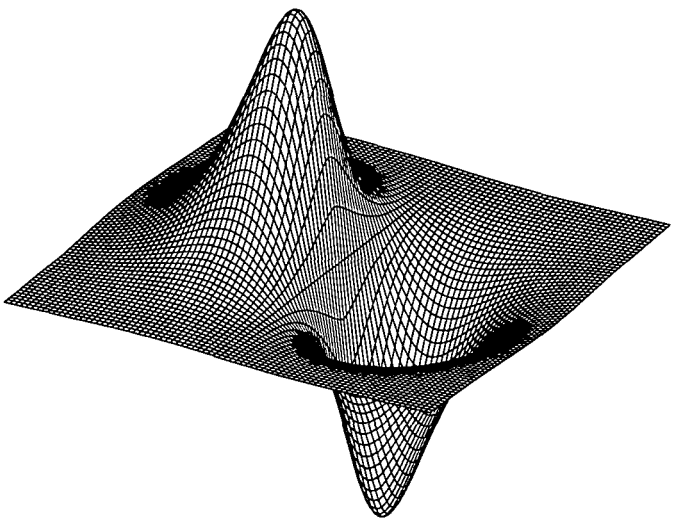

Figure A.2: One component of the supercurrent, $j_x(x, y)$, around a vortex. The vortex line is vertical in this plot and going through the middle. The supercurrent is an ideal variable for Newton's method: It is a gauge invariant and smooth.

Appendix B

Crank-Nicholson method

Here we describe the method used to solve the time-dependent Gross-Pitaevskii equation numerically. The Crank-Nicholson algorithm is second accurate in space and time and is renowned for its stability.

B.1 A semi-implicit finite difference scheme

The Crank-Nicholson algorithm [108, 109], is one of the standard routines for solving the multi-dimensional Schrödinger type equation,

$$\mathrm{i}\frac{\partial}{\partial t}\psi(\boldsymbol{x},t) = H\psi(\boldsymbol{x},t)\ . \tag{B.1}$$

The time evolution of the wavefunction is formally given by

$$\psi(\boldsymbol{x},t+\Delta t) = \exp(-\mathrm{i}\Delta t H)\psi(\boldsymbol{x},t)\ . \tag{B.2}$$

The operator $\exp(-\mathrm{i}\Delta t H)$ is replaced by a finite difference representation, called Cayley's form, which is second order accurate and uni-modular:

$$\mathrm{e}^{-\mathrm{i}\Delta t H} \simeq \frac{1-\frac{1}{2}\mathrm{i}\Delta t H}{1+\frac{1}{2}\mathrm{i}\Delta t H}\ . \tag{B.3}$$

In other words,

$$\left(1+\tfrac{1}{2}\mathrm{i}\Delta t H^{(n+1)}\right)\psi^{(n+1)} = \left(1-\tfrac{1}{2}\mathrm{i}\Delta t H^{(n)}\right)\psi^{(n)} \ , \tag{B.4}$$

where the superscript n denotes the time step. In the case of the NLSE, the Hamiltonian H depends on the wavefunction and is therefore time-dependent. It has been shown [110] that a second order accuracy in time can be retained if the Hamiltonian on the left hand side of the equation depends on the wavefunction at the new time level, $n+1$, whereas the Hamiltonian on the right hand side depends on the previous time level, n, as indicated in Eq. (B.4). The wavefunction at the new time level is obtained by an iteration technique and we assume $\psi^{(n+1)} = \psi^{(n)}$ initially.

In three dimensions, the kinetic energy part of the Hamiltonian contains derivatives in all three directions. However, the operators can be split into three one-dimensional operators within the second order accuracy [109]. This *approximate factorisation* allows fast matrix inversion routines to be employed.

B.2 The motion of a classical object in a quantum fluid

In chapter 4 we simulate the motion of a massive object through a quantum fluid. The object is modelled by a potential term $V(\boldsymbol{r}-\boldsymbol{r}_{\mathrm{o}}(t))$, where $\boldsymbol{r}_{\mathrm{o}}$ marks the position of the object. The dynamics of the quantum fluid is given by the NLSE while we assume a classical trajectory for the object:

$$\mathrm{i}\partial_t\psi(\boldsymbol{r},t) = \left(-\frac{1}{2}\nabla^2 + V(\boldsymbol{r}-\boldsymbol{r}_{\mathrm{o}}(t)) + |\psi(\boldsymbol{r},t)|^2\right)\psi(\boldsymbol{r},t) \ . \tag{B.5}$$

The equation of motion of the object is given by

$$M\ddot{\boldsymbol{r}}_{\mathrm{o}} = \boldsymbol{F} + \int \mathrm{d}^3 r \ \frac{\mathrm{d}V}{\mathrm{d}\boldsymbol{r}}|\psi(\boldsymbol{r},t)|^2 \ , \tag{B.6}$$

where $\boldsymbol{F}$ is an external force and the second term is the force on the object due to the fluid. The computation is simplified by transforming into the frame of the

object, where Eq. (B.5) may be rewritten as

$$\mathrm{i}\partial_t\tilde{\psi}(\boldsymbol{r}',t) = \left(-\frac{1}{2}\nabla^2 + V(\boldsymbol{r}') + |\tilde{\psi}(\boldsymbol{r}',t)|^2 + \mathrm{i}\boldsymbol{U}\cdot\nabla\right)\tilde{\psi}(\boldsymbol{r}',t)\ , \tag{B.7}$$

where $\tilde{\psi}(\boldsymbol{r}',t) = \psi(\boldsymbol{r},t)$ is the wavefunction in the fluid frame written in terms of the object frame coordinates, $\boldsymbol{r}' = \boldsymbol{r} - \boldsymbol{r}_0(t)$, and $\boldsymbol{U}$ is the object velocity at time t. The system is prepared in a time-independent laminar flow state, $\tilde{\psi}(\boldsymbol{r}',t) = \phi(\boldsymbol{r}')\mathrm{e}^{\mathrm{i}\mu t}$, where μ is the chemical potential. From this initial state, the time evolution due to an applied force, $\boldsymbol{F}$, is evaluated by integrating Eq. (B.7) using a semi-implicit Crank-Nicholson formula. The conservation of momentum

$$\boldsymbol{P}_0 + \boldsymbol{F}t = M\boldsymbol{U} + \frac{\mathrm{i}}{2}\int \mathrm{d}^3r'\,[\psi\nabla'\psi^* - \psi^*\nabla'\psi]\ , \tag{B.8}$$

where $\boldsymbol{P}_0$ is the initial momentum, is used to calculate the velocity of the object at each time step. The velocity at the new time level enters in $H^{(n+1)}$ on the left hand side of Eq. (B.4) and is found by iteration.

For the simulations in Chapter 4, the equations (B.7) and (B.8) are discretised on a three dimensional grid using the non-linear mapping $\hat{x} = x/(D+|x|)$, where $D = 12$ is used as a scaling parameter, to map an infinite box onto the space $[-1,1]$. The grid contains 140 points in each dimension and we use a time step $\mathrm{d}t = 0.02$.

The accuracy of the solution is assessed by comparing it to known solutions for special cases, and with solutions obtained using a much finer grid spacing and shorter time steps. In addition, physical features of the time-dependent solution such as the conservation of the number of particles, momentum, and energy can be considered to check the code is working correctly.

B.3 Imaginary time - The Gauss-Seidel method

The Crank-Nicholson formula can also be applied to find time-independent solutions to the NLSE of the form

$$\mu\psi = \left(-\frac{1}{2}\nabla^2\psi + V + |\psi|^2 + i\boldsymbol{U}\cdot\nabla\right)\psi \; = H\psi, \tag{B.9}$$

where μ is the chemical potential, $\mu = 1$ for homogeneous systems, and the momentum operator $i\boldsymbol{U}\cdot\nabla$ is incorporated to find soliton solutions around a moving object represented by the potential term V.

Consider the diffusion equation

$$\partial_t\psi = \mu\psi - H\psi \; =: \frac{1}{2}\nabla^2\psi - \frac{1}{2}\rho, \tag{B.10}$$

with a diffusion constant of $\frac{1}{2}$ and a source term ρ. As $t \to \infty$, the initial wavefunction relaxes to an equilibrium solution, usually to the time-independent ground state. This is known as the Gauss-Seidel method for solving the inhomogeneous Laplace equation $\nabla^2\psi = \rho$. The equation (B.10) is the NLSE where the time has been replaced by a negative 'imaginary' time. Therefore, propagating the wavefunction in an Crank-Nicholson code using negative and imaginary time-steps Δt is another way (besides the Newton method (Appendix 1)) of finding the ground state of a system. The procedure fails to converge if no ground state exists, for example, there are no time-independent solutions for flow around a sphere at supercritical velocities.

A 'complex time', i. e. the time step Δt has a real and imaginary components, can be used to incorporate dissipation into the Gross-Pitaevskii equations. Whereas the real part of the time drives the convection of the fluid, the negative imaginary part smoothes out excitations. However, care must be taken to conserve the number of particles in the system.

Appendix C

Semi-Implicit Finite Difference Method for the TDGL Equations

Here we present the finite-difference algorithm used for solving the time-dependent Ginzburg-Landau equation coupled to the appropriate Maxwell equation in this thesis. The time derivatives are discretised using a second order semi-implicit scheme which, for intermediate values of the Ginzburg-Landau parameter κ, allows time-steps two orders of magnitude larger than commonly used in explicit schemes. As an extra demonstration we use the method to solve a fully three-dimensional problem of a current-carrying wire with longitudinal and transverse magnetic fields.

C.1 Numerical methods

The most popular approach to the solution of the TDGL equations, (7.14) and (7.15), is a gauge-invariant discretisation that is second order accurate in space and first order in time [99, 97, 111, 112, 113]. In addition, a number of other finite difference [114, 115] and finite element methods [116, 117] have been developed. For large values of κ the magnetic field is nearly homogeneous and equation (7.15) can be dropped. This case is often referred to as the London limit. The remaining equation has been solved by a semi-implicit Fourier spectral method which is second order

accurate in time [118]. Here, we modify the very robust and accurate semi-implicit Crank-Nicholson algorithm discussed in Appendix 2 to include the equation for the vector potential.

C.1.1 The $U-\psi$ method

The widely used $U-\psi$ method is described in detail by Gropp *et al.* [111]. As this method forms the basis of our algorithm we briefly review the main points here. Complex link variables U^x, U^y and U^z are introduced to preserve the gauge invariant properties of the discretised equations:

$$\begin{aligned} U^x(x,y,z) &= \exp\left(-\mathrm{i}\int_{x_0}^{x} A^x(x',y,z)\mathrm{d}x'\right) \\ U^y(x,y,z) &= \exp\left(-\mathrm{i}\int_{y_0}^{y} A^y(x,y',z)\mathrm{d}y'\right) \\ U^z(x,y,z) &= \exp\left(-\mathrm{i}\int_{z_0}^{z} A^z(x,y,z')\mathrm{d}z'\right) , \end{aligned} \tag{C.1}$$

where (x_0, y_0, z_0) is an arbitrary reference point. The TDGL equations can then be expressed as functions of ψ and these link variables. Both the order parameter and the link variables are discretised on a three dimensional grid with grid spacing h_x, h_y, and h_z, respectively. The mesh points for the link variables are half way between the mesh points for the order parameter (see Fig. C.1). All spatial derivatives are approximated by finite differences to second order accuracy. Denoting the complex conjugate of U by $\overline{U}$, the finite difference representations of the TDGL equations read

$$\begin{aligned} \partial_t \psi_{i,j,k} &= \frac{\overline{U}^x_{i-1,j,k}\psi_{i-1,j,k} - 2\psi_{i,j,k} + U^x_{i,j,k}\psi_{i+1,j,k}}{h_x^2} \\ &+ \frac{\overline{U}^y_{i,j-1,k}\psi_{i,j-1,k} - 2\psi_{i,j,k} + U^y_{i,j,k}\psi_{i,j+1,k}}{h_y^2} \\ &+ \frac{\overline{U}^z_{i,j,k-1}\psi_{i,j,k-1} - 2\psi_{i,j,k} + U^z_{i,j,k}\psi_{i,j,k+1}}{h_z^2} \\ &+ (1 - |\psi_{i,j,k}|^2)\psi_{i,j,k} \end{aligned} \tag{C.2}$$

$$\partial_t U^x_{i,j,k} = -\mathrm{i}\,\mathrm{Im}\left(\mathcal{F}^x_{i,j,k}\right) U^x_{i,j,k} , \tag{C.3}$$

where

$$\begin{aligned}\mathcal{F}^x_{i,j,k} &= \kappa^2 \frac{\overline{U}^x_{i,j+1,k}\overline{U}^y_{i,j,k}U^x_{i,j,k}U^y_{i+1,j,k} - \overline{U}^x_{i,j,k}\overline{U}^y_{i,j-1,k}U^x_{i,j-1,k}U^y_{i+1,j-1,k}}{h_y^2} \\ &+ \kappa^2 \frac{\overline{U}^z_{i+1,j,k-1}\overline{U}^x_{i,j,k-1}U^z_{i,j,k-1}U^x_{i,j,k} - \overline{U}^z_{i+1,j,k}\overline{U}^x_{i,j,k}U^z_{i,j,k}U^x_{i,j,k+1}}{h_z^2} \\ &+ U^x_{i,j,k}\overline{\psi}_{i,j,k}\psi_{i+1,j,k} \ .\end{aligned}$$

Analogous expressions for $\partial_t U^y_{i,j,k}$ and $\partial_t U^z_{i,j,k}$ can be obtained by permutating the coordinates and indices as follows:

$$(x,y,z;i,j,k) \rightarrow (y,z,x;j,k,i) \rightarrow (z,x,y;k,i,j) \rightarrow (x,y,z;i,j,k) \ . \tag{C.4}$$

The standard method approximates the time evolution by a simple Euler step,

$$\psi_{i,j,k}(t+\Delta t) = \psi_{i,j,k}(t) + \Delta t \ \partial_t \psi_{i,j,k}(t) + \mathcal{O}(\Delta t^2) \tag{C.5}$$

$$U^x_{i,j,k}(t+\Delta t) = U^x_{i,j,k}(t) + \Delta t \ \partial_t U^x_{i,j,k}(t) + \mathcal{O}(\Delta t^2) \ . \tag{C.6}$$

To keep $U^x_{i,j,k}$ uni-modular, equation (C.6) is often modified to

$$U^x_{i,j,k}(t+\Delta t) = U^x_{i,j,k}(t) \exp\left(-\mathrm{i}\Delta t \ \mathrm{Im}\mathcal{F}^x_{i,j,k}\right) + \mathcal{O}(\Delta t^2) \ . \tag{C.7}$$

The Euler method is only first order accurate in time, i.e., the truncation error made due to the finite difference approximation of the time derivative is proportional to Δt^2. However, the main problem is that the code becomes unstable if long time steps are used. The cause of this instability is the diffusion-like character of the dynamics described by the equations (C.2) and (C.3). Equation (C.2) can immediately be written as a diffusion equation with an additional non-linear term

$$\partial_t \psi_{i,j,k} = L_x\psi_{i,j,k} + L_y\psi_{i,j,k} + L_z\psi_{i,j,k} + f \ , \tag{C.8}$$

where f stands for $(1-|\psi_{i,j,k}|^2)\psi_{i,j,k}$ and L_x, L_y, and L_z denote the *weighted* Laplacian operators,

$$L_x\psi_{i,j,k} \equiv \frac{a_{i-1}\psi_{i-1,j,k} - 2\psi_{i,j,k} + a_{i+1}\psi_{i+1,j,k}}{h_x^2} \ , \tag{C.9}$$

with $|a_{i-1}| = |a_{i+1}| = 1$ in our case. The diffusion constant is 1 in dimensionless units. Equation (C.3) is also dominated by diffusive terms as will become evident in the next section. The diffusion constant for the vector potential is κ^2. This can be seen by taking the curl of equation (7.15), $\dot{\boldsymbol{B}} = \kappa^2 \nabla^2 \boldsymbol{B} + \nabla \times \boldsymbol{j}_s$. The one-step forward Euler method is only stable as long as the time step is shorter than the diffusion time across a cell of width h [108]. For example, using a grid spacing of $h = 0.5\xi$ and $\kappa = 4$, the theoretical limit for the time step is

$$\Delta t < \frac{h^2}{2\kappa^2} = \frac{0.5^2}{2 \cdot 4^2} \approx 0.0078 \ . \tag{C.10}$$

In practice, a time step of $\Delta t = 0.0025$ is used to ensure stability [111]. In contrast, a semi-implicit two-step algorithm is unconditionally stable for diffusive problems and enables much larger time-steps to be employed.

C.1.2 Semi-implicit algorithm

We propose a spatial discretisation of the equations very similar to the above $U - \psi$ method. The link variables are uni-modular, $|U^x_{i,j,k}| = 1$, and can be written as the exponential of a phase, $U^x_{i,j,k} = \exp(-\mathrm{i}\phi^x_{i,j,k})$. We use the real-valued variable ϕ^x instead of the complex-valued U^x. The fields ψ and $\boldsymbol{\phi}$ are represented on a three-dimensional grid. The mesh points of the phase factors are placed between the mesh points of the order parameter (see Fig. C.1). For the field $\psi_{i,j,k}$, the grid point indices are $i = 1...N_x + 1$, $j = 1...N_y + 1$, and $k = 1...N_z + 1$. For $\phi^x_{i,j,k}$, the indices in the x direction range $i = 1...N_x$ only, due to the relative displacement of the grids. Similarly, $j = 1...N_y$ for $\phi^y_{i,j,k}$ and $k = 1...N_z$ for $\phi^z_{i,j,k}$.

We now discretise the spatial derivatives in equations (7.14) and (7.15) using the modified link variables ϕ^x, ϕ^y, and ϕ^z. For equation (7.14), we can reuse the expan-

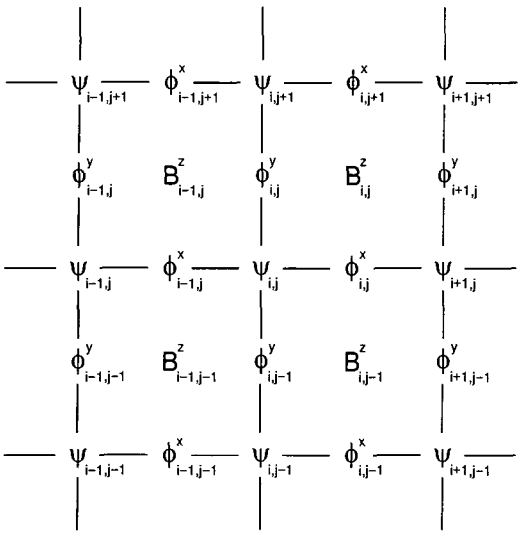

Figure C.1: The evaluation points for the fields ψ and ϕ in the $x-y$ plane. A finite difference approximation for the magnetic field B_z is given in (C.27).

sion (C.2) except that $U^x_{i,j,k}$ is replaced by $\exp(-\mathrm{i}\phi^x_{i,j,k})$, etc,

$$\begin{aligned}
\partial_t \psi_{i,j,k} &= \frac{\exp(\mathrm{i}\phi^x_{i-1,j,k})\psi_{i-1,j,k} - 2\psi_{i,j,k} + \exp(-\mathrm{i}\phi^x_{i,j,k})\psi_{i+1,j,k}}{h_x^2} \\
&+ \frac{\exp(\mathrm{i}\phi^y_{i,j-1,k})\psi_{i,j-1,k} - 2\psi_{i,j,k} + \exp(-\mathrm{i}\phi^y_{i,j,k})\psi_{i,j+1,k}}{h_y^2} \\
&+ \frac{\exp(\mathrm{i}\phi^z_{i,j,k-1})\psi_{i,j,k-1} - 2\psi_{i,j,k} + \exp(-\mathrm{i}\phi^z_{i,j,k})\psi_{i,j,k+1}}{h_z^2} \\
&+ (1 - |\psi_{i,j,k}|^2)\psi_{i,j,k} \ .
\end{aligned} \tag{C.11}$$

With help of the relation $-\nabla \times \nabla \times \boldsymbol{A} = \nabla^2 \boldsymbol{A} - \nabla(\nabla \boldsymbol{A})$, the second order accurate finite difference representation of (7.15) is

$$\begin{aligned}
\partial_t \phi^x_{i,j,k} &= \frac{\kappa^2}{h_y^2}(\phi^x_{i,j+1,k} - 2\phi^x_{i,j,k} + \phi^x_{i,j-1,k}) + \frac{\kappa^2}{h_z^2}(\phi^x_{i,j,k+1} - 2\phi^x_{i,j,k} + \phi^x_{i,j,k-1}) \\
&+ \frac{\kappa^2}{h_y^2}(-\phi^y_{i+1,j,k} + \phi^y_{i,j,k} + \phi^y_{i+1,j-1,k} - \phi^y_{i,j-1,k}) \\
&+ \frac{\kappa^2}{h_z^2}(-\phi^z_{i+1,j,k} + \phi^z_{i,j,k} + \phi^z_{i+1,j,k-1} - \phi^z_{i,j,k-1})
\end{aligned}$$

$$+ \quad \mathrm{Im}\left(\exp(-\mathrm{i}\phi^x_{i,j,k})\overline{\psi}_{i,j,k}\psi_{i+1,j,k}\right) \ . \tag{C.12}$$

The expressions for $\partial_t \phi^y_{i,j,k}$ and $\partial_t \phi^z_{i,j,k}$ are given by cyclic permutation (C.4).

Note, that the discretised equations are still invariant under the gauge transformation

$$\begin{cases} \psi_{i,j,k} & \rightarrow \psi_{i,j,k}\exp(\mathrm{i}\Lambda_{i,j,k}) \\ \phi^x_{i,j,k} & \rightarrow \phi^x_{i,j,k} + (\Lambda_{i+1,j,k} - \Lambda_{i,j,k}) \\ \phi^y_{i,j,k} & \rightarrow \phi^y_{i,j,k} + (\Lambda_{i,j+1,k} - \Lambda_{i,j,k}) \\ \phi^z_{i,j,k} & \rightarrow \phi^z_{i,j,k} + (\Lambda_{i,j,k+1} - \Lambda_{i,j,k}) \ . \end{cases} \tag{C.13}$$

Retaining the gauge invariance at the discrete level is often equivalent to preserving certain conservation laws and physical principles. It is crucial that the numerical approximation does not depend on the particular choice of gauge. If, for example, one studies the motion of a vortex lattice due to an applied electric field E_x, the measurable quantities $\boldsymbol{B}$, $|\psi|^2$ and $\boldsymbol{j}$ oscillate in time (see Chapter 8). The system is driven through a series of equivalent solutions and the dynamics is roughly described by $\Lambda = E_x x t$. This means that the phase gradients in the order parameter build up in time and the phase difference between two neighbouring grid points eventually exceeds 2π. This is normally a problem as the finite difference approximation becomes invalid. However, using the link variables U or ϕ these phase gradients are exactly cancelled by the change in the vector potential.

We now want to introduce a new scheme to update the wavefunction $\psi^{(n)}$ and the link variables $\phi^{(n)}$ from the nth to the $(n+1)$th step. The idea is to treat the diffusive terms semi-implicitly whereas all other terms are still treated explicitly. In this way we reduce the stability constraints associated with the simple Euler method but avoid the expensive solution of non-linear equations. The technique is known as *the method of fractional steps* [109]. A second-order accuracy in the time-step can be achieved by a simple 3 step iteration.

As mentioned above, the diffusive character of equation (7.15) becomes apparent in the new discretisation and both equation (C.11) and equation (C.12) can be written

as a initial value problem of the form

$$\partial_t u_{i,j,k} = D\left(L_x u_{i,j,k} + L_y u_{i,j,k} + L_z u_{i,j,k}\right) + f \ , \tag{C.14}$$

where u stands for the fields ψ or ϕ^x, ϕ^y or ϕ^z, respectively, D is the diffusion constant with $D = \kappa^2$ in (C.12) and f indicates all the other terms, $(1-|\psi_{i,j,k}|^2)\psi_{i,j,k}$ in (C.11) and the last three lines in equation (C.12). Note, that $L_x \equiv 0$ in (C.12).

The second derivatives are approximated in the usual way by an expression involving three neighbouring grid points. For any pair (j,k) the action of L_x on the vector $\{u_{i,j,k}\}_{i=2\ldots N_x}$, can be represented by a tri-diagonal matrix δ_x^2,

$$L_x u_{i,j,k} \equiv \frac{\delta_x^2}{h_x^2} u_{i,j,k} \equiv \frac{a_{i-1}u_{i-1,j,k} - 2u_{i,j,k} + a_{i+1}u_{i+1,j,k}}{h_x^2} \ . \tag{C.15}$$

As emphasised before, the instabilities of the Euler method have their origin in the explicit treatment of the diffusive terms. We now discretise the time derivative in equation (C.14) in the following way,

$$\begin{aligned} \frac{u^{(n+1)} - u^{(n)}}{\Delta t} = & \frac{D\delta_x^2}{2h_x^2}\left(u^{(n+1)} + u^{(n)}\right) + \frac{D\delta_y^2}{2h_y^2}\left(u^{(n+1)} + u^{(n)}\right) \\ & + \frac{D\delta_z^2}{2h_z^2}\left(u^{(n+1)} + u^{(n)}\right) + \frac{1}{2}\left(f^{(n+1)} + f^{(n)}\right) + \mathcal{O}(\Delta t^2) \ . \end{aligned} \tag{C.16}$$

This discretisation is semi-implicit as the right hand side of the equation depends on the fields at the old and the new time level. This mixing leads to an improved accuracy and prevents the algorithm from developing instabilities. After rearranging the equation we get

$$\begin{aligned} & \left(1 - \frac{D\Delta t}{2h_x^2}\delta_x^2 - \frac{D\Delta t}{2h_y^2}\delta_y^2 - \frac{D\Delta t}{2h_z^2}\delta_z^2\right) u^{(n+1)} = \frac{\Delta t}{2}\left(f^{(n+1)} + f^{(n)}\right) \\ & \left(1 + \frac{D\Delta t}{2h_x^2}\delta_x^2 + \frac{D\Delta t}{2h_y^2}\delta_y^2 + \frac{D\Delta t}{2h_z^2}\delta_z^2\right) u^{(n)} + \mathcal{O}(\Delta t^3) \ . \end{aligned} \tag{C.17}$$

We now employ an *approximate factorisation* [109],

$$\begin{aligned}&\left(1-\frac{D\Delta t}{2h_x^2}\delta_x^2-\frac{D\Delta t}{2h_y^2}\delta_y^2-\frac{D\Delta t}{2h_z^2}\delta_z^2\right)=\\&\left(1-\frac{D\Delta t}{2h_x^2}\delta_x^2\right)\left(1-\frac{D\Delta t}{2h_y^2}\delta_y^2\right)\left(1-\frac{D\Delta t}{2h_z^2}\delta_z^2\right)+\mathcal{O}(\Delta t^2)\,.\end{aligned} \tag{C.18}$$

The multidimensional operator is split into three operators that involve difference approximations in only one dimension. With the abbreviations

$$A_x=\left(1-\frac{D\Delta t}{2h_x^2}\delta_x^2\right),\ B_x=\left(1+\frac{D\Delta t}{2h_x^2}\delta_x^2\right), \tag{C.19}$$

and considering $(u^{(n+1)}-u^{(n)})=\mathcal{O}(\Delta t)$ equation (C.17) becomes

$$A_xA_yA_zu^{(n+1)}=B_xB_yB_zu^{(n)}+\frac{\Delta t}{2}\left(f^{(n+1)}+f^{(n)}\right)+\mathcal{O}(\Delta t^3)\,. \tag{C.20}$$

The tri-diagonal matrices A and B are actually time dependent because the differential operators L in equation (C.11) depend on the link variables. In the above equation, A is a function of $\phi^{(n+1)}$ whereas B depends on $\phi^{(n)}$. Consequently, the equations are solved in the following step-wise manner

$$\begin{aligned}A_xu^{(n+1/3)}&=B_xB_yB_zu^{(n)}+\frac{\Delta t}{2}\left(f^{(n+1)}+f^{(n)}\right)\\A_yu^{(n+2/3)}&=u^{(n+1/3)}\\A_zu^{(n+1)}&=u^{(n+2/3)}\,,\end{aligned} \tag{C.21}$$

where the 'fractional' time levels indicate intermediate results. The explicit term $f^{(n+1)}$ as well as the matrix elements of A may depend on the values of the link variables at the new time level and are unknown initially. We assume that $u^{(n+1)}=u^{(n)}$ to start with. After the first iteration of equation (C.21) for *all* variables ψ and ϕ, the updated values at the new time level are used in the matrix elements of A for the second iteration, and so on. The product $B_xB_yB_zu^{(n)}$ is a function of known values at the previous time level and can be stored in an auxiliary variable for subsequent iterations. As the matrices A are tri-diagonal, fast inversion routines can be applied [108].

The entire algorithm relies on the convergence of this iteration technique. To test whether the procedure converges, we calculate a total update, $S(m)$, of the fields after m iterations by comparing all values at the time level $(n+1)$ to all values at the previous time step, (n),

$$S(m) = \sum_{i,j,k} \left(\left(\left|\psi_{i,j,k}^{(n+1,m)}\right|^2 - \left|\psi_{i,j,k}^{(n)}\right|^2 \right)^2 + \left(\phi_{i,j,k}^{x(n+1,m)} - \phi_{i,j,k}^{x(n)} \right)^2 + \ldots \right), \quad \text{(C.22)}$$

where the three dots indicate the corresponding terms for the fields ϕ^y and ϕ^z. Fig. C.2 shows a typical evolution of the update for a time step of $\Delta t = 0.5$. After as few as five iterations the approximated increment is very close to the exact value. For smaller time steps, the procedure converges faster. We find an optimum trade-off between accuracy and performance for three iterations. We further check, if the correction between two successive iterations,

$$T(m) = \sum_{i,j,k} \left(\left(\left|\psi_{i,j,k}^{(n+1,m)}\right|^2 - \left|\psi_{i,j,k}^{(n+1,m-1)}\right|^2 \right)^2 + \left(\phi_{i,j,k}^{x(n+1,m)} - \phi_{i,j,k}^{x(n+1,m-1)} \right)^2 + \ldots \right), \quad \text{(C.23)}$$

converges to zero. Fig. C.2 (inset) confirms an exponential convergence.

The accuracy of the method is assessed by comparing the solution to simulations using the Euler method with a much smaller time step, $\Delta t = 0.0025$. Up to a time step of $\Delta t = 0.5$, no significant deviations could be observed. The program runs about 40 times faster than the Euler method for these parameters. For the calculations below we use a finer grid ($h = 0.4$) and a slightly larger Ginzburg-Landau parameter ($\kappa = 5$). The speed-up for these values is about 100.

Our implicit method is less memory intensive than the standard $U - \psi$ method because it uses real-valued link variables rather than complex-valued ones that must be represented by two real numbers. For a grid of N^3 points, the Euler method uses an equivalent of $22N^3$ real-valued variables (the complex wavefunction and the three complex link variables at two time levels plus three complex fields W, see [111]) whereas the implicit method requires the storage of a total of $19N^3$ variables

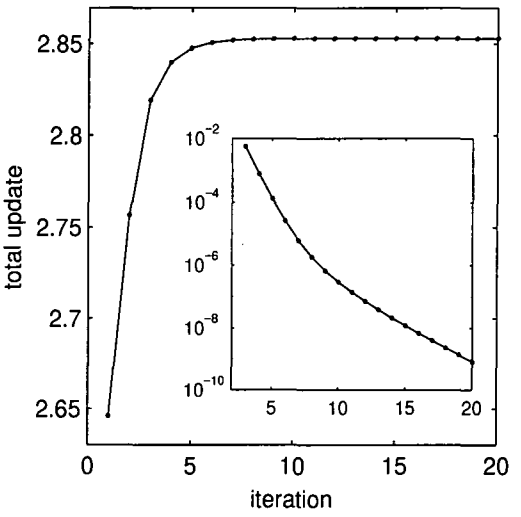

Figure C.2: The modification to the solution after one time step (total update) versus the number of iterations. For smaller time-steps, the solution converges faster. We find an optimum of speed and accuracy for a combination of three iterations and a time-step of $\Delta t = 0.5$. The correction between iterations, $T(m)$ is shown inset.

(the complex wavefunction and the three real link variables at two time levels, the products $B_x B_y B_z u^{(n)}$ in (C.21) plus four auxiliary fields).

C.1.3 Boundary conditions

The correct implementation of the boundary conditions requires great care because of the relative displacement of the grids. The matrices A_x and B_x only act on the interior points, $i = 2...N_x$, of the vectors ψ_i, ϕ_i^y, and ϕ_i^z for all $j = 1...N_y + 1, k = 1...N_z + 1$. Note, that $A_x = B_x \equiv 1$ in the case $u = \phi^x$. The end points $i = 1$ and $i = N_x + 1$ are computed for book-keeping purposes. Similarly, the operators B_y and B_z do not automatically include information on the end points at $j = 1, N_y + 1$ and $k = 1, N_z + 1$, respectively. In addition, there are different boundary conditions, namely periodic, Dirichlet and Neumann boundary conditions, that require an adaption of the matrix elements on the first and last row [108].

Another complication is that the physical boundary conditions that apply for the vectors $u^{(n)}$ and $u^{(n+1)}$ in equation (C.21) do not necessarily apply for the interme-

diate results $u^{(n+1/3)}$ and $u^{(n+2/3)}$. When, for example, solving the second equation of the system (C.21),

$$A_y u^{(n+2/3)} = u^{(n+1/3)}, \tag{C.24}$$

a correct treatment of the boundary condition for $u^{(n+2/3)} = A_z u^{(n+1)}$ must be implemented into A_y. The matrices A_x, A_y, and A_z commute as they act in different directions. It is therefore advisable to solve (C.21) starting in the direction with the simplest boundary condition. For a periodic boundary condition, for example, the relations $u_1 = u_N$ and $u_{N+1} = u_2$ hold at all time levels, including 'fractional' ones.

The boundary conditions depend on the geometry of the problem. We choose a system with a periodic boundary condition in the z-direction. At the interfaces in the x- and the y-direction, boundary conditions for the magnetic field and the order parameter are applied. For the order parameter, $\psi_{i,j,k}$, conditions are needed for all values at the faces of the three-dimensional box. The grid representation of the periodic boundary condition reads

$$\begin{array}{rclcrcl} \psi_{i,j,1} & = & \psi_{i,j,N_z}\,, & & \psi_{i,j,N_z+1} & = & \psi_{i,j,2} \\ \phi^x_{i,j,1} & = & \phi^x_{i,j,N_z}\,, & & \phi^x_{i,j,N_z+1} & = & \phi^x_{i,j,2}\,. \end{array} \tag{C.25}$$

In the y and z direction we set the supercurrent across the boundary to zero [111], i. e.,

$$\begin{array}{rcl} \psi_{1,j,k} & = & \psi_{2,j,k}\exp(-\mathrm{i}\phi^x_{1,j,k}) \\ \psi_{N_x+1,j,k} & = & \psi_{N_x,j,k}\exp(+\mathrm{i}\phi^x_{N_x,j,k}) \\ \psi_{i,1,k} & = & \psi_{i,2,k}\exp(-\mathrm{i}\phi^y_{i,1,k}) \\ \psi_{i,N_y+1,k} & = & \psi_{i,N_y,k}\exp(+\mathrm{i}\phi^y_{i,N_y,k})\,. \end{array} \tag{C.26}$$

Expressions for the end points of the link variables can be found by incorporating information of the magnetic field at the boundaries of the box. The three components of the magnetic field are given by the following second order finite-difference approximations.

$$B^x_{i,j,k} = \frac{1}{h_y h_z}(\phi^y_{i,j,k} - \phi^y_{i,j,k+1} - \phi^z_{i,j,k} + \phi^z_{i,j+1,k})$$

$$B^y_{i,j,k} = \frac{1}{h_z h_x}(\phi^z_{i,j,k} - \phi^z_{i+1,j,k} - \phi^x_{i,j,k} + \phi^x_{i,j,k+1}) \tag{C.27}$$
$$B^z_{i,j,k} = \frac{1}{h_x h_y}(\phi^x_{i,j,k} - \phi^x_{i,j+1,k} - \phi^y_{i,j,k} + \phi^y_{i+1,j,k}) \ .$$

From these expressions, appropriate boundary conditions can be obtained. For example, the field $\phi^x_{i,j,k}$ is unknown at $j = 1$, and we use the last equation to relate the values of $\phi^x_{i,1,k}$ to known values

$$\phi^x_{i,1,k} = -B^z_{i,1,k} h_x h_y + \phi^x_{i,2,k} + \phi^y_{i,1,k} - \phi^y_{i+1,1,k} \ . \tag{C.28}$$

Equation (C.11), (C.12) and (C.21) combined with the boundary conditions (C.25), (C.26), and (C.28) provide all the information needed to solve a three-dimensional problem.

C.2 Example 1: Wire with longitudinal field

As an example, we model an infinite cylindrical wire in three dimensions with an external magnetic field, H_z, applied along its axis. Such a configuration has been studied in [115, 119, 120]. Experiments have shown that the magnetic field can increase the critical current down the wire [121].

In a type-II superconductor, a sufficiently strong magnetic field, H_z, will enter the cylinder and become trapped in vortex tubes aligned parallel to the axis of the cylinder. A current I along the wire induces an additional circular field $H_\varphi(\boldsymbol{r})$ such that $I = 2\pi\rho\kappa^2 H_\varphi(\rho)$ at a distance ρ from the axis of the wire. The vortex tubes corresponding to the current- induced H_φ field are rings coaxial with the wire. Above a critical current, these vortex rings enter at the edge of the cylinder and shrink until they annihilate on the axis of the cylinder. This process repeats and leads to dissipation. There is no stable mixed state associated with a H_φ field unless the vortex rings are pinned by impurities in the material. Blackburn *et al.* [115] have argued, that by entangling the vortex rings with vortex lines due to a strong longitudinal field, the rings can be prevented from shrinking and thereby increase the critical current in the wire.

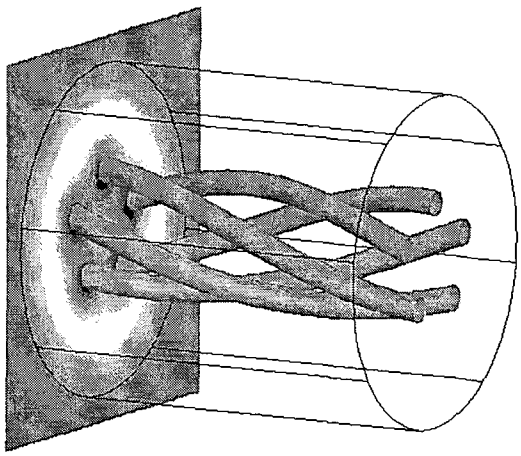

Figure C.3: Time-independent arrangement of spiral vortices in a cylinder of radius 12ξ, $\kappa = 5$. Five vortex lines are entangled with two rings. The applied fields are $H_z = 0.2$ and $H_\varphi = 1.5/\rho$, respectively. The tubes show the density of the order at the level $|\psi|^2 = 0.3$. The left slice shows the magnetic field component parallel to the wire, H_z, dark regions indicate a high field. The black lines mark the boundaries of the wire.

We model a cylindrical shape of the wire in a rectangular box by adding a potential term $V\psi$ with $V = 5$ to equation (7.14) at all grid points outside a cylindrical region with radius $R = 12\xi$. The density of the order parameter outside the cylinder decreases rapidly to zero. An array of longitudinal vortex tubes is created by imposing boundary conditions for an external magnetic field parallel to the wire. A current is ramped up by slowly increasing a circular field (B_x and B_y) around the box until vortices enter. The Bean-Livingston surface barrier was lowered by adding a weak sinusoidal potential at the surface of the cylinder. Fig. C.3 shows a time-independent state that arises after two vortex rings have entered the cylinder and entangled with the vortex lines. The critical current is dominated by the surface barrier as expected for small samples. Consequently, we do not observe any improvement in the critical current due to the presence of a longitudinal field. However, the effect could become more significant for larger sample sizes or if the surface effects are suppressed.

C.3 Example 2: Wire with transverse field

In superconducting magnets, the external magnetic field is typically aligned perpendicular to the wire (B_x for example). In the mixed state, an array of vortex lines fills the superconductor (see Fig. C.4). Any current carried by the wire superimposes a circular field onto this applied field. As a result, a gradient of the magnetic field develops that can be associated with a Lorentz force on the vortices. In most applications, different pinning mechanisms balance this Lorentz force and freeze the flux lattice up to a critical current density. For larger currents, the Lorentz force exceeds the pinning force and vortices start moving (Chapter 8). The motion of the flux lattice coincides with the breakdown of superconductivity.

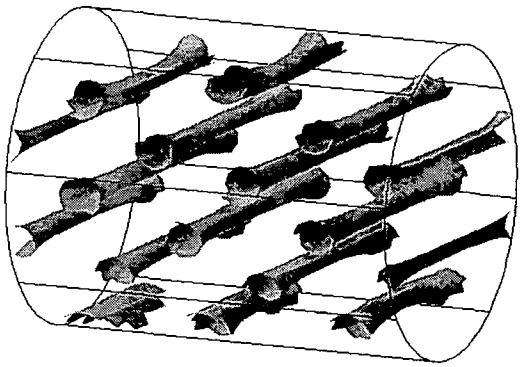

Figure C.4: Array of vortices in a wire exposed to a perpendicular magnetic field $B_x = 0.4$. The vortex tubes enter end exit the surface of the superconductor normally. The Ginzburg-Landau parameter is $\kappa = 5$, the radius of the wire $R = 8\xi$.

In this geometry the magnetic field at the boundary of the computational box strongly depends on the currents inside unless the box size is much larger than the radius R of the cylinder. In the Meissner state, for example, no flux lines penetrate the wire and supercurrents in the surface of the superconductor cancel the external field in the bulk of the wire. The field lines of these surface currents also extend outside the sample at length scales of order R. In the mixed state, the induced field is smaller and can be regarded as a small correction. To find a self-consistent

solution, the fields induced by both the supercurrents and normal currents have to be added to the applied field and included in the boundary conditions at each time step. We calculate the induced field $\boldsymbol{H}_{\mathrm{ind}}(\boldsymbol{r})$ using the Biot-Savart law, which in our units has the form,

$$\boldsymbol{H}_{\mathrm{ind}}(\boldsymbol{r}) = \frac{1}{4\pi\kappa^2} \int \mathrm{d}^3 r' \boldsymbol{j}(\boldsymbol{r}') \times \frac{\boldsymbol{r} - \boldsymbol{r}'}{|\boldsymbol{r} - \boldsymbol{r}'|^3} \,. \tag{C.29}$$

This calculation is computationally expensive. The integral is approximated by summing over all grid points for each boundary point requiring a total of $\mathcal{O}(N^5)$ calculations, whereas a time step takes $\mathcal{O}(N^3)$ calculations for a box of N^3 grid points. With periodic boundary conditions, the integration must also be extended to regions outside the box. The effect of including $\boldsymbol{H}_{\mathrm{ind}}$ is to bend the vortex lines, especially near the top and the bottom of the sample as apparent in Fig. C.4. To model the motion of flux lines, a fully self-consistent time-dependent solution can be found by iterating the boundary conditions at each time-step. However, in practice the study of the motion of vortices above the critical current does not seem to be feasible. Possible ways around this problem are to increase the box size so that the induced currents can be neglected, to cut-off the integral in (C.29) at a certain distance from the boundary, $|\boldsymbol{r} - \boldsymbol{r}'| < \mathcal{R}$, or to update $\boldsymbol{H}_{\mathrm{ind}}(\boldsymbol{r})$ only in larger intervals rather than every time step. The latter approach is especially suitable for finding time-independent solutions.

Bibliography

[1] D. W. Snoke and G. Baym *Unifying Themes of Bose-Einstein Condensation* in A. Griffin, D. W. Snoke and S. Stringari *Bose-Einstein Condensation*, (Cambridge University Press, 1995)

[2] T. W. B. Kibble, *Topology of cosmic domains and strings*, J. Phys. A: Math. Gen. **9**, 1387 (1976)

[3] M. B. Hindmarsh and T. W. B. Kibble, *Cosmic Strings*, Rep. Prog. Phys. **58**, 477 (1995)

[4] S. N. Bose, *Plancks Gesetz und Lichtquantenhypothese*, Z. Phys. **26**, 178 (1924)

[5] A. Einstein, *Quantentheorie des einatomigen idealen Gases*, Sitzber. Kgl. Preuss. Akad. Wiss. (1924)

[6] D. R. Tilley and J. Tilley, *Superfluidity and superconductivity*, 3rd Ed., (IoP, Bristol, 1990)

[7] R. J. Donnelly *Quantized vortices in Helium II*, (CUP, Cambridge, 1991)

[8] C. M. Muirhead, W. F. Vinen, and R. J. Donnelly, *The Nucleation of Vorticity by Ions in Superfluid* ^{4}*He*, Phil. Trans. R. Soc. Lond. A **311**, 433 (1984)

[9] M. Tinkham, *Introduction to Superconductivity*, 2nd ed., (McGraw-Hill, New York, 1996)

[10] K. Moon, R. T. Scalettar, and G. T. Zimanyi, *Dynamical phases of driven vortex systems*, Phys. Rev. Lett. **77**, 2778 (1996)

[11] C. J. Olson, C. Reichhardt, and F. Nori, *Nonequilibrium Dynamic Phase Diagram for Vortex lattices*, Phys. Rev. Lett. **81**, 3757 (1998)

[12] L. Tisza, *Transport Phenomena in Heluim II*, Nature **141**, 913 (1938)

[13] L. Landau, *The Theory of Superfluidity of Helium II*, J. Phys. (USSR) **5**, 71, (1941)

[14] M. H. Anderson, J. R. Ensher, M. R. Matthews, C. E. Wieman, and E. A. Cornell, *Observation of Bose-Einstein Condensation in a Dilute Atomic Vapor*, Science **269**, 198 (1995)

[15] K. B. Davis, M. O. Mewes, M. R. Andrews, N. J. van Druten, D. S. Durfee, D. M. Kurn, and W. Ketterle, *Bose-Einstein Condensation in a Gas of Sodium Atoms*, Phys. Rev. Lett. **75**, 3969 (1995)

[16] C. C. Bradley, C. A. Sackett, and R. G. Hulet, *Bose-Einstein Condensation of Lithium: Observation of Limited Condensate Number*, Phys. Rev. Lett. **78**, 985 (1997)

[17] S. L. Cornish, N. R. Claussen, J. L. Roberts, E. A. Cornell, and C. E. Wieman, *Stable Rb-85 Bose-Einstein Condensates With Widely Tunable Interactions*, Phys. Rev. Lett. **85**, 1795 (2000)

[18] D. G. Fried, T. C. Killian, L. Willmann, D. Landhuis, S. C. Moss, D. Kleppner, and T. J. Greytak, *Bose-Einstein Condensation of Atomic Hydrogen*, Phys. Rev. Lett. **81**, 3811 (1998)

[19] A. Robert, O. Sirjean, A. Browaeys, J. Poupard, S. Nowak, D. Boiron, C. I. Westbrook, and A. Aspect, *A Bose-Einstein condensate of metastable atoms*, Science **292**, 461 (2001)

[20] F. P. Dos Santos, J. Leonard, J. M. Wang, C. J. Barrelet, F. Perales, E. Rasel, C. S. Unnikrishnan, M. Leduc, and C. Cohen-Tannoudji, *Bose-Einstein condensation of metastable helium*, Phys. Rev. Lett. **86**, 3459 (2001)

[21] C. S. Adams and E. Riis, *Laser Cooling and Trapping of Neutral Atoms*, Prog. Quantum Elect. **21**, 1 (1997)

[22] K. W. Madison, F. Chevy, W. Wohlleben, and J. Dalibard, *Vortex Formation in a Stirred Bose-Einstein Condensate*, Phys. Rev. Lett. **84**, 806 (2000)

[23] J. R. Abo-Shaeer, C. Raman, J. M. Vogels, and W. Ketterle, *Observation of Vortex Lattices in Bose-Einstein Condensates*, Science **292**, 476 (2001)

[24] C. Raman, M. Köhl, R. Onofrio, D. S. Durfee, C. E. Kuklewicz, Z. Hadzibabic, and W. Ketterle, *Evidence for a Critical Velocity in a Bose-Einstein Condensate*, Phys. Rev. Lett. **83**, 2502 (1999)

[25] B. Jackson, J. F. McCann, and C. S. Adams, *Dissipation and Vortex Creation in Bose-Einstein Condensed Gases*, Phys. Rev. A **61**, 051603 (R) (2000)

[26] A. G. Truscott, K. E. Strecker, W. I. McAlexander, G. B. Partridge, and R. G. Hulet, *Observation of Fermi Pressure in a Gas of Trapped Atoms*, Science **291** 2570 (2001)

[27] G. Bruun, Y. Castin, R. Dum, and K. Burnett, *BCS Theory for Trapped Ultracold Fermions* Eur. Phys. J. D **7**, 433 (1999)

[28] M. O. Mewes, M. R. Andrews, D. M. Kurn, D. S. Durfee, C. G. Townsend, and W. Ketterle, *Output Coupler for Bose-Einstein Condensed Atoms*, Phys. Rev. Lett. **78**, 582 (1997)

[29] E. W. Hagley, L. Deng, M. Kozuma, J. Wen, K. Helmerson, S. L. Rolston, and W. D. Phillips, *A Well-Collimated Quasi-Continuous Atom Laser*, Science **283** 1706 (1999)

[30] I. Bloch, T. W. Hänsch, and T. Esslinger, *Atom Laser With a CW Output Coupler*, Phys. Rev. Lett **82**, 3008 (1999)

[31] V. L. Ginzburg and L. P. Pitaevskii, *On the Theory of Superfluidity*, Sov. Phys. JETP **7**, 858 (1958); E. P. Gross, *Hydrodynamics of a Superfluid Condensate*, J. Math. Phys. **4**, 195 (1963)

[32] F. Dalfovo, S. Giorgini, L. P. Pitaevskii, and S. Stringari, *Theory of Trapped Bose-Condensed Gases*, Rev. Mod. Phys. **71**, 463 (1999)

[33] A. J. Leggett, *Bose-Einstein Condensation in the Alkali Gases: Some Fundamental Concepts* Rev. Mod. Phys. **73**, 307 (2001)

[34] M. Gajda and K. Rzazewski, *Fluctuations of Bose-Einstein Condensate*, Phys. Rev. Lett. **78**, 2686 (1997)

[35] R. K. Pathria *Statistical Mechanics*, Pergamom Press, Oxford (1972)

[36] J. L. Roberts, N. R. Claussen, S. L. Cornish, E. A. Donley, E. A. Cornell, and C. E. Wiemann, *Controlled Collapse of a Bose-Einstein Condensate*, Phys. Rev. Lett **86**, 4211 (2001)

[37] N. G. Berloff, *Nonlocal Nonlinear Schrödinger Equations as Models of Superfluidity*, J. Low Temp. Phys. **116**, 359 (1999)

[38] N. G. Berloff and P. H. Roberts, *Motions in a Bose Condensate: VI. Vortices in a Nonlocal Model*, J. Phys. A **32**, 5611 (1999)

[39] R. J. Marshall, G. H. C. New, K. Burnett, and S. Choi, *Exciting, Cooling, and Vortex Trapping in a Bose-Condensed Gas*, Phys. Rev. A **59**, 2085 (1999)

[40] M. J. Davis, S. A. Morgan, and K. Burnett, *Simulations of Bose fields at finite temperature*, cond-mat/0011431 (2000)

[41] J. Nagamatsu, N. Nakagawa, T. Muranaka, Y. Zenitani, and J. Akimitsu, *Superconductivity at 39 K in Magnesium Diboride*, Nature, **410**, 63 (2001)

[42] H. Vogel *Gerthsen Physik*, Springer-Verlag Berlin Heidelberg (1995)

[43] V. L. Ginzburg and L. D. Landau, *On the Theory of Superconductivity*, Zh. Eksperim. i. Teor. Fiz. (JETP) **20**, 1064 (1950)

[44] L. P. Gor'kov, Zh. Eksperim. i. Teor. Fiz. **36**, 1918 (1959); Soviet Phys.-JETP **9**, 1364 (1959)

[45] K. J. M. Moriarty, E. Myers, and C. Rebbi, *Dynamical Interactions of Cosmic Strings and Flux Vortices in Superconductors*, Phys. Lett. B **207**, 411 (1988)

[46] T. Tsuneto, *Superconductivity and Superfluidity*, (University Press, Cambridge, 1998)

[47] M. Tinkham, *Introduction to superconductivity*, 1st ed., McGraw-Hill, New York (1975)

[48] G. Bednorz and K. A. Müller, *Possible High T_c Superconductivity in the Ba-La-Cu-O System*, Z. Phys. **B64**, 189 (1986)

[49] M. Machida and H. Kaburaki, *Structure of Flux Lines in Three-Dimensional Layered Type-II Superconductors: Numerical Experiments*, Phys. Rev. Lett. **74**, 1434 (1995); *Direct Numerical Experiment on Two-Dimensional Pinning Dynamics of a Three-Dimensional Vortex Line in Layered Superconductors*, Phys. Rev. Lett. **75**, 3178 (1995)

[50] D. S. Fisher, M. P. A. Fisher, and D. A. Huse, *Thermal fluctuations, quenched disorder, phase transitions, and transport in type-II superconductors* Phys. Rev. B **43**, 130 (1991)

[51] R. Kato, Y. Enomoto, and S. Maekawa, *Effects of the surface boundary on the magnetization process in type-II superconductors*, Phys. Rev. B **47**, 8016 (1993)

[52] N. B. Kopnin, B. I. Ivlev, and Lalatsky, *The Flux-Flow Hall Effect in Type II Superconductors, An Explanation of the Sign Reversal*, J. Low Temp. Phys. **90**, 1 (1993)

[53] A. T. Dorsey, *Vortex Motion and the Hall-Effect in Type-II Superconductors - A Time-Dependent Ginzburg-Landau Theory Approach*, Phys. Rev. B **46**, 8376 (1992)

[54] L. D. Landau and E. M. Lifshitz, *Fluids Mechanics*, 2nd Ed., (Butterworth-Heinemann, Oxford 1987)

[55] E. Madelung, *Quantentheorie in hydrodynamischer Form*, Zeit. f. Phys. **40**, 322 (1926)

[56] P. Nozières and D. Pines, *Theory of Quantum Liquids Vol II*, (Addison-Wesley, Redwood City, 1990)

[57] B. M. Caradoc-Davies, R. J. Ballagh, and K. Burnett, *Coherent Dynamics of Vortex Formation in Trapped Bose-Einstein Condensates*, Phys. Rev. Lett. **83**, 895 (1999)

[58] G. W. Rayfield and F. Reif, *Quantized Vortex Rings in Superfluid Helium*, Phys. Rev. **136**, 1194 (1964)

[59] Y. Kagan, A. E. Muryshev, and G. V. Shlyapnikov, *Collapse and Bose-Einstein Condensation in a Trapped Bose Gas with Negative Scattering Length*, Phys. Rev. Lett. **81**, 933 (1998)

[60] F. Dalfovo and S. Stringari *Bosons in Anisotropic Traps: Ground State and Vortices*, Phys. Rev. A **53** 2477 (1996)

[61] I. Aranson, and V. Steinberg, *Stability of Multicharged Vortices in a Model of Superflow*, Phys. Rev. B **53**, 75 (1996)

[62] P. H. Roberts and J. Grant, *Motion in a Bose Condensate I. The structure of the large circular vortex*, J. Phys. A **4**, 55 (1971)

[63] C. A. Jones and P. H. Roberts, *Motions in a Bose Condensate: IV. Axisymmetric Solitary Waves*, J. Phys. A **15**, 2599 (1982)

[64] V. Hakim, *Nonlinear Schrödinger Flow Past an Obstacle in One Dimension*, Phys. Rev. E, **55**, 2835 (1997)

[65] J. A. Freire, D. P. Arovas, and H. Levine, *Quantum Nucleation of Phase Slips in a 1D Model of a Superfluid*, Phys. Rev. Lett., **79**, 5054 (1997)

[66] C. Huepe and M.-É. Brachet, *Vortical Nucleation Solutions in a Model of Superflow*, C. R. Acad. Sci. Paris, Série 2 b, **325**, 195 (1997)

[67] K. W. Schwarz, *Effect of Surface-Roughness on the Critical Velocities of Superfluid He-4*, Phys. Rev. Lett., **69**, 3342 (1992)

[68] B. Jackson, J. F. McCann, and C. S. Adams, *Vortex Formation in Dilute Inhomogeneous Bose-Einstein Condensates*, Phys. Rev. Lett. **80**, 3903 (1998)

[69] D. C. Samuels and R. J. Donnelly, *Motion of Charged Vortex Rings in Helium II*, Phys. Rev. Lett. **67**, 2505 (1991)

[70] G. W. Rayfield, *Evidence for a Peeling Model of Vortex Ring Formation by Ions in Liquid Helium*, Phys. Rev. Lett. **19**, 1371 (1967)

[71] P. C. Hendry, N. S. Lawson, P. V. E. McClintock, and C. D. H. Williams, *Macroscopic Quantum Tunnelling of Vortices in He-II*, Phys. Rev. Lett. **60**, 604 (1988)

[72] D. S. Hall, M. R. Matthews, J. R. Ensher, C. E. Wieman, and E. A. Cornell, *Dynamics of Component Separation in a Binary Mixture of Bose-Einstein Condensates*, Phys. Rev. Lett. **81**, 1539 (1998)

[73] B. Jackson, J. F. McCann, and C. S. Adams, *Vortex Rings and Mutual Drag in Trapped Bose-Einstein Condensates* Phys. Rev. A **60**, 4882 (1999)

[74] T. Frisch, Y. Pomeau, and S. Rica, *Transition to Dissipation in a Model of Superflow*, Phys. Rev. Lett. **69**, 1644 (1992)

[75] C. Josserand and Y. Pomeau, *Generation of Vortices in a Model of Superfluid He-4 by the Kadomtsev-Petviashvili Instability*, Europhys. Lett. **30**, 43 (1995)

[76] M. Leadbeater, T. Winiecki, D. C. Samuels, C. F. Barenghi, and C. S. Adams, *Sound Emission Due to Superfluid Vortex Reconnections*, Phys. Rev. Lett. **86**, 1410 (2001)

[77] R. Onofrio, C. Raman, J. M. Vogels, J. R. Abo-Shaeer, A. P. Chikkatur, and W. Ketterle, *Observation of Superfluid Flow in a Bose-Einstein Condensed Gas*, Phys. Rev. Lett **85**, 2228 (2000)

[78] C. Nore, C. Huepe, and M. E. Brachet, *Subcritical Dissipation in Three-Dimensional Superflows*, Phys. Rev. Lett **84**, 2191 (2000)

[79] P. O. Fedichev and G. V. Shlyapnikov, *Critical Velocity in Cylindrical Bose-Einstein Condensates*, Phys. Rev. A **63**, 045601 (2001)

[80] G. B. Hess, *Angular Momentum of Superfluid Helium in a Rotating Cylinder*, Phys. Rev. **161**, 189 (1967)

[81] E. J. Yarmchuk and M. J. V. Gordon, *Observation of Stationary Vortex Arrays in Rotating Superfluid Helium*, Phys. Rev. Lett. **43**, 214 (1979)

[82] D. A. Butts and D. S. Rokhsar, *Predicted Signatures of Rotating Bose-Einstein Condensates*, Nature **397**, 327 (1999)

[83] D. L. Feder, C. W. Clark, and B. I. Schneider *Nucleation of vortex arrays in rotating anisotropic Bose-Einstein condensates* Phys Rev A **6001**: 1601 (2000)

[84] Y. N. Ovchinnikov and I. M. Sigal, *Long-time behaviour of Ginzburg-Landau vortices*, Nonlinearity **11**, 1295 (1998)

[85] L. F. Chibotaru, A. Ceulemans, V. Bruyndoncx, and V. V. Moshchalkov, *Vortex Entry and Nucleation of Antivortices in a Mesoscopic Superconducting Triangle*, Phys. Rev. Lett. **86**, 1323 (2001)

[86] L. P. Gor'kov and N. B. Kopnin, *Vortex motion and resistivity of type-II superconductors in a magnetic field* Usp. Fiz. Nauk **116**, 413 (1975); Sov. Phys.-Usp. **18**, 496 (1976)

[87] R. D. Parks, *Superconductivity*, Vol. 1 and 2, (Marcel Dekker, Inc., New York, 1969)

[88] P. G. deGennes, *Superconductivity of Metals and Alloys*, W. A. Benjamin, New York (1966), p. 227; reprinted by Addison-Wesley (1989)

[89] A. A. Abrikosov, *On the Magnetic Properties of Superconductors of the Second Group*, Zh. Eksperim. i. Teor. Fiz. **32**, 1442 (1957); Sov. Phys. JETP **5**,1174 (1957)

[90] A. K. Geim, I. V. Grigorieva, S. V. Dubonos, J. G. S. Lok, J. C. Maan, A. E. Filippov, and F. M. Peeters, *Phase Transitions in Individual Sub-Micrometre Superconductors*, Nature **390**, 259 (1997)

[91] P. Singha Deo, V. A. Schweigert, and F. M. Peeters, *Magnetization of Mesoscopic Superconducting Disks*, Phys. Rev. Lett. **79**, 4653 (1997)

[92] V. A. Schweigert, F. M. Peeters, and P. Singha Deo *Vortex Phase Diagram for Mesoscopic Superconducting Disks*, Phys. Rev. Lett. **81**, 2783 (1998)

[93] P. Singha Deo, V. A. Schweigert, and F. M. Peeters, *Hysteresis in mesoscopic superconducting disks: The Bean-Liningston barrier*, Phys. Rev. B **59**, 6039 (1999)

[94] C. P. Bean and J. D. Livingston, *Surface Barrier in Type-II Superconductors*, Phys. Rev. Lett. **12**, 14 (1964)

[95] D. Saint-James and P. G. de Gennes, *Onset of Superconductivity in Decreasing Fields*, Phys. Lett. **7**, 306 (1963)

[96] Y. B. Kim, C. F. Hempstead, and A. R. Strnad, *Flux-Flow Resistance in Type-II Superconductors*, Phys. Rev. **139**, A 1163 (1965)

[97] G. W. Crabtree, D. O. Gunter, H. G. Kaper, A. E. Koshelev, G. K. Leaf, and V. M. Vinokur *Numerical simulations of driven vortex systems*, Phys. Rev. B **61**, 1446 (2000)

[98] C. Reichhardt, C. J. Olson, N. Gronbech-Jensen, and F. Nori, *Moving Wigner Glasses and Smectics: Dynamics of Disordered Wigner Crystals* Phys. Rev. Lett. **86**, 4354 (2001)

[99] M. Machida and H. Kaburaki, *Direct simulation of the time-dependent Ginzburg-Landau equation for type-II superconducting thin films: Dynamics and V-I characteristics*, Phys. Rev. Lett. **71**, 3206 (1993)

[100] M. Machida and H. Kaburaki, *Numerical simulation of flux-pinning dynamics for a defect in a type-II superconductor* Phys. Rev. B **50**, 1286 (1994)

[101] G. Stejic, L. D. Cooley, R. Joynt, D. C. Larbalestier, and S. Takacs, *Numerical Calculation of Flux Pinning by α-Ti Precipitates in Nb-Ti*, Supercond. Sci. Technol. **5**, S176 (1992)

[102] E. V. Thuneberg, J. Kurkijarvi, and D. Rainer, *Pinning of a Vortex Line to a Small Defect in Superconductors*, Phys. Rev. Lett. **48**, 1853 (1982)

[103] G. Blatter, M. V. Feigelman, V. B. Geshkenbein, A. I. Larkin, and V. M. Vinokur, *Vortices in Superconductors*, Rev. Mod. Phys. **66**, 1125 (1994)

[104] N. Savvides, A. Katsaros, and S. X. Dou, *Critical current density and flux pinning in silver/superconductor composites and tapes*, Physica C **179**, 361 (1991)

[105] V. V. Moshchalkov, M. Baert, V. V. Metlushko, E. Rosseel, M. J. Van Bael, K. Temst, and Y. Bruynseraede, *Pinning by an Antidot Lattice: The Problem of the Optimum Antidot Size*, Phys. Rev. B **57**, 3615 (1998)

[106] M. J. Van Bael, L. Van Look, M. Lange, K. Temst, G. Güntherodt, V. V. Moshchalkov, and Y. Bruynseraede, *Vortex Confinement by Regular Pinning Arrays*, Physica C **341**, 965 (2000)

[107] D. J. Morgan and J. B. Ketterson, *Fluxon Pinning by Artificial Magnetic Arrays*, J. Low Temp. Phys. **122**, 37 (2001)

[108] W. H. Press, S. A. Teukolsky, W. T. Vetterling and B. P. Flannary, *Numerical recipes in Fortran : The Art of Scientific Computing*, 2nd Ed. CUP, Cambridge, 1992.

[109] W. F. Ames *Numerical Methods for Partial Differential Equations*, (Academic Press, Inc. San Diego, 1992)

[110] T. R. Taha and M. J. Ablowitz, *Analytical and Numerical Aspects of Certain Nonlinear Evolution Equations. II. Numerical, Nonlinear Schrödinger Equation*, J. Comp. Phys. **55**, 203 (1984)

[111] W. D. Gropp, H. G. Kaper, G. K. Leaf, D. M. Levine, M. Palumbo, and V. M. Vinokur, *Numerical simulation of vortex dynamics in type-II superconductors*, J. Comput. Phys. **123**, 254 (1996)

[112] H. Frahm, S. Ulah, and A. T. Dorsey, *Flux dynamics and the growth of the superconducting phase*, Phys. Rev. Lett. **66**, 3067 (1991)

[113] R. Kato, Y. Enomoto, and S. Maekawa, *Computer simulations of dynamics of flux lines in type-II superconductors*, Phys. Rev. B **44**, 6916 (1991)

[114] E. Coskun and M. K. Kwong, *Simulating vortex motion in superconducting films with the time-dependent Ginzburg-Landau equations*, Nonlinearity **10**, 579 (1997)

[115] J. F. Blackburn, A. Campbell, and E. K. H. Salje, *The force-free case in three-dimensional superconductors: a computational study*, Philos. Mag. B **80**, 1455 (2000)

[116] Q. Du, *Finite element method for the time dependent GL model of superconductivity*, Comp. Math. Appl. **27**, 119 (1994)

[117] Q. Du, M. D. Gunzburger, and J. S. Peterson, *Solving the Ginzburg-Landau equations by finite-element methods*, Phys. Rev. B **46**, 9027 (1992)

[118] L. Q. Chen and J. Shen, *Applications of semi-implicit Fourier-spectral method to phase field equations*, Comp. Phys. Commun. **108**, 147 (1998)

[119] A. V. Samokhvalov, *Expanding Vortex Rings in a Current-Carrying Superconducting Cylinder*, Physica C **308**, 74 (1998)

[120] Y. A. Genenko, *Magnetic self-field entry into a current-carrying type-II superconductor*, Phys. Rev. B **49**, 6950; *Magnetic self-field entry into a current-carrying type-II superconductor. II. Helical vortices in a longitudinal magnetic field*, Phys. Rev. B **51**, 3686 (1995)

[121] B. C. Belanger and M. A. R. LeBlanc, *Interaction of Conduction and Induced Currents in Nb_3Zr Wires Subjected to Axial Fields*, Appl. Phys. Lett. **10**, 298 (1967)